VNIVERSITAT DE VALÈNCIA

Departamento de Física Atómica, Molecular y Nuclear

SiPM based tracking for detector calibration in NEXT

DOCTORADO EN FÍSICA

David Lorca Galindo

Dirigida por Dr. Juan José Gómez Cadenas

SiPM based tracking for detector calibration in NEXT

Author: David Lorca Galindo

Advisor: Dr. Juan José Gómez Cadenas

The following web-page address contains up to date information about this dissertation and related topics:
`http://next.ific.uv.es/next/index.php`

Text printed in Valencia
First edition, March 2015

Agradecimientos

Este trabajo pone fin a un periodo tanto académico como personal, en el cual he tenido oportunidad de aprender en ambos aspectos de mi vida. En primer lugar me gustaría agradecer a Manuela por su paciencia y apoyo durante todos los momentos difíciles que han acaecido durante este tiempo; esta tesis es en gran medida obra suya. También a mis padres, quienes me han ayudado desde el principio de mi carrera haciéndome ver que nada era imposible, y a mis hermanos, quienes siempre han sido un ejemplo a seguir en mi vida y me han ayudado a despejar la mente cuando fue necesario.

Por otro lado, quiero agradecer a J.J. Gómez Cadenas por darme la oportunidad de realizar mis estudios de doctorado en el experimento NEXT, y sobre todo de poder hacerlo en la espina dorsal del experimento como es el grupo de Valencia. Sin el conocimiento, experiencia y liderazgo de J.J., este grupo no habría llegado tan lejos. Gracias a Justo por todo su tiempo durante las eternas discusiones sobre el análisis y por sus indicaciones hacia donde y como proceder; sus palabras, aunque él nunca lo creería, siempre fueron bien recibidas. Gracias también a Andrew por sus continuas iteraciones durante la escritura de este trabajo, y por estar siempre disponible para una cerveza; ambas cualidades me han ayudado por igual. Me gustaría agradecer especialmente a Luis, Miquel y Toni por sumarse siempre a estas cervezas, por su empatía

y por compartir tantos y tantos momentos, discusiones y risas en ese despacho, en el cual siempre habrá que cerrar la puerta.

También quiero dar las gracias a todas las personas con las que he compartido estos años y que de una manera u otra han colaborado en la finalización de este trabajo. A Nadia Yahlali y Markus Ball por guiarme en los inicios de esta carrera, a Curro y Raúl por proporcionarnos la maquina de hacer tesis, a Alex Gil, Javi R. y Vicente por su constante ayuda y por el trabajo compartido. A los nexters Michel, Paola, Miguel G.V., Igor, Francesc, Manolo, Javi P., Ander, Marc, Javi M., Sara, Alberto, Josh, Neus y Pau por su aportación a hacer que funcione.

A todos vosotros ...

Infinitas gracias,
David Lorca Galindo
Marzo 2015

Resumen

Desde que el neutrino fue propuesto en 1930 por el físico austríaco Wolfgang Pauli, y posteriormente detectado experimentalmente en 1957 por los físicos Clyde L. Cowan and Frederick Reines, muchas propiedades de esta singular partícula han sido reveladas, como su spin, su carga eléctrica y su tipo de interacción con el resto de partículas del Modelo Standard. Sin embargo, una de las más importantes propiedades que todavía no ha sido revelada es la propia naturaleza del neutrino, y como esta influenció en la evolución de nuestro Universo.

Inicialmente, el neutrino fue introducido en el Modelo Standard de Física de Partículas como una partícula no masiva. Sin embargo, los experimentos desarrollados durante las ultimas décadas basados en la oscilación de neutrinos, han demostrado que estos deben tener masa, y por tanto, al igual que para el resto de leptones cargados, un termino de masa asociado a los neutrinos debe ser incluido en el Modelo Standard. Una de las maneras en las que este termino de masa puede ser incluido sugiere que los neutrinos podrían ser partículas de Majorana, es decir, idénticas a sus antipartículas, al contrario que el resto de fermiones del Modelo Standard.

Actualmente, el único procedimiento experimental que puede confirmar la naturaleza Majorana del neutrino es la observación de la desintegración doble beta sin neutrinos ($\beta\beta0\nu$), en donde un núcleo con

número atómico Z y número másico A decae en su isóbaro de número atómico Z+2 emitiendo únicamente dos electrones:

$$ {}^{A}_{Z}X \rightarrow {}^{A}_{Z+2}\,Y + e_1^- + e_2^- $$

El descubrimiento de este hipotético proceso establecería, sin lugar a dudas, la naturaleza Majorana del neutrino al mismo tiempo que proporcionaría información directa sobre la masa del neutrino, y por que esta debe ser tan pequeña comparada con el resto de fermiones de la misma generación. Además, la observación de $\beta\beta0\nu$ demostraría que la conservación del número leptónico es violada en este proceso físico, resultado que puede ser asociado con la asimetría entre materia y antimateria de nuestro Universo mediante el proceso llamado leptogénesis.

El objetivo de todos los experimentos diseñados para observar la desintegración doble beta sin neutrinos es medir la semivida de este proceso. Sin embargo, esta medida está limitada por la sensibilidad experimental del detector empleado, que puede ser descrita como

$$ T_{1/2} \propto a \cdot \epsilon \cdot \sqrt{\frac{M \cdot t}{\Delta E \cdot B}} $$

donde M es la masa del isótopo empleado, t es el tiempo activo de toma de datos del detector, ΔE es su resolución en energía en la región de interés, ϵ es su eficiencia de detección y a es un término que incluye los elementos de matriz nuclear.

En este momento, los experimentos EXO-200 y KamLAND-Zen ya se encuentran buscando la desintegración $\beta\beta0\nu$ del isótopo ^{136}Xe. Sin embargo, ambos experimentos han obtenido resultados negativos, estableciendo un límite combinado a la semivida de la desintegración de $T^{0\nu}_{1/2}(^{136}Xe) > 3.4 \times 10^{25}$ años (90% CL). En paralelo, el experimento GERDA, que busca la desintegración $\beta\beta0\nu$ del isótopo ^{76}Ge, tampoco ha encontrado evidencias de este proceso, estableciendo un límite de $T^{0\nu}_{1/2}(^{76}\mathrm{Ge}) > 2.1 \cdot 10^{25}$ años (90% CL).

El Experimento NEXT (Neutrino Experiment with a Xenon TPC), que será instalado en el Laboratorio Subterráneo de Canfranc, buscará la desintegración $\beta\beta0\nu$ del isótopo ^{136}Xe utilizando una cámara de proyección temporal (TPC, por sus siglas en inglés), llena con 100 kg de xenón gaseoso enriquecido al 91% en su isótopo ^{136}Xe, a una presión de 15 bares y con amplificación por Electroluminescencia (EL). Con esta tecnología, una resolución en energía mejor que el 1% en $Q_{\beta\beta}$ del ^{136}Xe puede ser alcanzada gracias al pequeño factor de Fano del xenón gaseoso ($F_{GXe} = 0.15 \pm 0.02$) en comparación con otros medios de detección como el xenón líquido ($F_{LXe} \sim 20$), y a las pequeñas fluctuaciones introducidas por un sistema de amplificación basado en Electroluminescencia. Además, el xenón gaseoso como medio de detección proporciona información topológica de los eventos, permitiendo discriminar entre eventos $\beta\beta$, caracterizados por una traza retorcida de unos 10 cm de longitud y con dos deposiciones de energía en ambos extremos, de eventos de ruido producidos por interacciones de gammas de alta energía con el xenón.

El proceso de detección en NEXT presenta sistemas independientes para la medida de la energía y la información topológica. Las partículas que interaccionan con el xenón gaseoso ionizan y excitan sus átomos. La energía transferida mediante excitación es liberada en forma de luz de centelleo en la región ultravioleta ($\sim$ 172 nm), y recogida por un plano de PMTs, el plano de energía, posicionado detrás del cátodo transparente de la TPC, dando lugar al inicio del evento. Los electrones de ionización producidos derivan hacia el ánodo de la TPC debido al campo eléctrico existente. Una vez allí, entran en una región con un campo eléctrico aún más intenso, donde son acelerados produciendo luz de Electroluminescencia. Esta luz es emitida isotrópicamente, por lo que parte es detectada por el plano de energía mencionado anteriormente, proporcionando una medida precisa de la energía. Por otro lado, el resto de luz EL es detectada por un plano de SiPMs, el plano de

tracking, posicionado a tan solo unos milímetros de donde esta luz es generada, aportando la información topológica del evento.

Para demostrar que el concepto de detección propuesto por NEXT es factible, el prototipo NEXT-DEMO fue construido y operado en el Instituto de Física Corpuscular de Valencia. Dicho prototipo consiste en una vasija de alta presión hecha de acero inoxidable y capaz de aguantar 20 bares de presión interna. Sus 60 cm de largo y 30 cm de diámetro contienen aproximadamente 1.5 kg de xenón a 10 bares de presión. Tres rejillas metálicas (cátodo, gate y ánodo), definen las dos regiones activas de la TPC. Por un lado, 30 cm de región de deriva entre el cátodo y el gate, y por otro 0.5 cm de región de electroluminescencia entre el gate y el ánodo. El cátodo es operado típicamente a -25 kV, mientras que gate y ánodo a -10 kV y 0 V respectivamente. Con estos valores, un campo eléctrico de unos 500 V/cm es creado en la región de deriva, y un $\bar{E}/p$ de unos 2.0 kV bar^{-1} cm^{-1} en la región EL. Un juego de seis paneles de PTFE (Teflón) están presentes dentro formando un tubo de luz hexagonal. Este tubo de luz está recubierto además con un cambiador de longitud de onda (TPB), que aumenta la eficiencia de recolección de la luz de centelleo del xenón.

En el detector NEXT-DEMO, el plano de energía está formado por 19 PMTs de Hamamatsu modelo R7378A, mientras que el plano de tracking está formado por 256 SiPMs, también de Hamamatsu, modelo S10362-11-050P. Debido al gran numero de SiPMs utilizados, es imposible suministrar lineas de alimentación y lectura individuales a cada sensor, por ello, los SiPMs son montados en grupos de 64 elementos en tarjetas electrónicas, llamadas Dice Boards, y recubiertos con el mismo cambiador de onda mencionado anteriormente para adaptar la luz de centelleo del xenón a la región óptica donde estos sensores tienen su máxima sensibilidad.

Un estricto protocolo de deposición de la molécula TPB sobre los SiPMs ha sido desarrollado y diferentes caracterizaciones realizadas para asegurar la calidad de este procedimiento. Los resultados

muestran que este método asegura deposiciones uniformes, reproducibles y capaces de ser almacenadas a largo término. Al mismo tiempo, la aplicación directa de TPB sobre la superficie de los SiPMs, parece incrementar la sensibilidad de estos sensores a la luz de centelleo del xenón en casi un orden de magnitud.

Por otro lado, la descripción del proceso de funcionamiento y de las propiedades dinámicas de los SiPMs ponen de manifiesto la necesidad de corregir los parámetros de operación de estos sensores debido a los efectos introducidos por cambios en las condiciones durante la toma de datos. Para ello, una fuente de alimentación autocorregible ha sido diseñada y construida para asegurar la respuesta uniforme de los SiPMs con el tiempo.

Durante la operación del prototipo NEXT-DEMO, la abundancia de emisiones de rayos X por los átomos de xenón gracias a la interacción con gammas provenientes de diferentes fuentes radioactivas, ha sido identificada como una herramienta útil a la hora de caracterizar parámetros fundamentales del detector al mismo tiempo que proporcionan su ecualización en respuesta. La ventaja de utilizar estos eventos proviene de que están distribuidos por todo el volumen del detector y que su rango de alcance es pequeño, menor que un milímetro, por lo que producen deposiciones que pueden ser consideradas puntuales. Estas deposiciones han sido empleadas para describir la geometría del detector así como la pérdida de carga por la presencia de impurezas en el gas, proporcionando los factores de corrección necesarios para la correcta medida de la energía depositada.

Estas correcciones han sido aplicadas utilizando un método basado en la suma pesada de los PMTs para reconstruir la energía depositada por gammas provenientes de fuentes de ^{22}Na y ^{137}Cs, obteniendo una resolución en energía de (5.691 ± 0.003)% FWHM a 29.7 keV y (1.62 ± 0.01)% FWHM para 511 keV. La extrapolación de estos resultados al $Q_{\beta\beta}$ del ^{136}Xe predice una resolución en energía de 0.6256% FWHM y 0.7353% FWHM respectivamente.

Contents

1 Introduction **1**

2 The Nature of Neutrinos **5**
2.1 Neutrino Masses and Mixing 8
2.2 Experimental Neutrino Mass Measurement 12
2.3 Dirac or Majorana Neutrinos 14
2.4 The *see-saw* Mechanism 17
2.5 Double Beta Decay 18
2.5.1 $\beta\beta0\nu$ Rate 21
2.5.2 Double Beta Decay Experiments 22

3 The NEXT Experiment **27**
3.1 Xenon Gas as Detection Medium 28
3.2 Intrinsic Energy Resolution in Xenon Gas Detectors . . 34
3.3 Tracking for Background Rejection 37
3.4 The SOFT Concept 39
3.5 The NEXT-100 detector 42
3.5.1 Pressure Vessel 42
3.5.2 Field Cage 45
3.5.3 Gas System 45
3.5.4 Energy Plane 47

3.5.5 Tracking Plane 49
3.5.6 Data Acquisition 50
3.5.7 Shielding 50
3.6 Projected Sensitivity 52
3.7 The NEXT-DEMO prototype 55

4 The NEXT-DEMO Tracking Plane 59
4.1 Introduction to Semiconductor Detectors 60
4.2 Silicon PhotoMultipliers 65
4.2.1 Electrical Model 67
4.2.2 Gain and Breakdown Voltage 67
4.2.3 Recovery Time 74
4.2.4 Afterpulsing 76
4.2.5 Dark Count Rate 76
4.2.6 Optical Crosstalk 78
4.2.7 Photon Detection Efficiency 80
4.2.8 Dynamic Range 83
4.2.9 Suitability for NEXT 85
4.3 SiPM Coating with a WLS 87
4.3.1 Coating Protocol 87
4.3.2 Characterization of Coatings 90
4.3.3 Response of Coated SiPMs 93
4.4 Dice Boards 95
4.5 Tracking Plane Electronics 98
4.6 Active Control of the Gain 101
4.7 Installation of the Tracking Plane 109

5 Commissioning and Results 113
5.1 Internal Calibration 114
5.1.1 X-ray Calibration 116
5.1.2 Photon Transfer Curve 117
5.1.3 Common Noise Filtering 119

5.2 X-rays Production in Xenon 124
5.3 Data Sets, Preprocessing and Selection 124
5.4 Monte Carlo Data Generation 126
5.5 Position Reconstruction 128
5.6 Properties of Xenon EL-based TPC 130
5.6.1 Drift Velocity 131
5.6.2 Longitudinal Spread 132
5.6.2.1 EL Gap Induced Longitudinal Spread . 132
5.6.2.2 Longitudinal Diffusion 134
5.6.3 Transverse Spread 136
5.7 Energy Resolution 139
5.7.1 Electron Attachment 139
5.7.2 Time-related Fluctuations 140
5.7.3 XY Response 141
5.7.4 Calculation of Energy Weighted Sum 142
5.7.5 Extrapolation to Higher Energies 148

6 Summary and Conclusions **151**

List of Figures **155**

List of Tables **165**

Bibliography **167**

Dear Radioactive Ladies and Gentlemen ...

Wolfgang Pauli

CHAPTER

1

Introduction

The neutrino was first proposed in 1930 by the Austrian physicist Wolfgang Pauli, one of the fathers of quantum mechanics, as an explanation for the apparent loss of energy and momentum in the beta decay of neutrons ($n \rightarrow p + e^- + \bar{\nu}_e$). Pauli assumed the existence of a hypothetical particle which would also be produced in the decay accounting for the apparently lost energy and momentum. This particle would have no mass, no charge, and no strong interaction, being, therefore, very difficult to detect with the technology of the time.

Only a quarter of century later its existence could be proven. In 1956, the physicists Clyde L. Cowan and Frederick Reines used the nuclear reactor located at Savannah River, in South Carolina, as a neutrino source. The goal of the so-called Cowan-Reines neutrino experiment was the observation of the interaction between neutrinos and protons in a water tank [1]. The discovery was awarded the Nobel Prize in 1995.

Since then, many properties of neutrinos have been determined, such as their spin, electric charge or type of interaction. Nevertheless, the fundamental nature of the neutrino remains unclear: its mass, its relation to the other fundamental particles and its roll in the evolution of the Universe are still under debate.

Initially, neutrinos were introduced in the Standard Model (SM) of Particle Physics as massless particles. However, recent experiments on neutrino oscillations have demonstrated that they must have a mass (see § 2.1) and, therefore, a neutrino mass term must be introduced into the Standard Model. One way in which this mass term can be introduced into the SM suggests that neutrinos could be Majorana particles (see § 2.3), that is, identical to their antiparticles, instead of Dirac particles, as the other SM fermions.

Currently, the only experimental method that can directly confirm the Majorana nature of neutrinos is the observation of neutrinoless double beta decay ($\beta\beta0\nu$). The discovery of this hypothetical process would unambiguously establish a Majorana nature for the neutrino and would provide direct information on neutrino masses. Moreover, it would demonstrate that total lepton number is violated, a result that can be linked to the cosmic asymmetry between matter and antimatter through the process known as leptogenesis [2, 3].

The Neutrino Experiment with a Xenon TPC (NEXT) is one of the experiments designed to prove the existence of $\beta\beta0\nu$. The *NEXT Collaboration*, which is formed by around 70 members at 14 international institutions, has designed and built different prototypes which indicate that the chosen technology, an asymmetric Time Projection Chamber (TPC) with Electroluminescence amplification, satisfies the requirements for a $\beta\beta0\nu$ experiment (see § 2.5.2): excellent energy resolution, topological information for the identification of signal and background [4, 5] and scalability to future 1-ton detectors.

In NEXT, the inclusion of a tracking plane for reconstructing the electron tracks inside the TPC allows to discriminate real $\beta\beta0\nu$ events

from others events coming from natural radioactivity (see § 3.3). Nevertheless, due to the diameter of the NEXT detector, a large number of small photosensors are required to fully cover the EL producing region with sufficient granularity (see § 3.5.5).

This thesis attempts to answer many of the questions that have arisen during the design and construction of the detector's prototype and the different techniques used for characterization and calibration of its tracking plane. These results are applied to correct the fluctuations in sensor's response due to the operative conditions. At the same time, the tracking plane is used to describe the geometric effects involved in the measurement of the charge released by electrons in xenon, in order to reach an energy resolution close to the intrinsic in gaseous xenon.

In Chapter 2, the current knowledge about neutrinos is described. It explains how massive neutrinos can be introduced in the Standard Model of Particle Physics, and how neutrinoless double beta decay can contribute with direct information about neutrino masses. It also lists the current generation of $\beta\beta0\nu$ experiments, including their current status.

Chapter 3 introduces the experimental concept of NEXT and the principal detector NEXT-100, which will search for the neutrinoless double beta decay of ^{136}Xe at the *Laboratorio Subterráneo de Canfranc*. In addition, the scaled-down prototype NEXT-DEMO, designed to demonstrate that the detector concept is reliable and feasible is also presented.

In Chapter 4, a detailed description of the NEXT-DEMO tracking plane is given, justifying the choice of settings and describing the characterization of the sensors of which it is formed. These studies led to the publication of the paper *"Design and characterization of the SiPM tracking system of NEXT-DEMO, a demonstrator prototype of the NEXT-100 experiment"* [6], JINST 8 (2013) T05002, [arXiv:1206.6199], of which I was a main author. This chapter also includes the description of the wavelength shifter used to adapt the response of the sensors to

the scintillation light of xenon, which led to the publication of the paper *"SiPMs coated with TPB: coating protocol and characterization for NEXT"* [7], JINST 7 (2012) P02010, [arXiv:1201.2018], of which I also was a main author.

Chapter 5 presents the utilization of X-ray depositions as multi-tool for description of the NEXT-DEMO TPC. The X-ray emission of the xenon atoms enables the realization of several studies of xenon gas properties, like electron diffusion, drift velocities, etc, while at the same time, produces the point-like energy depositions required to calibrate the spatial variation in the response of the detector. These studies have been applied to reconstruct the energy released by gamma particles coming from external sources, achieving an excellent energy resolution in the NEXT-DEMO prototype. The results were published in the paper *"Characterisation of NEXT-DEMO using xenon K_α X-rays"* [4], JINST 9 (2014) P10007, [arXiv:1407.3966], of which I was also a main author.

Finally, Chapter 6 concludes.

Personally, I think it does help, that it makes a beneficial difference, but the scientific literature on the subject is very messy.

Jeanne Petrek

CHAPTER

2

The Nature of Neutrinos

The Standard Model (SM) of Particle Physics (Figure 2.1) is a theory concerning the electromagnetic, weak, and strong nuclear interactions, which describes fundamental properties of subatomic particles. This model works well in general, but there are still some missing pieces, many of them related to neutrinos. These particles are unique in many ways; in particular, their lack of color or electromagnetic charge means that, of the three fundamental forces described by the SM, they only feel the weak force. The Standard Model requires massless neutrinos in its basic formulation, but recent experiments on neutrino oscillations have demonstrated that they are massive particles, opening a new field of physics beyond the Standard Model.

Neutrinos might be the only particles having a Majorana mass term, forbidden to the other fermions, explaining the different mass scale of

neutrinos compared with other fundamental particles (Figure 2.1) [8]. Experimental evidence of this phenomenon would have deep implications in physics and cosmology, since Majorana particles would be their own antiparticles as described by Majorana [9]. In addition, Majorana particles are a basic ingredient for the *see-saw mechanism*, needed to describe the lightness of neutrino mass relative to other fermions of the same generation without fine-tuning, and would provide a possible mechanism for leptogenesis.

If neutrinos are Majorana particles, neutrinoless double beta decay ($\beta\beta0\nu$) could be observable and a mean to prove this hypothesis. The simple existence of $\beta\beta0\nu$ decay would prove that neutrinos are Majorana particles and that lepton number is not always conserved, while the decay rate would measure the neutrino mass.

This chapter describes different neutrino characteristics and presents the techniques used to study them. Neutrino oscillations and how it solved fundamental problems of particle physics and astrophysics is explained in § 2.1, while in § 2.2, the different ways scientists are trying to measure the neutrino mass are described. In § 2.3, the basic formulation necessary to introduce a neutrino mass term into the Standard Model is presented and, assuming a Majorana nature for neutrinos, the most natural explanation of the smallness of neutrino masses is given in § 2.4. In § 2.5 the measurement of the $\beta\beta0\nu$ decay rate and its implications for the Standard Model is presented.

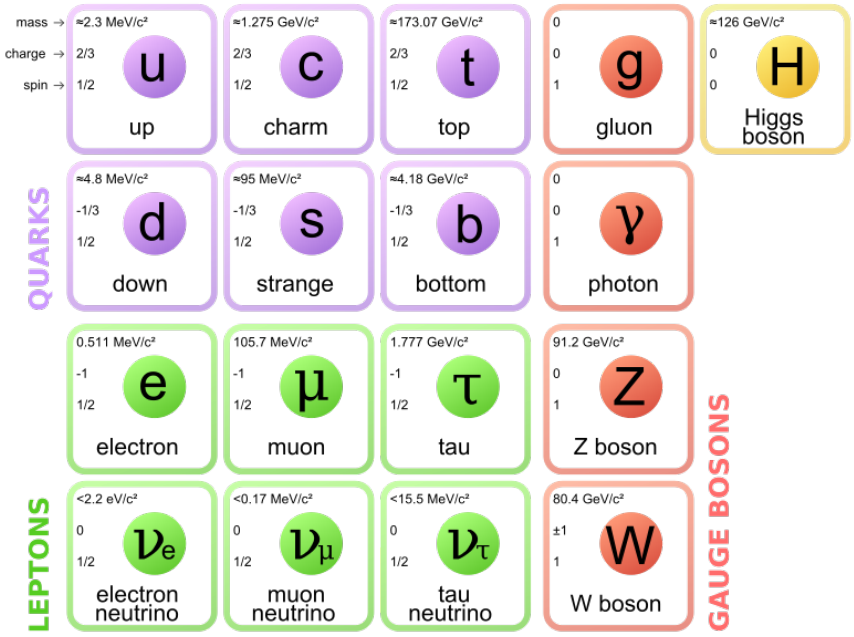

Figure 2.1: Particle content of the Standard Model. Notice the mass scale of neutrinos compared with that of other fundamental particles. Reproduced from [10].

2.1 Neutrino Masses and Mixing

First indication of the Neutrino Oscillation phenomenon was obtained by Ray Davis's Homestake Experiment [11] in the late 1960s, where he observed a shortage of electron neutrinos coming from the Sun with respect to the prediction of the Standard Solar Model [12]. This discrepancy supported the idea of the neutrino mass, which require a modification of the Standard Model of Particle Physics.

Different experiments [13, 14, 15] confirmed this deficit, until in June 2001, the SNO experiment [16] published the first clear evidence of solar neutrino oscillation [17]. Previously, the Super-Kamiokande experiment [18] had published evidence for atmospheric neutrino oscillation as early as 1998. These results then agreed with those obtained by the K2K experiment [19] using a neutrino beam. The K2K results were the first positive measurement of neutrino oscillations in which both the source and detector were fully under experimenter's control. The KamLAND experiment [20], with only 145 days of data during 2002, reported its first results of a high precision observation of reactor neutrino oscillation.

In 1957, Bruno Pontecorvo, following the ideas developed by Maki, Nakagawa and Nakata [21], proposed the idea of neutrino oscillation arising from a mixture between the flavour and mass eigenstates of neutrinos [22]. A neutrino created in a weak interaction with a flavour α has a non zero probability to be detected in a distinct flavour state β after traveling a distance z due to a slight difference in the masses of the mass eigenstates. A flavour state can be expressed mathematically as a combination of the three mass eigenstates:

$$| \nu_\alpha \rangle = \sum_i U^*_{\alpha i} | \nu_i \rangle \tag{2.1}$$

where $| \nu_\alpha \rangle$ is a neutrino with flavour α = e (electron), μ (muon) or τ (tau), and $| \nu_i \rangle$ is a neutrino with definite mass m_i *(i = 1, 2, 3).* $U_{\alpha i}$ represents the αi entry of the Pontecorvo-Maki-Nakagawa-Sakata (PMNS)

lepton mixing matrix:

$$U = \begin{pmatrix} U_{e1} & U_{e2} & U_{e3} \\ U_{\mu 1} & U_{\mu 2} & U_{\mu 3} \\ U_{\tau 1} & U_{\tau 2} & U_{\tau 3} \end{pmatrix} \tag{2.2}$$

If this matrix were the identity matrix, then the flavour eigenstates would be the same as the mass eigenstates. However, the experimental data show that this is not the case. When the standard three neutrino theory is considered, the standard parametrization of the matrix is

$$U = \begin{pmatrix} c_{12}c_{13}e^{i\alpha_1/2} & s_{12}c_{13} & s_{13}e^{-i\delta} \\ -s_{12}c_{23} - c_{12}s_{23}s_{13}e^{i\delta} & (c_{12}c_{23} - s_{12}s_{23}s_{13}e^{i\delta})e^{i\alpha_2/2} & s_{23}c_{13} \\ s_{12}s_{23} - c_{12}c_{23}e^{i\delta} & -c_{12}s_{23} - s_{12}c_{23}s_{13}e^{i\delta} & c_{23}c_{13} \end{pmatrix} \tag{2.3}$$

where α_1 and α_2 are the two Majorana phases which exist only if neutrinos are Majorana particles. The phases α_1 and α_2 together with the phase factor δ are different from zero only if neutrinos violate CP symmetry. The parameter c_{ij} means $\cos\theta_{ij}$ and s_{ij} means $\sin\theta_{ij}$, where θ_{ij} is the mixing angle between neutrino masses.

The mixing angle θ_{23} between μ and τ neutrino, was first measured by the Super-Kamiokande experiment using atmospheric neutrinos produced from the decays of particles resulting from interactions of cosmic rays with Earth's atmosphere [23], while the mixing angle θ_{12} was first measured by the KamLAND experiment using reactor anti-neutrinos and later confirmed by the SNO experiment [24]. Recently, in 2013, a precise measurement of the the last mixing angle θ_{13} was measured by the T2K experiment [25], confirming the previous measurements announced by the Daya Bay reactor neutrino experiment and the RENO experiment [26, 27]. The up-to-date experimental values are presented in Table 2.1.

The only mass information available from oscillation experiments is the square mass differences of the eigenstates and not the absolute

Parameter	Best fit $\pm 1\sigma$ (eV^2)
$sin^2(\theta_{12})$	$0.304^{+0.012}_{-0.012}$
$sin^2(\theta_{23})$	$0.451^{+0.001}_{-0.001}$
$sin^2(\theta_{13})$	$0.0219^{+0.0010}_{-0.0011}$
Δm^2_{21}	$(7.50^{+0.18}_{-0.19}) \times 10^{-5}$ eV^2
$\lvert\Delta m^2_{32}\rvert$	$(2.473^{+0.070}_{-0.067}) \times 10^{-3}$ eV^2
Δm^2_{31}	$= \Delta m^2_{32} + \Delta m^2_{21} \simeq \Delta m^2_{32}$

Table 2.1: Neutrino mixing angles and experimental measurement of Δm^2_{ij} according to global oscillation analysis [28].

mass scale:

$$\Delta m^2_{ij} = m^2_i - m^2_j \tag{2.4}$$

The difference between the eigenstates m_2 and m_1 has been measured using solar and reactor experiments ($\Delta m^2_{\mathrm{sol}}$), while atmospheric and accelerator-based experiments have measured the difference between the eigenstates m_3 and m_2 ($\Delta m^2_{\mathrm{atm}}$). The current experimental values are presented in Table 2.1.

The current results of neutrino oscillation experiments cannot establish the absolute mass scale, which must be determined by other means [29] (see § 2.2). Moreover, the sign of Δm_{32} has not yet been determined to date, leaving open two possible ordering of the mass states: *"normal"*, where m_1 is the lightest eigenstate and m_3 the heaviest, or *"inverted"*, where m_3 is the lightest and m_2 the heaviest eigenstate (see Figure 2.2).

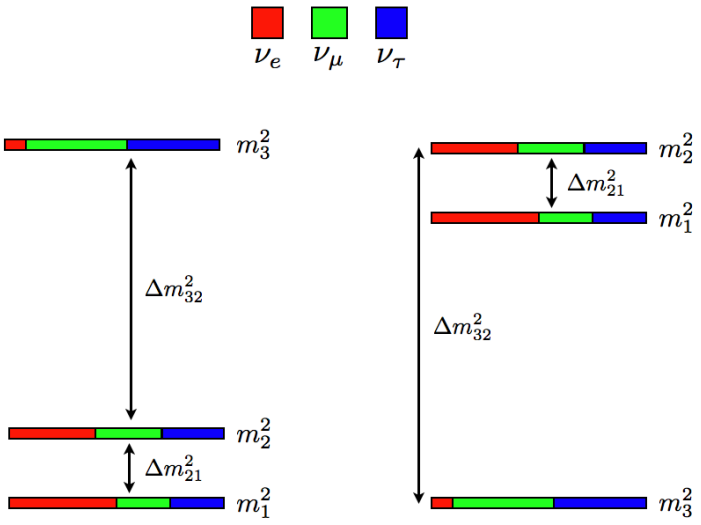

Figure 2.2: Representation of the two possible neutrino mass orderings. Left corresponds to the *"normal"* ordering, where m_1 is the lightest neutrino mass eigenstate, while right is the *"inverted"* ordering, if m_3 is the lightest eigenstate.

2.2 Experimental Neutrino Mass Measurement

Neutrino oscillation experiments provide only information about relative differences between the mass eigenstates, not the absolute mass values. The measurement of the mass scale is sought in three primary ways: directly, via radioactive β decay and μ decay, by cosmological observations and via measurement of the rate of neutrinoless double beta decay (§ 2.5).

Measurement with β decay

Ideally, the simplest way to measure the absolute neutrino mass is to look at the energy spectrum of the electron emitted by a β decay source, also called the *Kurie plot* (Figure 2.3). In beta decay, an electron and an anti-neutrino are emitted, whit the total transition energy (Q_β) being distributed between their kinetic energies, the electron mass and the electron anti-neutrino mass. The difference between the maximum energy released by the β particle and the Q_β value can provide an estimation of the effective electron neutrino mass (m_β). However, this measurement is very challenging due to the small mass of the neutrino, smaller than 1 eV [30].

Different experiments have employed this technique, most of them using tritium as the source ($Q_\beta = 18570$ eV). The Troitsk experiment [31] and the Mainz experiment [32], established an upper limit for the electron neutrino mass of 2.5 eV and 2.3 eV respectively, giving a combined limit of 2 eV [8]. The KATRIN experiment [33] is expected to improve the current limit by almost an order of magnitude reaching a sensitivity to the electron neutrino mass of 0.30 eV with 3 sigma significance and 0.35 eV with 5 sigma significance.

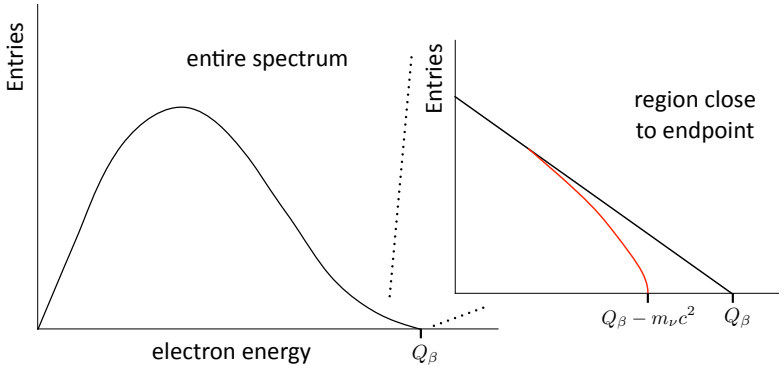

Figure 2.3: Energy spectrum of beta decay showing the endpoint region. The black line corresponds to zero neutrino mass and the red line to finite neutrino mass.

Measurement with Cosmology

Neutrinos are the second largest population of particles in the Universe, behind photons. Therefore, massive neutrinos would have produced a measurable effect in the Universe's structure [34]. The study of the distribution of galaxies in the Universe together with the Cosmic Microwave Background (CMB), provide an upper limit for the sum of all neutrino masses ($\sum m_i$) [34]. In the past, different NASA missions have explored this idea, like the Wilkinson Microwave Anisotropy Probe (WMAP) [35] and the 2dFGRS [36]. More recently, *the Planck satellite* [37] operated by the European Space Agency, has presented its results in 2013. *Planck* data, in combination with the data measured by WMAP, sets a constraint of $\sum m_i < 0.23\,eV$ (0.95% CL) [37]. At the same time, Planck data alone provides no evidence for extra neutrino mass eigenstates, beyond the known three states.

2.3 Dirac or Majorana Neutrinos

Neutrinos were introduced in the Standard Model (SM) of Particle Physics as massless particles; however, experimental observations, as the ones described in § 2.1, require the SM to be modified in order to include a neutrino mass term.

The question of how neutrino masses arise has not been answered conclusively. In the Standard Model, fermion masses result from the Yukawa interactions with the Higgs field. These interactions involve both left and right-handed fermions. However, only left-handed neutrinos have been observed experimentally [38].

For that reason, neutrinos may have another source of mass, which must be included in the SM. Two possibilities are normally considered to introduce a possible neutrino mass term. We discuss them in the following.

Dirac mass term

A Dirac neutrino mass can be generated with the same Higgs mechanism that gives masses to quarks and charged leptons, with the only introduction in the SM of right-handed components $\nu_{\alpha R}$ of the neutrino fields ($\alpha = e, \mu, \tau$) [39, 40].

$$\nu_L = \begin{pmatrix} \nu_{eL} \\ \nu_{\mu L} \\ \nu_{\tau L} \end{pmatrix} \quad \nu_R = \begin{pmatrix} \nu_{eR} \\ \nu_{\mu R} \\ \nu_{\tau R} \end{pmatrix} \tag{2.5}$$

This model is usually called the *minimally extended Standard Model*. These right-handed neutrino fields are called *sterile* [40] because they do not participate in weak, strong or electromagnetic interactions, their only interaction being gravitational. On the other hand, the normal left-handed neutrino fields that participate in weak interactions are usually called *active*.

In the minimally extended Standard Model with three right-handed neutrinos, the SM Higgs-lepton Yukawa Lagrangian which generates the masses of fermions is represented as

$$\mathcal{L}_{H,L} = -\sum_{\alpha,\beta=e,\mu,\tau} Y'^{\ell}_{\alpha\beta}\,\overline{L_{\alpha L}}\,\Phi\,\ell'_{\beta R} - \sum_{\alpha,\beta=e,\mu,\tau} Y'^{\nu}_{\alpha\beta}\,\overline{L_{\alpha L}}\,\Phi^{*}\,\nu'_{\beta R} + H.c. \qquad (2.6)$$

where Y'^{ℓ} and Y'^{ν} are the complex 3×3 matrix of Yukawa couplings for charged leptons and neutrinos respectively, the leptonic weak-isospin doublets are represented by $L_L \equiv (\nu_{\ell L}\,\ell_L)$, ℓ_R (with $\ell = e,\mu,\tau$) are the leptonic weak-isospin singlets, and Φ is the scalar Higgs doublet.

After spontaneous symmetry breaking, this Lagrangian can be written in matrix form as

$$-\mathcal{L}_{H,L} = \Big(\frac{v+H}{\sqrt{2}}\Big)\Big[\overline{\ell'_L}\,Y'^{\ell}\,\ell'_R + \overline{\nu'_L}\,Y'^{\nu}\,\nu'_R\Big] + H.c. \qquad (2.7)$$

where v is the vacuum expectation value (VEV) of the Higgs doublet and H is the Higgs boson field. Introducing in the Lagrangian the Dirac neutrino fields

$$\nu_i \;=\; \nu_{iL} + \nu_{iR}\,;\;\; (i = 1,2,3) \qquad (2.8)$$

for neutrinos we finally obtain

$$-\mathcal{L}_{H,L} \;=\; \Big(\frac{v+H}{\sqrt{2}}\Big)\sum_{i=1}^{3} y_i^{\nu}\,\overline{\nu_{iL}}\,\nu_{iR} + H.c. = \sum_{i=1}^{3} M_D\,\overline{\nu_i}\,\nu_i \qquad (2.9)$$

where y^{ν} are elements of the complex non-diagonal matrix M_D, known as Dirac mass matrix. In this model, the neutrino masses are defined by

$$m_{D_i} \equiv \frac{y_i^{\nu}\,v}{\sqrt{2}}\,;\;\; (i = 1,2,3) \qquad (2.10)$$

The neutrino masses obtained using this mechanism are proportional to the Higgs VEV v, like the masses of charged leptons and

quarks. However, it is known that the masses of neutrinos are much smaller than those of charged leptons and quarks, and this mechanism gives no explanation of the very small values of the neutrino Yukawa couplings that are needed, making the explanation of neutrino masses with a Dirac mass term alone unsatisfactory.

Majorana mass term

A Majorana mass term can be added to the SM considering a chiral fermion field alone, if the other chiral field can be expressed in terms of the first. This idea was proposed by Ettore Majorana in 1937 [9] when he realized that for neutral particles (like neutrinos)

$$\nu_R \rightarrow (\nu_L)^c = C\,\bar{\nu}_L^T \tag{2.11}$$

where C is the operator of charge conjugation. Neutrinos are the only SM fermions for which this possibility is compatible with charge conservation [40], and therefore a Majorana mass term can be included in equation 2.9 as

$$\mathcal{L}_{mass}^{M,L} = -\frac{1}{2}\, m_L\, \overline{\nu_L^c}\, \nu_L + H.c \tag{2.12}$$

where m_L is a free parameter with dimensions of mass for left-handed neutrinos. If the right-handed neutrino field introduced previously also exists and is independent, a different Majorana mass term can be obtained with the same Lagrangian

$$\mathcal{L}_{mass}^{M,R} = -\frac{1}{2}\, m_R\, \overline{\nu_R^c}\, \nu_R + H.c \tag{2.13}$$

In addition, as a consequence of equation 2.11, which converts a chiral field into the opposite by the charge conjugate, a neutrino is converted into its own antiparticle, violating the SM total lepton number by two units [39].

2.4 The *see-saw* Mechanism

There exist at present strong arguments in favor of the Majorana nature of massive neutrinos. These arguments are based on the fact that neutrino masses are much smaller than the masses of quarks and leptons as depicted in Figure 2.1.

The most natural explanation of the smallness of neutrino masses is based on the assumption that the total lepton number is violated by a right-handed Majorana mass term at a large scale; this is the famous *see-saw* mechanism [41, 42, 43, 44] of neutrino mass generation. The simplest version of the mechanism (*see-saw* Type 1) predicts the existence of a light left-handed neutrino state (m_1) and a corresponding very heavy right-handed neutrino state (m_2), which has yet to be observed. According to this model [39], the masses are of the order of

$$m_1 \simeq \frac{m_D^2}{m_R} \;\; ; \;\; m_2 \simeq m_R \tag{2.14}$$

This assumption indicates that the light neutrino of mass m_1 would be the main components of the left-handed neutrinos already observed, while a very heavy neutrino of mass m_2 forms the right-handed neutrinos, not observed because of the extremely high energies needed to produce them, close to the grand unification energy [39].

Confirming the Majorana nature of neutrinos would be one of the greatest achievements in modern physics. Many theoretical models of the Universe require neutrinos to be Majorana particles. However, there is currently only one realistic experimental approach which can directly confirm this to be true, the observation of neutrinoless double beta decay. This decay, described in detail in § 2.5, would provide an unambiguous result confirming neutrinos as a distinct form of matter than the other leptons.

2.5 Double Beta Decay

Double beta decay ($\beta\beta$) is a very rare nuclear transition in which a nucleus with Z protons decays into a nucleus with $Z + 2$ protons and same mass number A. It can only be observed in those isotopes where the β decay mode is forbidden due to the energy of the daughter nuclei being higher than the energy of the parent nuclei, or highly suppressed. If this condition is fulfilled, two simultaneous β-decays are possible.

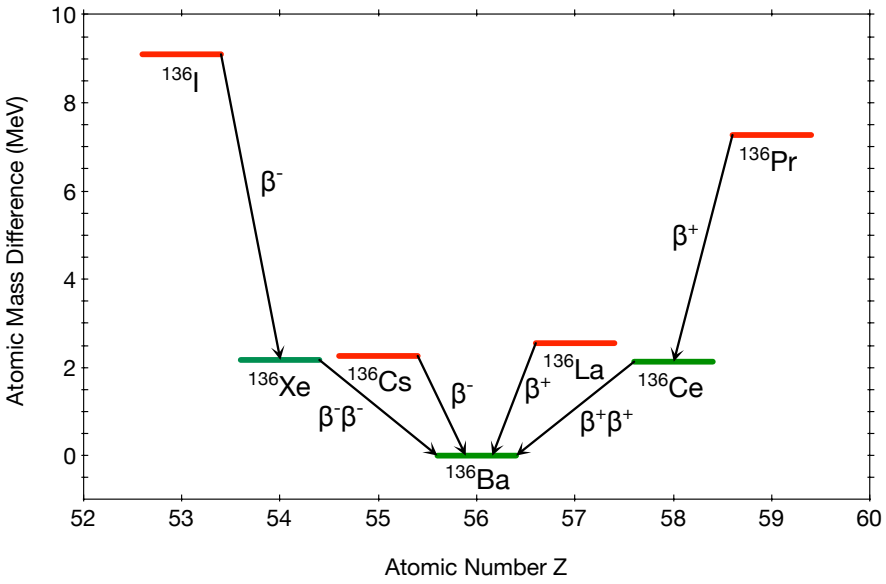

Figure 2.4: Atomic masses of isotopes with $A = 136$ given as differences with respect to the most bound isotope, ^{136}Ba. The red levels indicate odd-odd nuclides, whereas the green indicate even-even ones. The arrows show the type of nuclear transition connecting the levels. Double beta (either plus or minus) transitions are possible because the intermediate state ($\Delta Z = \pm 1$) is less bound, forbidding the beta decay [45].

Two $\beta\beta$ decay modes are normally considered. The standard two neutrino double beta decay mode ($\beta\beta 2\nu$)

$$ {}^{A}_{Z}X \rightarrow {}^{A}_{Z+2}\,Y + e^{-}_{1} + e^{-}_{2} + \bar{\nu}_{e_1} + \bar{\nu}_{e_2} \tag{2.15} $$

was proposed by Goeppert-Mayer in 1935 [46] and has been observed in several nuclei, where an anti-neutrino associated to each electron is emitted. This process has typical lifetimes on the order of $10^{18} - 10^{21}$ years.

The neutrinoless double beta decay mode ($\beta\beta 0\nu$)

$$ {}^{A}_{Z}X \rightarrow {}^{A}_{Z+2}\,Y + e^{-}_{1} + e^{-}_{2} \tag{2.16} $$

where the electrons carry essentially all the energy released in the decay. This process, which was postulated by Furry in 1939 [47] and has not been observed yet, is forbidden in the Standard Model of Particle Physics. The Feynman diagrams for both possible decays are represented in Figure 2.5.

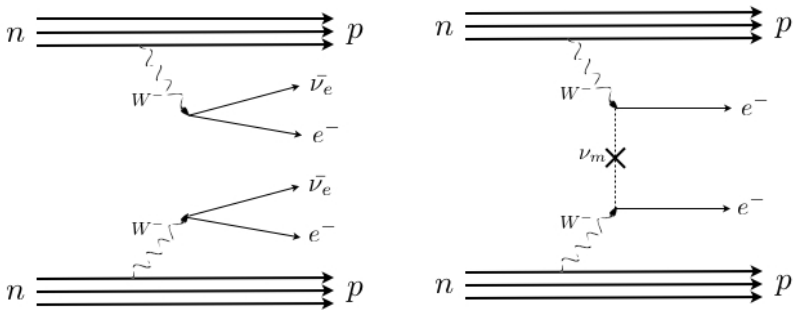

Figure 2.5: Feynman diagram for the $\beta\beta 2\nu$ (left) and the $\beta\beta 0\nu$ (right).

Only if neutrinos are massive, Majorana particles [48], and therefore their own antiparticles, $\beta\beta 0\nu$ can take place. The anti-neutrino created in a vertex from one β decay virtually propagates to the other

Decay	Energy (keV)	Half-life (10^{19} years)
$^{48}Ca \rightarrow {}^{46}Ta$	990.4 ± 2.4	$4.4^{+0.6}_{-0.5}$
$^{76}Ge \rightarrow {}^{76}Se$	2039.006 ± 0.050	160^{+13}_{-10}
$^{82}Se \rightarrow {}^{76}Kr$	2995.1 ± 2.0	9.2 ± 0.7
$^{96}Zr \rightarrow {}^{96}Mo$	1144.1 ± 2.0	2.35 ± 0.2
$^{100}Mo \rightarrow {}^{100}Ru$	3034 ± 6	0.711 ± 0.04
$^{116}Ca \rightarrow {}^{116}Sn$	2805 ± 3.8	2.85 ± 0.15
$^{130}Te \rightarrow {}^{130}Xe$	2528.8 ± 1.3	69 ± 13
$^{136}Xe \rightarrow {}^{136}Ba$	2457.8 ± 1.4	220 ± 6
$^{150}Nd \rightarrow {}^{150}Sm$	3367.5 ± 2.2	0.82 ± 0.09

Table 2.2: Observed double beta decay isotopes and best measured half-life of the two neutrino mode [8].

vertex, where it acts as a neutrino producing an electron via inverse beta decay. As the neutrino acts in a vertex as a neutrino and in the other as an anti-neutrino, this process is only possible if both particles are the same. Additionally, the observation would demonstrate that total lepton number is violated in physical phenomena, an observation that could be linked to the cosmic asymmetry between matter and antimatter through the process known as leptogenesis [2, 3].

There are only thirty five natural isotopes which are able to undergo double beta decay. However, in most of them the probability of this happening is so low, or the signal of interest is in a range of energies where background is dominant, that it is practically impossible to observe. For this reason, the half-life of the two neutrino mode has only been measured for nine isotopes to date. Table 2.2 lists the properties of these observed double beta decay isotopes.

2.5.1 $\beta\beta0\nu$ Rate

As mentioned above, $\beta\beta0\nu$ can only be observed if neutrinos are massive Majorana particles. However, the probability for the decay to take place is low due to the different helicity h states required at each vertex. The helicity is the projection of the spin $\vec{S}$ onto the momentum vector $\vec{p}$ and can be defined as a linear combination of chirality states

$$h = A \cdot \nu_L + B \cdot \nu_R \tag{2.17}$$

where ν_L and ν_R represent respectively the chiral fields *left-handed* and *right-handed*, and A and B their weight factors. The first vertex produces a $\bar{\nu}_e$ which is predominantly composed of the right-handed chiral state, however, only the chiral field ν_L can interact with the second vertex, so this interaction depends on the weight of the factor A, which is proportional to $(m_\nu/E)^2$ [39]. Therefore, the probability of this disintegration depends directly on the neutrino mass.

The lifetime for the $\beta\beta0\nu$ process, if mediated by light Majorana neutrino exchange, can be expressed by

$$(T_{1/2}^{\beta\beta0\nu}) = G^{\beta\beta0\nu} \, |M^{\beta\beta0\nu}|^2 \, m_{\beta\beta}^2 \tag{2.18}$$

where $G^{\beta\beta0\nu}(E_0, Z)$ is an exactly-calculable phase-space factor for the emission of two electrons, $M^{\beta\beta0\nu}$ is the nuclear matrix element (NME) of the transition, which has to be evaluated theoretically; and $m_{\beta\beta}$ is the *effective Majorana mass* of the electron neutrino

$$m_{\beta\beta} = \left| \sum_i U_{\alpha i}^2 \, m_i \right| \tag{2.19}$$

where m_i are the neutrino mass eigenstates and $U_{\alpha i}$ are elements of the neutrino mixing matrix as described in § 2.1.

Even in the case of a negative result, it is still possible to constrain the parameter $m_{\beta\beta}$ and the value of the lowest mass eigenstate. The

relationship between $m_{\beta\beta}$ and the neutrino masses m_i is affected by the uncertainties in the measured oscillation parameters, the unknown neutrino mass ordering (*normal* or *inverted*), and the unknown phases in the neutrino mixing matrix. Figure 2.6 illustrates the relationship between $m_{\beta\beta}$ and the lightest neutrino mass m_{light}, which is equal to m_1 or m_3 in the *normal* and *inverted* mass orderings, respectively.

The upper bound on the *effective Majorana mass* corresponds to the experimental constraint set from $\beta\beta0\nu$ searches ($m_{\beta\beta} < 200$ meV) [49, 50], while the left bound correspond to cosmological constraints set by Planck data in combination with the data measured by WMAP [37] as explained in § 2.2.

2.5.2 Double Beta Decay Experiments

The main goal of basically all double beta decay experiments is to measure the total energy of the radiation emitted by a $\beta\beta$ source. In a neutrinoless double beta decay, the sum of the energies of the two emitted electrons is constant and equal to the mass difference between the parent and the daughter atoms ($Q_{\beta\beta}$). Any experiment hoping to measure the $\beta\beta0\nu$ half-life must be able to count the number of events at this energy due to $\beta\beta0\nu$. However, the measurement is limited by the experimental sensitivity of the detector employed, which can be expressed as

$$T_{1/2} \propto a \cdot \epsilon \cdot \sqrt{\frac{M \cdot t}{\Delta E \cdot B}} \tag{2.20}$$

where M is the isotope mass, t is the running time of the detector, ΔE is the energy resolution, B is the background rate in the energy region of interest, ϵ is the detection efficiency and a is a term which includes nuclear matrix elements.

Natural fluctuations and detector effects combine to smear the energy response and backgrounds from naturally occurring radioisotopes can pollute the energy region. For that reason, the materials with

which the detector is built must be selected carefully to reduce the natural radioactivity present in all materials. In addition, double beta decay experiments must be placed at underground facilities, in order to reduce the background levels from atmospheric radiation. Finally, the intrinsic background from the standard two neutrino double beta decay mode ($\beta\beta 2\nu$), which has a continuous energy spectrum, can be problematic if the energy resolution is not very good.

Three experiments of the present generation are taking data already. On the one hand, the GERDA experiment [51] looks for the neutrinoless double beta decay of ^{76}Ge at Laboratori Nazionale del Gran Sasso. In GERDA, high purity germanium detectors (HPGe) are arranged in strings and mounted in special low-mass holders made of ultra-pure copper and PTFE. The strings are suspended inside a vacuum-insulated stainless steel cryostat of 4.2 m diameter and 8.9 m height filled with LAr. A copper lining 6 cm thick covers the inner cylindrical shell of the cryostat. The cryostat is placed in a 590 m^3 water tank instrumented with PMTs which serves as a Cherenkov muon veto as well as a gamma and neutron shield. The GERDA Collaboration has published a measurement of the $\beta\beta 2\nu$ half-life of ^{76}Ge, $T^{2\nu}_{1/2}(^{76}\mathrm{Ge}) = (1.926 \pm 0.095) \times 10^{21}$ years [52] and a limit on the $\beta\beta 0\nu$ half-life, $T^{0\nu}_{1/2}(^{76}\mathrm{Ge}) > 2.1 \times 10^{25}$ years (90% C.L.) [53].

On the other hand, xenon-based detectors like KamLAND-Zen [54], a transparent balloon with a ∼3 m diameter, containing 13 tons of liquid scintillator loaded with 320 kg of xenon (enriched to 91% in ^{136}Xe), is suspended at the centre of a stainless steel spherical vessel with 1879 photomultiplier tubes mounted on the inner surface which record the scintillation light generated by $\beta\beta$ events occurring in the detector. With this configuration it has achieved an extrapolated energy resolution of 9.9% FWHM at the $Q_{\beta\beta}$ value of ^{136}Xe, publishing recently a limit on the half-life of $\beta\beta 0\nu$ of $T^{0\nu}_{1/2}(^{136}Xe) > 1.9 \times 10^{25}$ years [54].

In parallel, the EXO Collaboration has published a limit on the half-life of $\beta\beta 0\nu$ of $T^{0\nu}_{1/2}(^{136}Xe) > 1.6 \times 10^{25}$ years [55] using the EXO-200

detector, a symmetric LXe TPC filled with 110 kg of xenon (enriched to 91% in ^{136}Xe). In EXO-200, ionization charges in the xenon created by charged particles drift towards the two anodes of the TPC due to the presence of an electric field. Events in the chamber are reconstructed by a pair of crossed wire planes which measure their amplitude and transverse coordinates, and an array of avalanche photodiodes (APDs), which detect the xenon scintillation light. The EXO-200 detector has achieved an energy resolution of 4% FWHM at the $Q_{\beta\beta}$ value of ^{136}Xe.

The combination of the KamLAND-Zen and EXO results give a limit of $T^{0\nu}_{1/2}(^{136}Xe) > 3.4 \times 10^{25}$ years (120-250 meV, depending on the NME) [54]. This result excludes the claim of Klapdor-Kleingrothaus and collaborators [56].

In Chapter 3, a new neutrinoless double beta decay experiment is introduced, the *NEXT experiment*, which will search for neutrinoless double beta decay of ^{136}Xe at Laboratorio Subterráneo de Canfranc with the NEXT-100 detector. Such a detector, thanks to its excellent and demonstrated energy resolution, together with a high efficiency background rejection, will be one of the leading experiment in the field, exploring the region of neutrino mass lower than 100 meV [48].

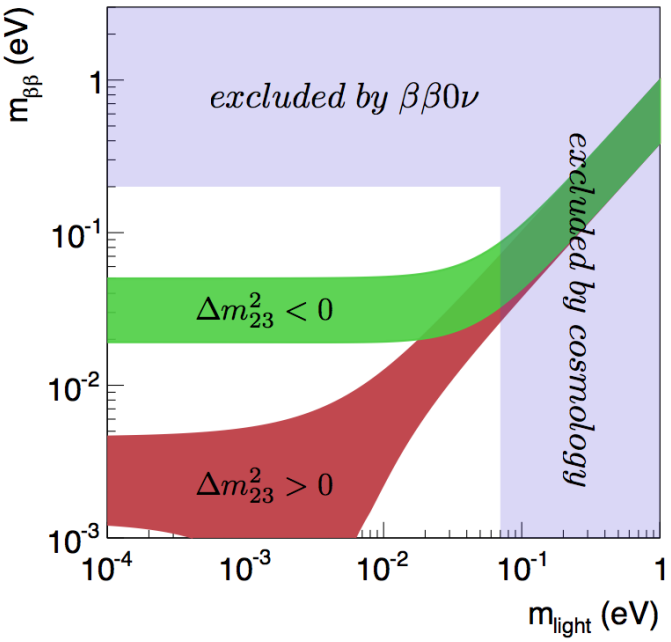

Figure 2.6: Effective neutrino Majorana mass, $m_{\beta\beta}$, as a function of the lightest neutrino mass, m_{light}. The green band corresponds to the *inverse* hierarchy of neutrino masses, whereas the red corresponds to the *normal* ordering. The upper bound on the lightest neutrino mass comes from cosmological bounds whereas the bound on the *effective Majorana mass* from $\beta\beta0\nu$ constraints.

A combination of luck and stubbornness, I think it is a good recipe in this field.

Dave R. Nygren

CHAPTER

3

The NEXT Experiment

The NEXT experiment[1], will search for the neutrinoless double beta decay of ^{136}Xe using a radiopure high-pressure xenon gas Time Projection Chamber (TPC) filled with 100 kg of Xe enriched in its ^{136}Xe isotope. The experiment will be located at *Laboratorio Subterráneo de Canfranc*, which is carved into the rock at 850 meters deep below the Tobazo Mountain, on the Spanish side of the Pyrenees.

NEXT will be the first large high-pressure gas TPC to use electroluminescence readout with SOFT (Separated, Optimized Functions TPC) technology. The following sections outline the most relevant aspects of xenon gas detectors, as well as describe the structure of the NEXT-100 detector. In addition, one of the prototypes with which the NEXT collaboration is demonstrating the feasibility of the SOFT concept is also presented, and its main features described.

[1] The acronym stands for *Neutrino Experiment with a Xenon TPC.*

3.1 Xenon Gas as Detection Medium

Gas detectors and, particularly, time projection chamber technology have been developed over a number of years and now find applications in a diverse range of fields. The relative ease with which noble gases can be cleaned of impurities as well as the availability of both scintillation and ionization signals when using these materials as detection media have meant that such detectors have been extensively used in medical imaging, dark matter detection, X-ray astronomy, and for the observation of double beta decay [57, 58, 59, 60].

Xenon, both as a gas and liquid, is of special interest for applications in which the energy of the interacting particle must be measured. This trait coupled with the existence of the ^{136}Xe isotope which can decay via the double beta mechanism makes xenon an attractive material for the search for neutrinoless double beta decay. ^{136}Xe constitutes only 8.86% of natural xenon, but the enrichment process is relatively simple and cheap compared to that of other $\beta\beta$ isotopes. Moreover, the two-neutrino decay mode of ^{136}Xe is slow, $T^{2\nu}_{1/2}(^{136}\text{Xe}) = 2.2 \cdot 10^{21}$ years [54, 61], and hence the experimental requirement for energy resolution is less severe than for other $\beta\beta$ sources.

Primary Ionization Yield

The energy released by charged particles as electrons in the $\beta\beta0\nu$ process, is divided into excitation and ionization of the xenon atoms. The first process is a resonant reaction in which the atomic electrons are promoted to higher energy levels:

$$X + \beta \rightarrow X^* + \beta \tag{3.1}$$

Upon de-excitation, the electrons previously promoted emit photons corresponding to their typical emission spectrum, with a peak at 172 nm in the UV region. If the energy transferred by the β particle is above a

threshold, an electron can be extracted and the atom suffers ionization resulting in the creation of electron-ion pairs:

$$X + \beta \rightarrow X^{+} + \beta + e^{-} \tag{3.2}$$

Both cases are described via Platzman's equation [62]:

$$E_{\beta} = < E_i > N_I + < E_{sci} > N_{sci} + \epsilon \tag{3.3}$$

where N_I is the number of electron-ion pairs ultimately produced with an average energy expenditure $< E_I >$, N_{sci} is the number of atoms excited at an average energy expenditure $< E_{sci} >$, and ϵ is the average kinetic energy of sub-excitation electrons, whose energy is lower than the excitation potential and eventually goes into heat.

To characterize the transfer efficiency of the absorbed energy into a measurable number of electron-ion pairs, a value of the energy acquired for production of an electron-ion pair is often used

$$W_I = < E_I > + (N_{sci}/N_I) \cdot E_{sci} \tag{3.4}$$

In the particular case of $\beta\beta0\nu$ of ^{136}Xe, where $W_I = 21.9$ eV [63], the average number of primary ionization electrons is equal to:

$$\bar{N_I} = \frac{Q_{\beta\beta}}{W_I} = \frac{2.458 \times 10^6 \text{ eV}}{21.9 \text{ eV}} \cong 112,237 \text{ electrons} \tag{3.5}$$

In absence of electric field, all electrons and ions liberated will recombine generating scintillation light. By applying an electric field, this process is rapidly reduced.

Electron collection efficiency

The presence of a drift field $\vec{E}$ to avoid recombination produces the drift of charges within the TPC. Under the applied electric field, electrons acquire a net motion in the opposite direction of the electric field, with

a stationary drift velocity $\vec{v_d}$, which is the average of the instantaneous velocities as $\vec{v_d} =< \vec{v}(t) >$. In presence of sufficiently low electric fields, drift velocity is proportional to the electric field [62]

$$\vec{v} = \mu\vec{E} \tag{3.6}$$

The proportionality factor μ is called *mobility*. At high fields, the drift velocity saturates, becoming independent of the field. The drift velocity of ions is several orders of magnitude smaller than that of the electrons.

The fact that ionization electrons drift toward the anode introduces an uncertainty in their collection. As they drift, due to the collisions with the xenon atoms, the ionization electrons deviate from the trajectories defined by the field lines spreading gaussianly in both the longitudinal and transverse directions. This diffusion limits the intrinsic position resolution of gaseous detectors. The magnitude of the spread is proportional to the drift time, t_d:

$$\sigma_L = \sqrt{D_L \cdot t_d}\,, \quad \sigma_T = \sqrt{D_T \cdot t_d}\,, \tag{3.7}$$

where D_L and D_T are, respectively, the longitudinal and transverse diffusion coefficients of the gas. In addition, electron *attachment* to electronegative impurities dissolved in the gas may lead to a significant decrease of the ionization signal during drift. This effect can be described, in general, by an exponential distribution:

$$N(t_d) = N(0) \cdot exp(-t_d/\tau) \tag{3.8}$$

where N is the number of drifting electrons, which is a function of the drift time, and τ is the electron lifetime in the gas, inversely proportional to the concentration of impurities. Sufficiently long electron lifetimes can be achieved by circulating the gas continuously through appropriate filters.

Detection of Primary Signals

Xenon scintillation light can be directly detected by commercial photosensors. However, the efficiency of those devices to VUV light is usually poor. For that reason, different wavelength shifter are used to convert the 172 nm light of xenon to the near-visible band, where photosensors have their photodetection peak.

Regarding ionization electrons, once these are produced and recombination avoided, the number is so low that their signal must be amplified. In gas detectors, this is typically done by applying an electric field with higher intensity than that applied for drifts. In the case that the amplification field gives to the primary ionization electrons energy above the ionization threshold of xenon, they will produce new electrons-ion pairs while drifting, which can produce new pairs, in a process called *avalanche*. Otherwise, if the amplification field is between the ionization and scintillation thresholds, primary ionization electrons will excite by inelastic collisions but do not ionize the atoms of xenon generating secondary scintillation photons. This process, known as *Electroluminescense* (EL), is illustrated in Figure 3.1. The intensity of the secondary scintillation light is orders of magnitude stronger than that of the primary scintillation. In addition, the EL signal is also longer because it is produced as electrons drift, a few μs compared to a few ns of the primary scintillation.

The advantage of EL amplification is that the fluctuations associated with this process are small, in contrast with the avalanche multiplication. That is because the energy of drifting electrons is mostly dissipated via the emissions of photons, which do not participate further in the process. Due to this circumstance, EL amplification can provide better energy resolution than other gas gain amplification processes [62].

Both gain and energy resolution have been measured by using Electroluminescense in a wide range of $\bar{E}/p$, where $\bar{E}$ is the electric field present in the EL region defined by the two meshes which origins the

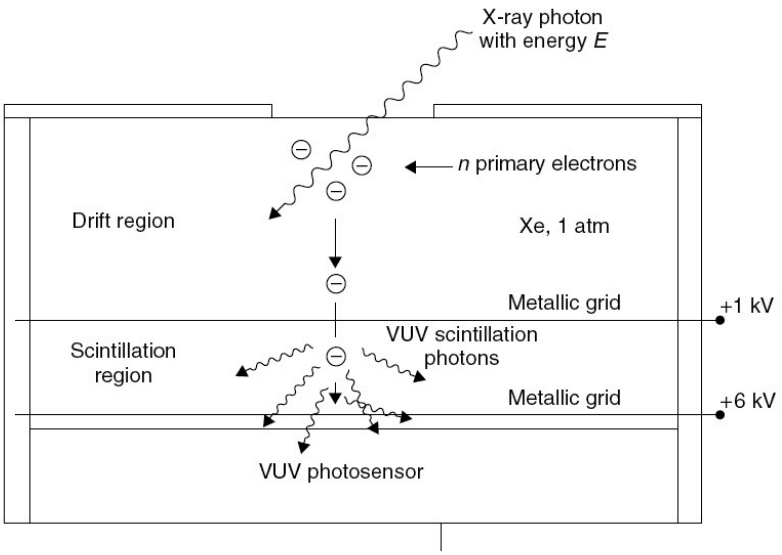

Figure 3.1: Principle of Electroluminescense generation process.

amplification, and p is the gas pressure. These results are represented in Figure 3.2, reproduced from [64]. Above $\bar{E}/p = 8-9$ V cm^{-1} torr^{-1} ($6-7$ kV cm^{-1} bar^{-1}), the electric field is such, that charge multiplication is produced by secondary ionization of the atoms, deteriorating rapidly the energy resolution. The best values of energy resolution are achieved with $3 < \bar{E}/p < 6$ kV cm^{-1} bar^{-1} ($4 < \bar{E}/p < 8$ V cm^{-1} torr^{-1}).

The absolute Electroluminescense gain under a uniform and constant $\bar{E}/p$ in xenon gas, defined as the number of scintillation photons produced by a single ionization electron, is given in [65] and represented by η as

$$\eta = 140 \cdot (\bar{E}/p - 0.83) \cdot p \cdot \Delta x \ \ (\text{UVphotons/e}^-) \tag{3.9}$$

where $\bar{E}/p$ is given in kV cm^{-1} bar^{-1}, p in bar, and the separation Δx between the meshes in cm.

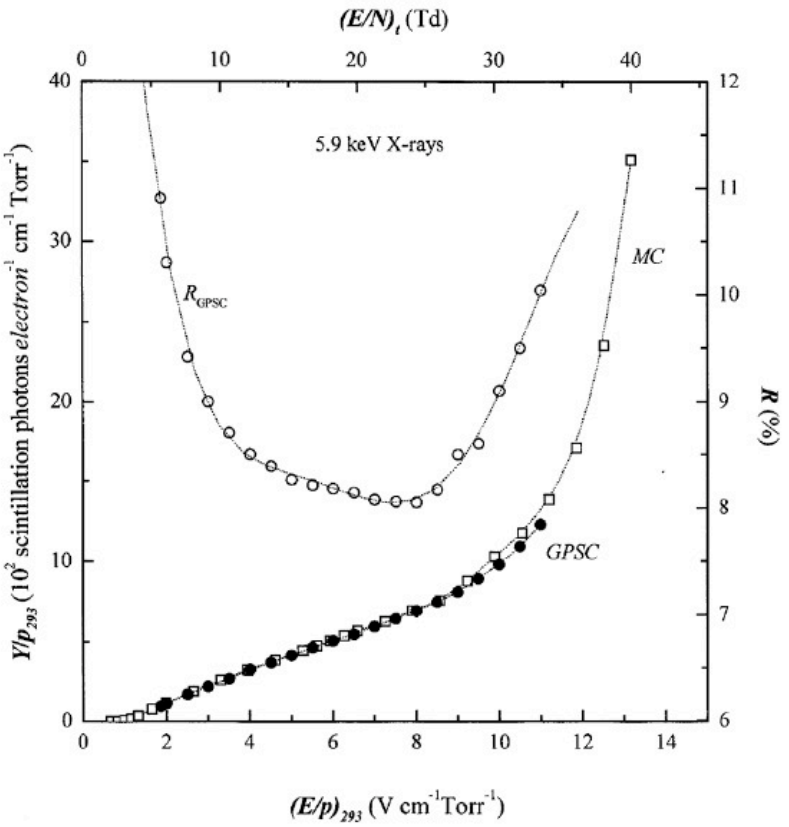

Figure 3.2: Reduced scintillation yield (open squares represent Monte Carlo results, while filled circles experimental results) and detector energy resolution (open circles) as a function of reduced electric field in the scintillation region for 5.9 keV X-rays. The experimental values are normalized to the calculated Monte Carlo values at $\bar{E}/p$ = 6 V cm^{-1} torr^{-1}, (4.5 kV cm^{-1} bar^{-1}) (from [64]).

3.2 Intrinsic Energy Resolution in Xenon Gas Detectors

Energy Resolution (ER) is a crucial ingredient for all $\beta\beta0\nu$ experiments. Due to intrinsic physical processes, there is a limit on the precision with which the energy can be measured in any detection medium.

In Gas Xe (GXe) detectors, a good measure of the energy deposited in the medium by ionizing particles is the number of ionization electrons produced in the process. If each ionization process could be considered independent of the others, the fluctuations would then be described by a Poisson distribution where the variance (σ^2) would be equal to the mean number of ionization electrons, N_I. However, the fluctuations in the mean number of ionization electrons present a lower value, as predicted by Fano's theory [66], being proportional to a factor F, known as the Fano Factor, which multiplies the mean primary ionization yield.

Therefore, the intrinsic fluctuations of the statistical ionization process are expressed by:

$$\sigma_I = (F \cdot N_I)^{1/2} \tag{3.10}$$

The Fano factor is typically less than 1, and can be as small as 0.05 for some Penning mixtures of noble gases [67]. For pure gaseous xenon, at low densities, various measurements [68, 69, 70] show that

$$F_{GXe} = 0.15 \pm 0.02 \tag{3.11}$$

This value is extremely small compared with the Fano factor of Liquid Xe (LXe) [71]:

$$F_{LXe} \approx 20 \tag{3.12}$$

resulting in an energy resolution much better in High Pressure Gas Xenon detectors. This effect can be observed in Figure 3.3, reported by Bolotnikov and Ramsey in [72], where energy resolution from the

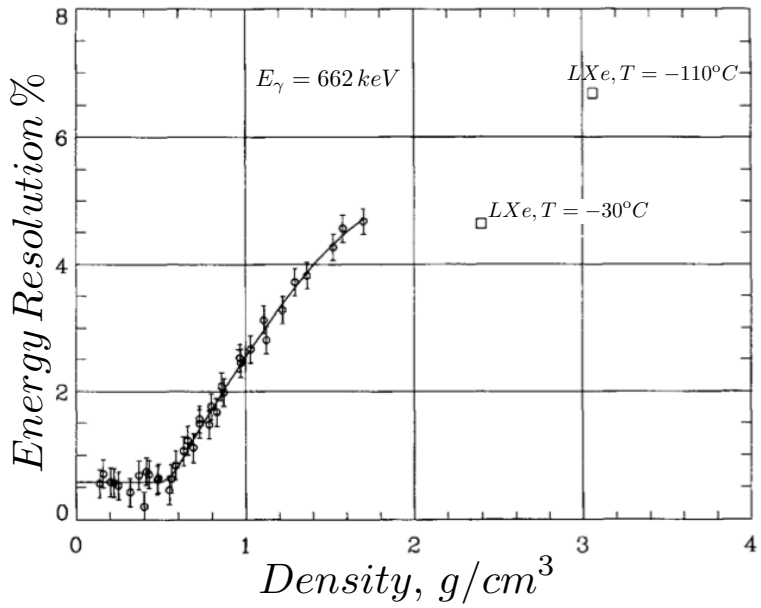

Figure 3.3: Energy resolution (% FWHM) of ^{137}Cs 662 keV γ-ray, as a function of xenon density for the ionization signal only, reproduced from[72].

photoelectric peak of a ^{137}Cs source (E_γ = 662 keV) is represented as a function of xenon density. Energy resolution presents a behavior practically constant at densities below $\rho_t \approx 0.55$ g/cm^3. For densities greater than ρ_t, energy resolution deteriorates rapidly, approaching a plateau at Liquid Xe density, disfavoring these detectors compared with Gas Xe detectors, where $\rho_{GXe} < \rho_t$.

However, other effects related to detection and amplification processes described in § 3.1, have an impact in energy resolution. Considering a as the amplification factor produced by an EL-based system amplification, it introduces a fluctuation in the detected signal, repres-

ented by a variance A (${\sigma_a}^2 = A$). In addition, electronic noise results from unavoidable random statistical fluctuations of the electric current when the charge carriers, such as electrons, traverse a gap. The current is a flow of discrete charges, and the fluctuation in the arrivals of those charges creates a continues noise function. Taking r as the fluctuations introduced in the detected signal by the electronic noise, the total fluctuation induced by the amplification system will be

$$A^* = (A^2 + r^2)^{1/2} \tag{3.13}$$

Under this condition, taking the measured signal of the detector as $\bar{D} = a \cdot N_I$, the variance in the detection process will be:

$$\sigma_{\bar{D}} = (A^* \cdot N_I)^{1/2} \tag{3.14}$$

If we consider that the fluctuations in the detection process are independent of the fluctuations in the primary ionization process, both contributions (equations 3.10 and 3.14) can be added in quadrature, and their sums described as:

$$\sigma_{\bar{D}} = ((A^* + F) \cdot N_I)^{1/2} \tag{3.15}$$

where A contain the fluctuations associated to the process of detecting a single electron, and F is a limitation on fluctuations in energy partitioning for a fixed total energy. Therefore, a good approximation for the energy resolution is:

$$\begin{aligned} \delta E/E &= 2\sqrt{2\,ln2} \cdot \sigma_{\bar{D}} \\ \delta E/E &= 2.35 \cdot ((A^* + F) \cdot N_I)^{1/2} \\ \delta E/E &= 2.35 \cdot ((A^* + F)\frac{W_I}{Q_{\beta\beta}})^{1/2} \end{aligned} \tag{3.16}$$

One of the goals for a good $\beta\beta0\nu$ detector is to have its fluctuations in the amplification system as small as possible, in principle as good

as F. In that case, where $F = A = 0.15$, the obtained energy resolution at $Q_{\beta\beta}$ value of ^{136}Xe would be:

$$\delta E/E = 3.84 \cdot 10^{-3} \text{ FWHM} \tag{3.17}$$

This value is in agreement with the one obtained in [73], where a GXe TPC with EL amplification was used to measure the energy resolution of a 122 keV γ-ray source. An energy resolution of 2.2 % FWHM was obtained at this energy, so if extrapolating as $E^{-1/2}$, the energy resolution at $Q_{\beta\beta}$ value of ^{136}Xe would be

$$\delta E/E = 4.4 \cdot 10^{-3} \text{ FWHM} \tag{3.18}$$

This result shows that in a high pressure TPC using EL amplification the factor A can be as small as the Fano factor, optimizing energy resolution. In contrast, this factor would be much larger for the case of avalanche-based read-out where typical values are in the range 0.2 to 0.9 [74, 75].

3.3 Tracking for Background Rejection

There are many types of events which can release an energy similar to the $Q_{\beta\beta}$ value of xenon, and therefore be confused with $\beta\beta0\nu$ events. For that reason, as important as energy resolution is the capability to identify the track of the particles which have crossed the detector.

Double beta decay events have a distinctive topological signature in GXe. As the electrons propagate through the xenon, they suffer multiple scattering with the xenon atoms. During this process, the deposited energy per unit path is constant $\frac{dE}{dx} \approx 70 \frac{\text{keV}}{\text{cm}}$ [76]. However, as the electrons's energy decreases, the number of scattering interactions increases, producing a larger deposition or blob at the end of the track, about 30 cm long at 10 bar. This behavior is illustrated in Figure 3.4.

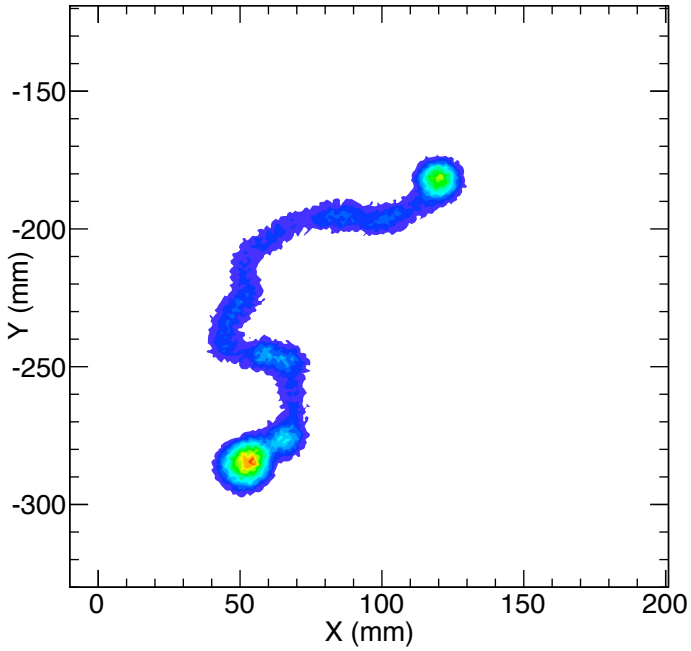

Figure 3.4: Monte Carlo simulation of the topological signature of a $\beta\beta0\nu$ event in NEXT, a track that ends in two "blobs" of energy. The trajectory of electrons are dominated by multiple scattering in the dense gaseous xenon [45].

The capability of reproducing the track of the particle in GXe allows the discrimination of background events which do not follow the described topology. The main background sources in the NEXT experiment are the gamma lines at 2.615 MeV from ^{208}Tl and at 2.448 MeV from ^{214}Bi. These isotopes are produced at the lower part of the natural radioactive chains of ^{232}Th and ^{238}U respectively as follows

1. For the 2.615 MeV line, the Compton edge is well below $Q_{\beta\beta}$, but a scattered gamma can interact and produce other electron

tracks close enough to the initial Compton electron, so they can be reconstructed as a single object falling in the energy Region of Interest (ROI). These photons can also be scattered outside the detector and then suffer photoelectric absorption inside contributing to the ROI. In addition, photoelectric electrons from the 2.615 MeV emission are produced above the ROI but can lose energy via bremsstrahlung and populate the energy window, if the emitted photons escape out of the detector.

2. The gamma line at 2.448 MeV is dangerous in spite of its low intensity (1.57%) because it is very close to $Q_{\beta\beta}$.

It is possible for the energy of such events to be reconstructed within the ROI, however, the topology of a single electron track differs from that of a $\beta\beta0\nu$ track. Identifying the endpoints of the topological information in XYZ and comparing the energy within a set radius of each can effectively differentiate signal and background.

Figure 3.5 shows the energy ROI of ^{136}Xe with the different background events which can fall on it and can be rejected by their topological reconstruction.

3.4 The SOFT Concept

The NEXT detector uses the Separated, Optimized Functions TPC (SOFT) concept (Figure 3.6), which consists in the idea that tracking and energy measurements are performed separately [77]. Using this concept, both energy resolution and tracking described in the previous sections can be achieved. When a charged particle interacts with the high pressure xenon, ionizes and excites its atoms. The excitation energy results is the prompt emission of VUV ($\sim$ 172 nm) scintillation light (S1) which is detected by a plane of PMTs located behind a transparent cathode, in one side of the TPC and giving the start-of-event (t_0).

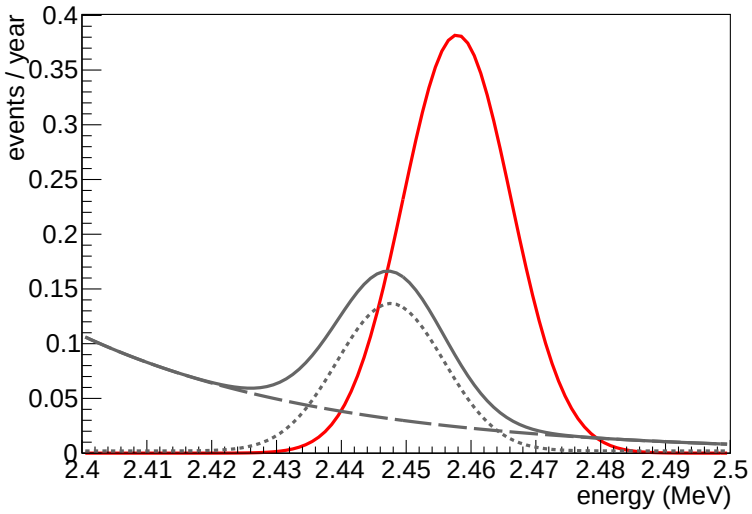

Figure 3.5: Energy spectra of signal (red, solid curve) and background (^{208}Tl: grey, dashed distribution; ^{214}Bi: grey, dotted distribution; total: grey, solid distribution) in the region of interest (ROI) around $Q_{\beta\beta}$. The signal strength represented here corresponds to a neutrino Majorana mass of 200 meV, while the backgrounds are scaled to their expected values in NEXT-100 (6×10^{-4} counts/(keV $\cdot$ kg $\cdot$ y)), assuming an exposure of 91 kg yr [45].

The ionization electrons left by the passage of the charged particle are prevented from recombining by an electric field which causes them to drift towards the TPC anode where they enter a region of more intense electric field between two meshes. In this region they are accelerated and induce the production of secondary excitation of xenon atoms without secondary ionization, by Electroluminescence amplification.

The EL light (S2) is generated a few millimeters away from an array of Silicon Photomultipliers (SiPMs), which form the *tracking plane*, providing the track of the event. As EL light is emitted isotropically,

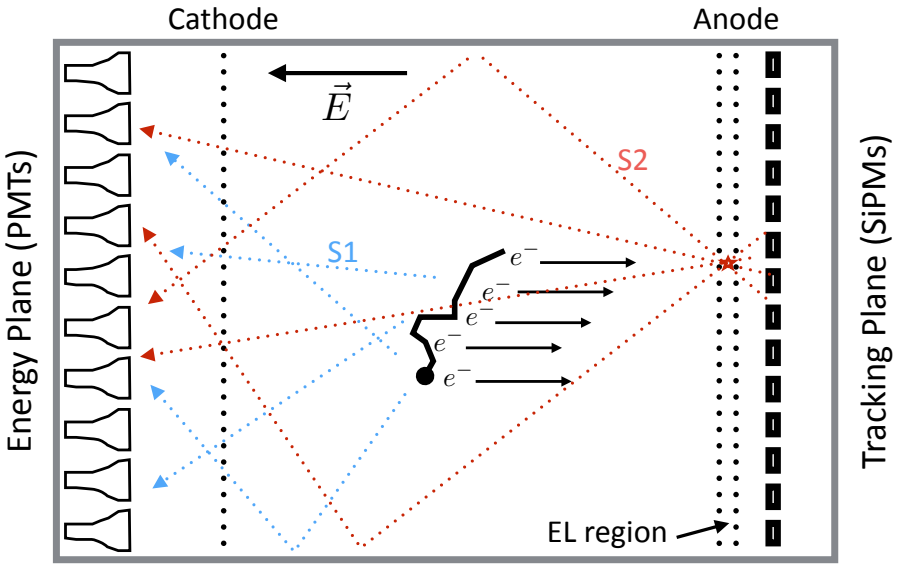

Figure 3.6: The Separated, Optimized Functions TPC (SOFT) concept. EL light generated at the anode is recorded in the photosensor plane right behind it and used for tracking. It is also recorded in the photosensor plane behind the transparent cathode and used for a precise energy measurement.

roughly half will reach the PMT plane, since now *energy plane*, giving a precise energy measurement.

The advantage of the separate functions for the two measurements is the decoupling of the operational configuration between the two planes of sensors, which gives more freedom to modify the operational parameters of each set, optimizing the performance of the whole detector.

3.5 The NEXT-100 detector

Based on the ideas described in the previous sections, *The NEXT Collaboration* plans to build the NEXT-100 detector, shown in Figure 3.7, which will search for neutrinoless double beta decay in ^{136}Xe. Such a detector will take advantage of the low noise introduced by an EL-based amplification system, to measure the ionization electrons produced by β-particles in high pressure GXe using an asymmetric Time Projection Chamber (TPC). The detector is designed to hold a maximum of 100 kg of xenon.

The NEXT-100 TPC is located inside a pressure vessel able to withstand high pressure xenon up to 15 bar, which is continuously purified by a gas system. Electroluminescence light is recorded by both energy and tracking planes located behind cathode and anode respectively, while their signals are processed by custom-designed electronics. The full system is contained inside a shielding infrastructure to protect the detector from the surrounding background. Besides, the activity of the lower part of ^{232}Th and ^{238}U chains (^{208}Tl and ^{214}Bi isotopes) from the components of the set-up and at the laboratory is the main concern in NEXT. For that reason, the materials included in the detector have been chosen according to their radiopurity properties, after an exhaustive screening campaign [78].

In the following sections, the different parts of the detector will be introduced, describing the most outstanding technological aspects. More details can be found in the *"Technical Design Report (TDR)"* [60] of the NEXT-100 detector.

3.5.1 Pressure Vessel

The pressure vessel is formed by a cylindrical structure made of stainless steel, with two identical torospherical heads on each end. The

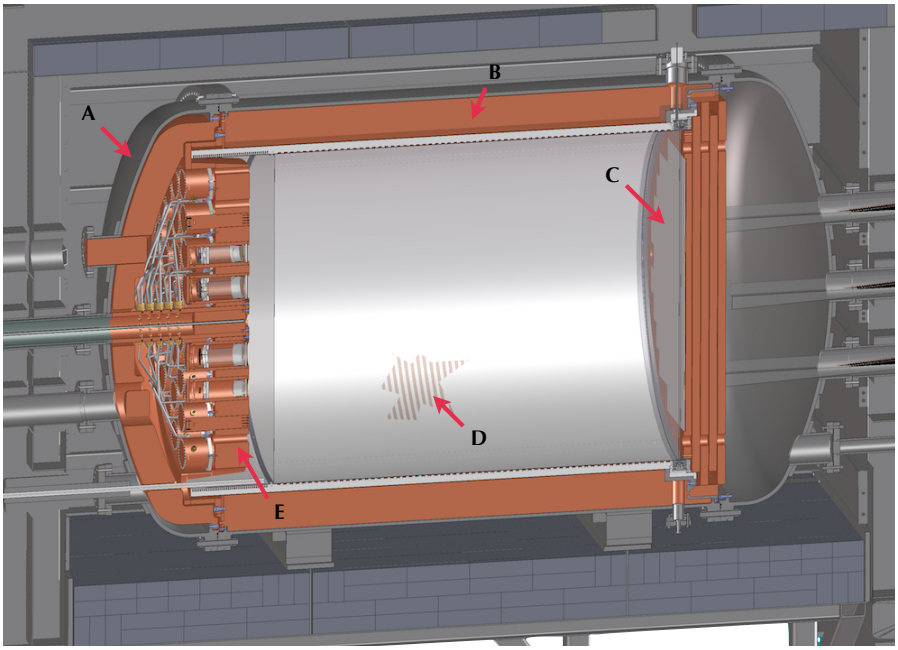

Figure 3.7: Cross-section view of the NEXT-100 detector inside its lead castle shield. A stainless-steel pressure vessel (A) houses the electric-field cage (D) and the two sensor planes (energy plane, E, and tracking plane, C) located at opposite ends of the chamber. The active volume is shielded from external radiation by at least 12 cm of copper (B) in all directions [45].

Parameter	Dimension
Maximum operating pressure (differential)	14.0 bar
Maximum allowable working pressure (differential)	15.4 bar
Maximum allowable external pressure (differential)	1.5 bar
Inner diameter	136 cm
Thickness (cylinder)	10 mm
Thickness (head)	4.0 cm
Mass	1200 kg

Table 3.1: NEXT-100 pressure vessel basic parameters and dimensions (some of these quantities could change slightly during the construction phase due to refinements in the design) [60].

vessel will be placed horizontally to reduce the maximum height, improving the distribution of weights. The total weight of the pressure vessel is 1200 kg. Table 3.1 shows its basic parameters and dimensions. The pressure vessel is built with an special stainless steel alloy, with a high composition in 316-Ti, which is a titanium stabilized version of 316 molybdenum-bearing austenitic stainless steel. The 316 alloys are more resistant to general corrosion, pitting and crevice than the conventional chromium-nickel austenitic stainless steels such as 304. In addition, 316-Ti alloy presents an activity at the level of 0.2 mBq/kg for the thorium series and 1.3 mBq/kg for the uranium series [60, 79], resulting in a total activity of about 1.6 Bq for the uranium series. To shield the internal volume from this activity, an inner radiopure copper shield of 12 cm thick is placed surrounding the internal face of the pressure vessel. This shielding, attenuates the radiation coming from the external detector.

3.5.2 Field Cage

The field cage of the NEXT-100 detector will consist in a cylindrical shell made of high-density polyethylene (HDPE) of 2.5 cm thick. The main functions of the field cage are, at the same time that provides electrical insulation from the pressure vessel, provides structural support to the different components needed to produce the drift field inside the TPC. In addition, it supports a set of reflector panels made of PTFE (Teflon) which improve the light collection efficiency of the detector. The reflectors panels are coated with a wavelength shifter (TPB), described in detail in § 4.3, which shifts the UV light emitted by xenon to blue ($\sim$ 430 nm).

The field cage is divided in three regions by three metallic wire meshes, cathode, gate and anode. The drift region, between cathode and gate, is a cylinder of 107 cm diameter and 130 cm length (see Table 3.2). The high voltage is degraded by copper strips attached to the HDPE and connected with low background resistors. The EL region, defined between gate an anode, is 0.5 cm long. In the opposite side of the field cage, a buffer region between the cathode and the energy plane will be used to degrade the high voltage in the cathode to ground, protecting the photosensors present in the energy plane. The meshes are made of stainless steel with 30 μm wire diameter and a 0.5 mm wire pitch, which results in an open area of 88%.

3.5.3 Gas System

The main goal of the gas system of the NEXT-100 detector is to maintain the xenon gas in optimum clean condition, in such a way that the levels of impurities are as low as possible. This will reduce the attachment of ionization electrons to the electronegative impurities (O_2, CO_2), thus increasing the electron lifetime and therefore the electron collection efficiency. In addition, the expensive ^{136}Xe used in the detector must be kept safely, reducing the leakage of the system to a minimum (it is

Parameter	Dimension
Drift field strength	0.3 kV cm^{-1}
El field strength (E/p)	3.0 kV cm^{-1} bar^{-1}
Optical gain	2500 photons/e^-
Drift Length	130 cm
Inner diameter	107 cm
EL gap	0.5 cm
Cathode voltage	-58 kV
Gate grid voltage	-22.5 kV
Anode grid voltage	0 V

Table 3.2: Basic parameters of the electric field regions (drift and EL) of NEXT-100 [60].

designed to be no more than 10 g of Xe per year). To ensure this, an operational protocol was established as follows:

- Vacuum evacuation of the vessel to as low pressure as possible. A reasonably good vacuum is in the range of 10^{-4} to 10^{-5} mbar. To achieve this, a turbo-molecular pump station will be directly connected as close as possible to the NEXT-100 vessel through a large conductance valve rated for vacuum and pressure. To improve the efficiency, the system will be evacuated from several points.

- Pressurize the vessel, from vacuum to 15 bar (absolute) with Argon. The objetive to do this is to clean the internal parts of the detector at the same time that the full system is checked for leaks. The system is then vacuum evacuated again.

- The pressure vessel is filled with the enriched xenon. A re-circulation compressor, with three stainless steel diaphragms,

is responsible for moving the gas through the system. Between each of the diaphragms there is a sniffer port to monitor for gas leakages. In the event of a leakage, automatic emergency shut-down is initiated.

- Finally, continuous gas re-circulation through the getter system will clean the gas. The gas system will contain two such getters in parallel with a bypass. The ability to bypass the getters will allow the testing of the purification of the gas and aid in diagnostic and monitoring of the gas system. While cold getter technology is capable of reaching the required purity levels in water and oxygen, a hot getter can also remove nitrogen and methane. In addition cold getters have shown to emanate Rn while hot getters are Rn free.

The nominal flow rate will be 100-300 standard liters per minute, well in excess of the required flow rates for NEXT-100, thus offering sufficient spare capacity. In addition, an automatic recovery system of the expensive ^{136}Xe will be needed to evacuate the chamber in case of an emergency condition. A 30 m^3 expansion tank will be placed inside the laboratory to quickly reduce the gas pressure in the system where an over-pressure, that can potentially cause an explosion, or an under-pressure, indicating a leak in the system, is detected.

3.5.4 **Energy Plane**

Measuring the energy of $\beta\beta0\nu$ events in NEXT-100 detector is a crucial task that must be carried out by sensitive and precise sensors that, at the same time, satisfy the required radiopurity conditions. For that reason, a set of photomultipliers (PMTs) will form the *energy plane* which will be located behind the transparent cathode. The *energy plane* will also record the scintillation light that indicates the start of the event (t_0).

Parameter	Value
Spectral response	160 to 650 nm
Wavelength of Maximum Response	420 nm
Photocathode size	3 inches
Supply voltage	1750 V
Quantum Efficiency at 175 nm	26 %
Gain	5.0×10^6
Dark current	10 nA
Radioactivity per PMT (uranium series)	3.3 mBq
Radioactivity per PMT (thorium series)	2.3 mBq

Table 3.3: Hamamatsu R11410-10 photomultiplier basic parameters [60].

The photomultipliers chosen for this task will be the Hamamatsu R11410-10. This model has been specially developed for radiopure, xenon-based detectors, having interesting properties which fit perfectly with the requirements of our detector (see Table 3.3).

A total number of 60 PMT will be needed to optimally cover the *energy plane*, 37% of the field cage cross-section [60]. However, the chosen model cannot withstand the pressure at which NEXT-100 plans to run (15 bar), having a maximum operational pressure of 6 atmospheres [80]. For that reason, they will be sealed into individual pressure resistant, vacuum tight copper enclosures coupled to sapphire windows. The window, 5 mm thick, is secured with a screw-down ring and sealed with an O-ring to the front-end of the enclosure. A similar back-cap of copper seals the back side of the enclosures. The PMT is optically coupled to the window using silicone optical pads of 2-3 mm thickness. A spring on the backside pushes the photomultiplier against the optical pads [60].

Each individual group, formed by a PMT plus its enclosure, will be mounted in a common carrier plate which is attached to the internal

face of the pressure vessel head. All enclosures are connected via pressure-resistant tubes coupled to a central manifold from where vacuum evacuation is produced. In the hypothetical case of a leak occurs in the system, the recovery system mentioned in § 3.5.3 becomes operational, quickly recovering xenon.

3.5.5 **Tracking Plane**

The topological reconstruction of the events and their rejection in the case are background events, will be carried out in NEXT-100 by a plane of Silicon PhotoMultipliers (SiPMs) operating as sensor pixels, located behind the transparent EL gap, which form the *tracking plane*. Two sensors are candidates to carry out this task, the Hamamatsu S10362-11-050P [81] model and the SensL MicroFC-10035-SMT-GP [82] model. The photosensors will be mounted in Dice Boards (see § 4.4) in groups of 64 elements sharing their common bias voltage, and then coated with a wavelength shifter (TPB) (see § 4.3). Both sensors have been chosen because of their high photon detection efficiency to the TPB wavelength re-emission ($\sim$ 430 nm), as well as their low dark count rate [60]. However, as their radiopurity levels play a crucial role, the final selection will be made once this measurement is done.

The pitch of the NEXT-100 *tracking plane* is a compromise between several constraints imposed by physics. In the one hand, the transversal charge diffusion in pure xenon at electric field strengths around 0.5 kV/cm is about 1 mm/$\sqrt{\text{cm}}$. Therefore a pitch smaller than 1 cm is not useful. On the other hand, as the pitch increases, the background rejection capabilities decrease due to the worse spatial resolution. Simulations show that a reasonable tradeoff may be found for a pitch of 1 cm. In NEXT-100, a total area of $\sim$0.92 m^2 must be covered, consequently around 7200 SiPMs spread over 112 Dice Boards will be used.

3.5.6 **Data Acquisition**

The NEXT-100 data-acquisition system is based on the Scalable Readout System (SRS) jointly developed with CERN-PH in the framework of the RD-51 collaboration [83]. At the top of the hierarchy, a PC farm running the DAQ software, DATE, receives event data from the DAQ modules via Gigabit Ethernet (GbE) links. The DATE PCs (Local Data Concentrators, LDCs) assemble incoming fragments into sub-events, which are sent to one or more additional PCs (Global Data Concentrators, GDC). The GDCs build complete events and store them to disk for offline analysis. A scheme of this structure is shown in Figure 3.8.

The DAQ modules used are Front-End Concentrator (FEC) cards, which serve as the generic interface between the DAQ system and application-specific front-end modules. The FEC module can interface different kinds of front-end electronics by using the appropriate plug-in card. Three different FEC plug-in cards are used in NEXT-100 (energy plane readout, trigger generation, and tracking plane readout) [60].

3.5.7 **Shielding**

The NEXT-100 detector will be placed at *Laboratorio Subterráneo de Canfranc* (LSC) [84], at Hall A. The facilites are carved into the rock at 850 meters deep below the Tobazo Mountain, on the Spanish side of the Pyrenees. The 2450 meter water equivalent depth, shield attenuate the cosmic radiation creating the cosmic silence needed for the experiment.

However, the ^{214}Bi isotope coming from the progeny of ^{222}Rn isotope present in air, must be taken into account and reduced. This is done by the inclusion in the laboratory of a Rn getter machine which will plane to reduce the amount of Rn in the air by a factor 10^3.

To shield NEXT-100 from the remanent external flux of high-energy gamma rays, a lead castle structure has been designed and built (see Figure 3.9). The lead wall has a thickness of 20 cm and is made of layers of staggered lead bricks held with a steel structure. The lead bricks

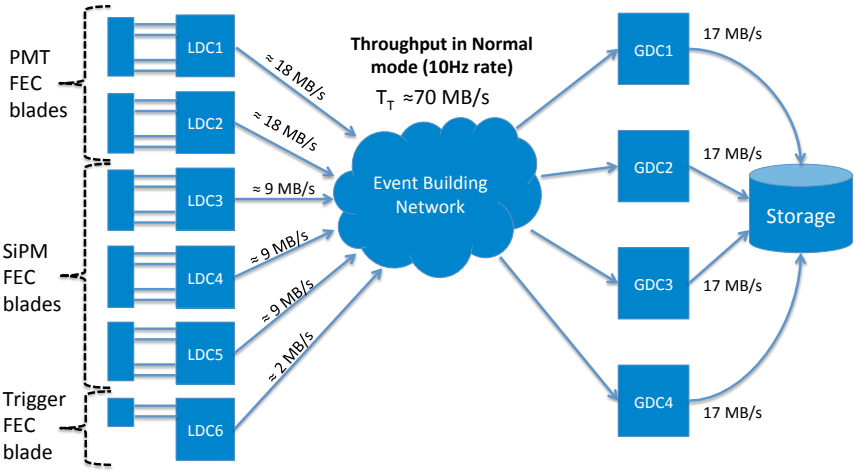

Figure 3.8: Scheme of DAQ and Online for NEXT-100.

have standard dimensions (200 x 100 x 50 mm^3), and by requirement, an activity in uranium and thorium lower than 0.4 mBq/kg.

The lead castle, with a total weight of 60 tons, is made of two halves mounted on a system of wheels that move on rails with the help of an electric engine. The movable castle has an open and a closed position. The former is used for the installation and service of the pressure vessel; the latter position is used in normal operation. A lock system fixes the castle to the floor in any of the two configurations to avoid accidental displacements. In addition, the lead castle, and the whole detector, are placed over an anti-seismic platform in order to reduce possible damage of the equipment in case of earthquake.

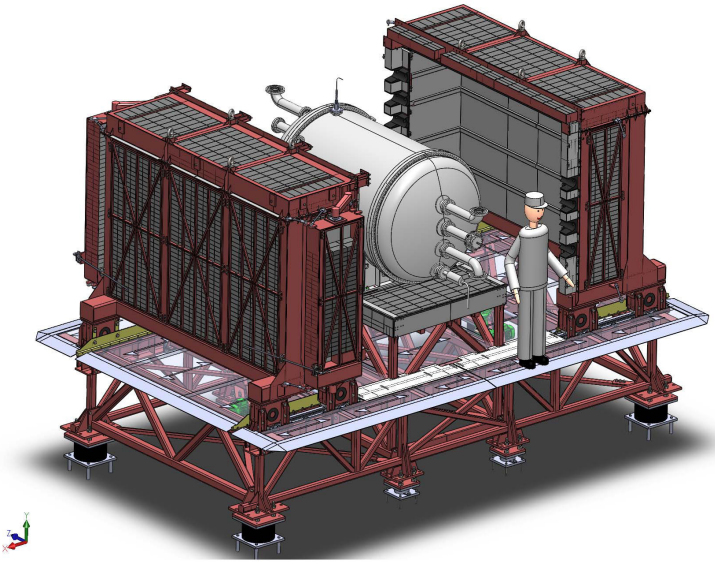

Figure 3.9: Drawing of the NEXT-100 detector and the lead castle shield (in open position). Both the detector and shield rest on an anti-seismic platform.

3.6 Projected Sensitivity

As explained above, the main backgrounds in NEXT are the high energy gammas emitted in the decays of ^{208}Tl and ^{214}Bi, present in all materials with which NEXT-100 is built. However, the appropriate selection of materials reduces the initial number of background events to levels of the order of few Bq [45], which is a extremely low rate considering the more than 12 tons of mass that constitute the detector [60], excluding the lead shielding. In addition, the technology used in NEXT allows the reduction of the number of background events which can be confused

Selection criteria	$\beta\beta0\nu$	^{208}Tl	^{214}Bi
Fiducial, single track $E > 2.3$ MeV	0.4759	2.83×10^{-5}	1.04×10^{-5}
Track with 2 blobs	0.6851	0.1141	0.105
Energy ROI	0.8661	0.150	0.457
Total	0.2824	4.9×10^{-7}	4.9×10^{-7}

Table 3.4: Acceptance of the selection criteria for $\beta\beta0\nu$-decay events described in the text. The values for ^{208}Tl and ^{214}Bi correspond to one of the dominant sources of background in the detector.

as a signal candidate. This property, known as rejection capability, is based on the assumption that only events fulfilling the following criteria will be accepted as $\beta\beta0\nu$ candidate:

1. The event consists of one single reconstructed track confined within the *fiducial volume* oh the detector — defined by excluding a region of 2 cm around the boundaries of the active volume — and with energy above 2.3 MeV.
2. The reconstructed track features the topology described in § 3.3, a *blob* at both ends.
3. The energy of the event is within the *region of interest* around $Q_{\beta\beta}$.

Using the previous criteria, the selection efficiency for background events as well as $\beta\beta0\nu$ events are shown in Table 3.4, producing a total rejection factor of the order of 10^{-7}. The achieved rejection factor produces a total background rate per unit of $\beta\beta$ isotope mass, energy and mass of

$$5.86 \times 10^{-4} \text{ counts}/(\text{kg} \times \text{keV} \times \text{year}).$$

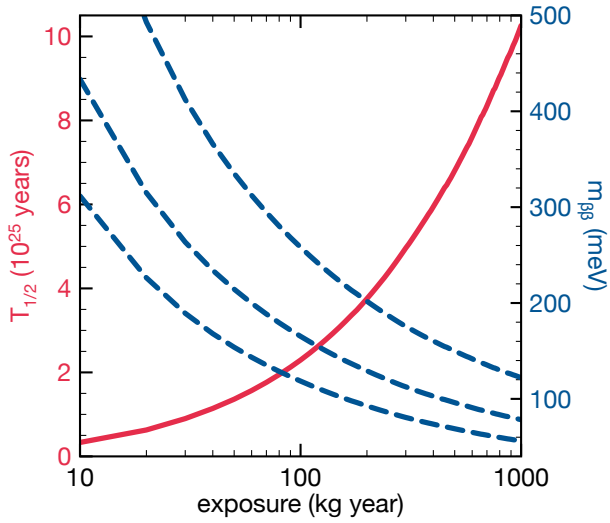

Figure 3.10: Sensitivity (at 90% CL) of NEXT-100 to neutrinoless double beta decay. The solid curve represents the half-life sensitivity, while the dashed curves correspond to the $m_{\beta\beta}$ sensitivity for three different NME calculations (from bottom to top: EDF [86], IBM-2 [85], ISM [87].

With this expected background rate and after 5 years of data taking, an experimental sensitivity of $T^{0\nu}_{1/2}(^{136}Xe) > 5.9\times 10^{25}$ years is predicted or, in terms of the effective neutrino Majorana mass $m_{\beta\beta}$, a value of around 100 meV, depending of the nuclear matrix element ($M^{\beta\beta 0\nu}$) model used to compute it. In Figure 3.10, $m_{\beta\beta}$ and $T^{0\nu}_{1/2}$ are represented for three different models of nuclear matrix elements, the interacting boson model (IBM-2) [85], the energy density functional method (EDF) [86] and the interacting shell model (ISM) [87].

With such sensitivity, NEXT-100 plans to be one of the leader experiments in the field, being able to explore the beginning of the region corresponding to the inverse hierarchy of neutrino masses.

3.7 The NEXT-DEMO prototype

To demonstrate that the detector concept described in the previous sections is feasible and reliable, a scaled-down prototype, NEXT-DEMO [88], was built. It is installed in a semi-clean room at *Instituto de Física Corpuscular de Valencia* (IFIC) (see Figure 3.11). This prototype was taking data during the last three years (2012-2014), leading some publications [4, 5, 88].

The goals of this detector are the following: demonstrate that the target energy resolution (1% FWHM at $Q_{\beta\beta}$) is realist in a large-scale detector at the same time that tracking reconstruction is feasible using a tracking plane performance. In addition, NEXT-DEMO has provided the necessary knowledge for working with large detectors, allowing to understand and establish a working protocol when operating high voltages and long drift lengths. Besides, it has also help to understand gas recirculation in a large volume, including operation stability and robustness against leaks. The detector is not radiopure and is not shielded against natural radioactivity.

NEXT-DEMO is a cylindrical pressure vessel made of stainless steel, able to withstand up to 20 bar of internal pressure. It is 60 cm long and 30 cm in diameter, and holds about 1.5 kg of Xe at 10 bar. Three wire grids, the cathode, gate and anode, limit the two active regions of the TPC, the 30 cm long drift region, between cathode and gate, and the 0.5 cm long EL region, between gate and anode (see Figure 3.12-*left*). The cathode is typically operated at -25 kV, while gate and anode are typically operated at -10 kV and 0 V respectively. These values produce an electric field in the drift region of around 500 V/cm, and an $\bar{E}/p$ of about 2.0 kV/bar cm. A set of six panels made of PTFE (Teflon) are mounted inside forming an hexagonal light tube, which is TPB coated to improve the light collection efficiency coming from xenon scintillation (see Figure 3.12-*right*).

Figure 3.11: The NEXT-DEMO detector and ancillary systems (gas system, front-end electronics and DAQ) at IFIC [5].

Natural xenon circulates in a closed gas system through the vessel and a system of purifying filters. The functions of the gas system of NEXT-DEMO are the evacuation of the detector, its pressurization and depressurization with xenon (and argon), and the recirculation and purification of the gas, that is, follows the same operational protocol described in § 3.5.3.

The energy plane of NEXT-DEMO is equipped with 19 Hamamatsu R7378A photomultiplier tubes. These are 1-inch, pressure-resistant (up to 20 bar) PMTs with a quantum efficiency of around 25% in the xenon scintillation emission. The PMTs are inserted into a PTFE holder following a hexagonal pattern. The total coverage area of the energy plane is about 39%. A grid, known as shield and similar to the cathode but with the wires spaced 0.5 cm apart, is screwed on top of the holder

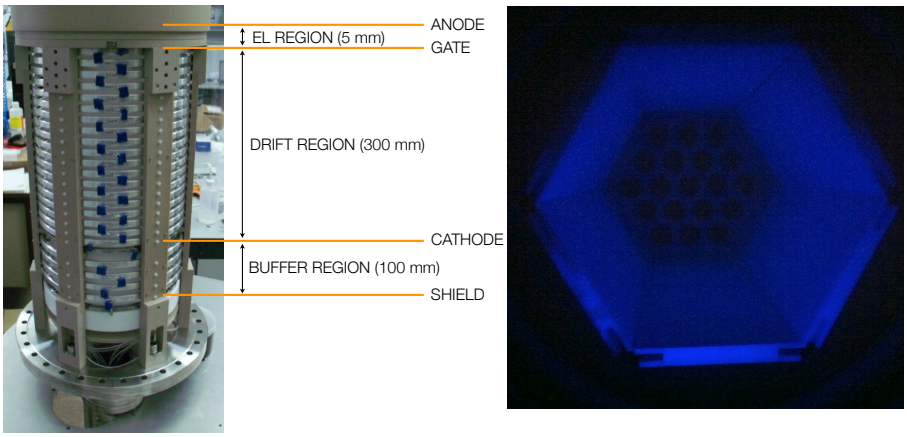

Figure 3.12: Left: External view of the time projection chamber approximately indicating the different regions. Right: Hexagonal light tube of NEXT-DEMO illuminated with a UV lamp after being coated with TPB [5].

and set to 500 V. This protects the PMTs from the high voltage set in the cathode, and ensures that the electric field in the 10 cm buffer region is below the EL threshold.

The tracking plane of NEXT-DEMO is formed by 256 Hamamatsu S10362-050-11P Silicon PhotoMultiplier (SiPMs). These are grouped in groups of 64 elements sharing their common bias voltage. This configuration is fully addressed in Chapter 4, describing the main characteristics of these sensors as well as the tests which were carried out for the understanding of their response, in order to ensure a proper operation once inside NEXT-DEMO.

Try not to become a man of success, but rather try to become a man of value.

Albert Einstein

CHAPTER

4

The NEXT-DEMO Tracking Plane

The tracking function in NEXT is provided by a plane of Silicon PhotoMultipliers located behind the EL gap. These photosensors are mounted on electronic boards called *Dice Boards* sharing the same bias voltage and coated with an appropriate wavelength shifter which emits at a wavelength at which the sensors have high detection efficiency. A candidate technology for the NEXT-100 detector is the S10362-11-050P [89], provided by Hamamatsu Photonics [81]. This model was selected to form the tracking plane of the NEXT-DEMO prototype.

This chapter describes the basic operating principle of silicon photomultiplier detectors as well as detailing the work performed to correctly characterize these sensors. Furthermore, the wavelength shifter coating protocol developed by the collaboration to ensure the homogeneous response of the tracking plane as well as its influence in the

sensor's response are presented. Finally, the installation procedure for NEXT-DEMO is described.

4.1 Introduction to Semiconductor Detectors

Silicon, as a semiconductor material, presents an electronic bands structure, illustrated in Figure 4.1-b. This structure consists of a *valence* band, a "forbidden" *energy gap* and a *conduction* band.

The energy bands are regions of many discrete levels which are so closely spaced that they may be considered a continuum, while the "forbidden" energy gap is a region in which there are no available energy levels at all. The highest energy band is the conduction band. Electrons in this region are detached from their parent atoms and are free to move around the material. The electrons in the valence band levels, however, are more tightly bound and remain associated to their respective lattice atoms.

In a semiconductor, the width of the energy gap is relatively small, around 1 eV [90], so only a few electrons can be thermally excited and jump into the conduction band. In insulators, Figure 4.1-a, the energy gap is larger, and their electrons are normally all in the valence band. In conductors (Figure 4.1-c), however, the gap is nonexistent and electrons are free to jump into the conduction band and, if an electric field is applied, a current is generated.

Silicon is a tetravalent atom, that is, it has four valence electrons to create four covalent bonds and stabilize the joint, forming an atomic crystal. In this configuration, if a valence electron is thermally excited, it moves into the conduction band leaving a hole in the valence band. This hole is rapidly filled by a neighboring valence electron, leaving a new hole which will be filled by another valence electron. The repetition of the process along the structure of the crystal results in the apparent movement of a positive charge (the hole), and thus a positive current is generated. In silicon, contrary to what happens with metals where

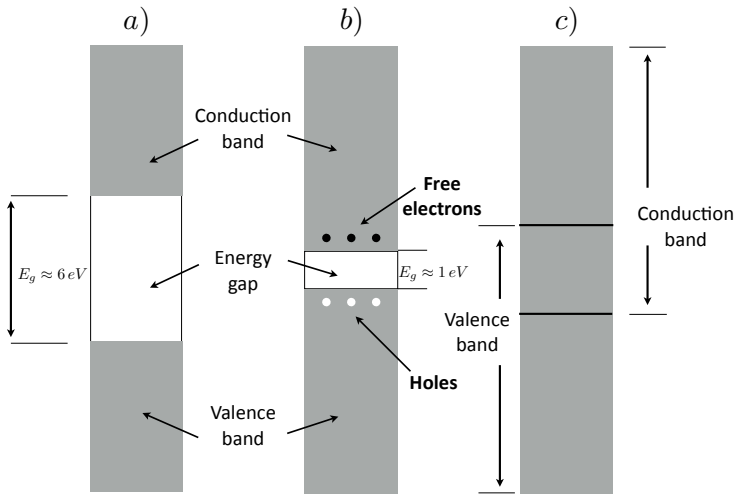

Figure 4.1: Scheme of the energy-band structure of (a) an insulator, (b) a semiconductor, and (c) a conductor.

the current is generated only by electrons in the conduction band, the electric current arises from two sources, the movement of the free electrons in the conduction band and the movement of the holes in the valence band.

If the silicon is "pure", the number of holes is equal to the number of electrons in the conduction band. However, a small amount of impurities can be added to the crystal, modifying its lattice. This process is called *doping*. If the dopant is pentavalent, which means that it has five electrons in the valence band, four covalent bonds will be formed leaving one free electron. This free electron will reside in a discrete energy level created in the energy gap by the presence of the

impurity atom, which will be extremely close to the conduction band being separated by only 0.05 eV [90]. In this configuration, electrons are the majority charge carriers and silicon is called *n-type* (Figure 4.2-left).

On the other hand, if the impurity is trivalent, it contains three electrons in the valence band and three covalent bonds will be formed, generating an excess of holes in the crystal. The trivalent impurities also perturb the band structure by creating a new state in the energy gap, but this time close to the valence band. In this case, holes become the majority charge carriers and silicon is called *p-type* (Figure 4.2-right).

The impurities typically used are arsenic or phosphorus to create *n-type*, and gallium or boron for *p-type*. The level of impurities present in the crystal is usually small compared to its density (10^{22} atoms/cm^3), typically of the order of 10^{13} atoms/cm^3 [90].

Silicon photomultiplier technology uses as its base the silicon diode. Such devices are made by diffusing *n-type* and *p-type* dopants into adjacent regions on a silicon substrate to create *pn-junctions*. Along the border between majority p-type and majority n-type regions the difference in electron and hole concentrations causes diffusion between the regions. As more electrons diffuse into the p-type region and holes move in the opposite direction an electric field $\vec{E}$ is created which opposes further movement. The region in which this field acts is called the *depletion region* and, generally, has a width of order 0.5 μm and a potential difference of $V_0 = 0.7$ V. This configuration is commonly represented with the bottom symbol in Figure 4.3.

If a bias voltage is applied to the *pn-junction* in such a configuration that the p-type is connected with the positive terminal and the n-type is connected with the negative terminal, free electrons present in the n-region are pushed by the electrons from the negative terminal to the *pn-junction*, at the same time that the positive terminal attracts the valence electrons in the p-region, or, in other words, holes are pushed toward the *pn-junction*. In any case, the *depletion zone* will be reduced according to the applied bias voltage and, if it is larger

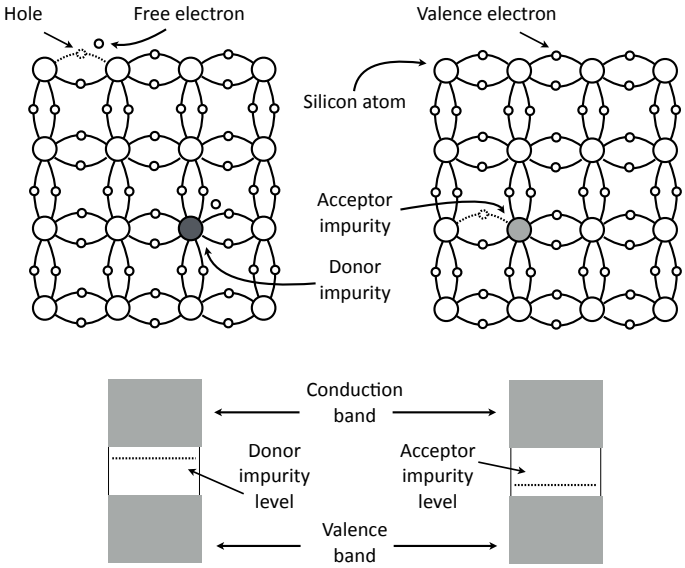

Figure 4.2: Covalent bonding of silicon. Left: Addition of pentavalent impurity (donor) forming n-type silicon. Right: Addition of tetravalent impurities (acceptor) forming p-type silicon.

than the potencial difference between the n-region and p-region V_0, a charge current is generated through the diode. This is the *forward bias* configuration.

On the other hand, if the bias voltage is applied in the *reverse bias* configuration, where the p-type region is connected to the negative terminal and the n-type region is connected to the positive terminal, the opposite effect occurs. Valence electrons present in the n-type region are attracted by the positive terminal at the same time as the negative terminal provides electrons to the holes present in the p-type region. This process is repeated until the *depletion zone* acquires the same

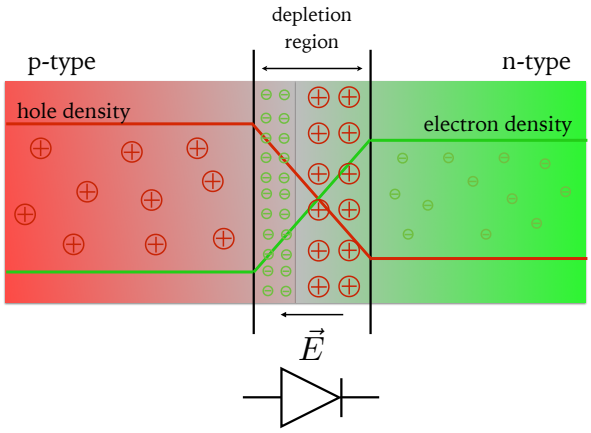

Figure 4.3: Scheme of the pn-junction model. Depletion zone and charge are only qualitative. Bottom symbol commonly used for a diode.

potential as the supplied as well as an electric field proportional to the one generated by the bias voltage. The net effect is an enlargement of the *depletion zone*, which is limited by the resistance of the semiconductor, until width values of around 1 mm. If the applied bias voltage keep rising the the *pn-junction* will breakdown and begin conducting.

Under these conditions, the *depletion zone* acquires the spatial property of being devoid of all mobile charged particle. The average energy for electron-hole pair creation in silicon at 25°C is 3.62 eV [90]. Ionizing radiation entering in this zone will create electron-hole pairs which will be swept out by the present electric field, and a current signal generated. The intensity of this signal depends of the bias voltage applied. If this voltage does not exceed a threshold, charges recombine, so no current signal will be generated. As bias voltage increases, the electric field causes that each original electron leads to an avalanche which is basically independent of all other avalanches formed from other electrons associated with the original ionizing event. The collec-

ted charge remains proportional to the number of original electrons. This is the proportional mode.

With a higher electric field, the *depletion zone* operates in Geiger mode, in which one avalanche can itself trigger a second avalanche at a different position. The difference between both modes is due to the holes: in Geiger mode they trigger avalanches, whereas in proportional mode, due to their ionization coefficient being much lower than that of electrons, they do not have enough energy to do so.

4.2 Silicon PhotoMultipliers

A Silicon PhotoMultiplier (SiPM) consists of a matrix of photodiodes, like the ones described in previous section, operating in Geiger mode. These photodiodes are connected in parallel with each one acting as a pixel of the SiPM. A detailed picture of this structure is shown in Figure 4.4. The pixels are connected using aluminium strips to read out the combined signals. The pixels are electrically decoupled by polysilicon resistive stripes between the pixels. These sensors are known by a huge range of names such a G-APD, SSPM, MRS APD, AMPD, or Multi Pixel Photon Counter (MPPC).

The MPPC used for the NEXT-DEMO detector is the model S10362-11-050P [89], provided by Hamamatsu Photonics [81]. This MPPC has many attractive features (see Table 4.1), such as low cost (about 20 to 50 euro per unit in large quantities), low operating voltage (usually smaller than 100 V), high gain, insensitivity to magnetic fields, and compact dimensions. Drawbacks arise from the high thermal noise rate (typically from 100 KHz up to a few MHz at the half photoelectron threshold) and the occurrence of after-pulses and cross-talk.

On the following sections, we describe the main features of the chosen MPPC as well as the test carried out to characterize their response.

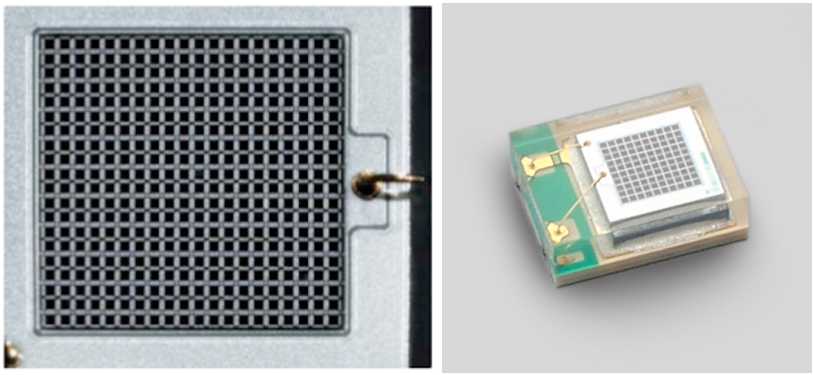

Figure 4.4: Left: Detail of the pixel array structure of a SiPM. Right: SiPM from Hamamatsu photonics.

Parameter	Value
Effective active area	1x1 mm
Number of Pixels	400
Pixel size	50x50 μm
Operating Temperature	0 to 40 °C
Fill factor	61.5 %
Spectral response range	320 to 900 nm
Peak Sensitivity wavelength	440 nm
Operating Voltage Range	70±10 V
Dark Count	400 kcps
Terminal Capacitance	35 pF
Time resolution (FHWM)	200 to 300 ps
Gain	$7.5 \cdot 10^5$

Table 4.1: Hamamatsu S10362-11-050P SiPM basic parameters [89].

4.2.1 Electrical Model

The simplest electrical model of a SiPM is shown in Figure 4.5. The depletion region introduces a capacitance to the pixel as it is basically a parallel-plate capacitor. The pixel can be regarded as a parallel circuit of a reverse biased diode and a capacitor with the pixel capacitance C_d. When the pixel is fired, the resulting avalanche makes the diode conducting so the capacitor is shorted and discharges.

The breakdown of the diode has to be quenched. Most of the time this is done passively with a quenching resistor. After the discharge of the pixel capacitance, the current starts flowing through the quenching resistor, which reduces the bias voltage V_{bias} at the diode below the breakdown voltage V_{bd}. This stops the breakdown and the diode blocks the current again. The quenching resistor is made of polysilicon and has a quenching resistance (R_q) of the order of few hundreds of kΩ. The quenching increases the pulse amplitude of the SiPM by introducing a spike component, since it is discharged during the breakdown of the pixel.

When a free electron is produced in one pixel, it initiates an avalanche of charge which produces a current. The sum of the currents from individual pixels is read out giving a signal proportional to the number of pixels fired.

4.2.2 Gain and Breakdown Voltage

The SiPM gain G, is defined as the charge produced in a single pixel avalanche, triggered either by thermal effects or the incidence of incoming photons, and is expressed in electron charge units.

In Geiger mode the charge generated by an avalanche fluctuates very little which allows the signal from the individual pixels of a SiPM to be added without need for correction.

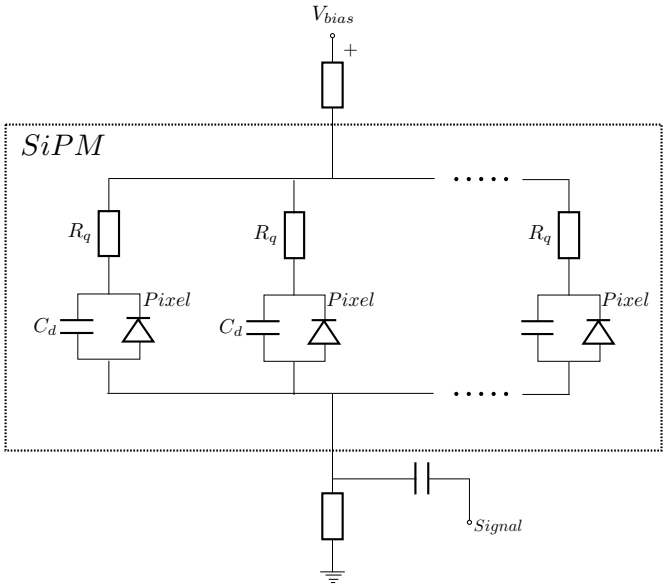

Figure 4.5: Schematics of the electrical model of the SiPM. The quenching resistance of the pixel is represented by R_q while the pixel capacitance by C_d.

The gains at their nominal bias voltage of several S10362-11-050C have been obtained using a basic bias circuit (Figure 4.6-*left*) containing a voltage feedback amplifier AD8055 [91] from Analog Devices, connected to a *Teledyne LeCroy WR-HRO 64ZI High Definition Oscilloscope* [92]. The SiPM is then illuminated with a low flux from a 400 nm LED. The output signal is integrated in a time window (~200 ns) containing 100% of the charge produced by the fired pixels (example in Figure 4.6-*right*). The resulting spectrum is known as the Single Photon Spectrum (*SPS*), depicted in Figure 4.7. As can be seen, a number of well-separated peaks are seen in the spectrum. These peaks represent

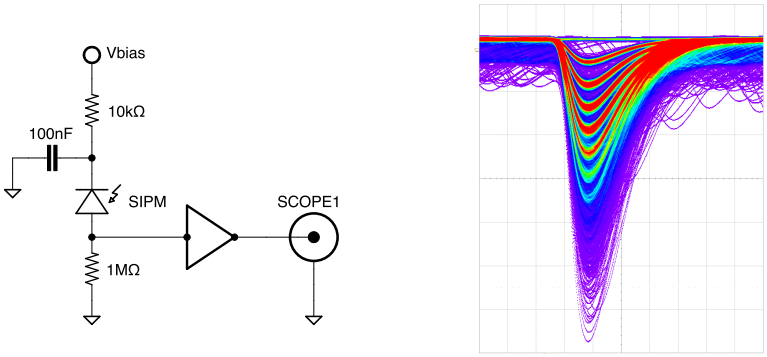

Figure 4.6: Left: Bias circuit connection example. Right: Pulse waveforms registered in the oscilloscope. The distributions produced by different number of fired pixels in the SiPM are clearly observable. The X axis has a scale of 50 ns/div while the the Y axis 5 mV/div.

the charge produced by integer numbers of photoelectrons. The rightmost peak in the spectrum is the integrated charge when there is no pixel fired, which corresponds to the electronic noise of the setup. The second peak from the right corresponds to that of one fired pixel. Later peaks correspond to multiple pixels firing at the same time. The gain of the SiPM is then obtained using the following relation:

$$G = \frac{\overline{\Delta V}}{F_{amp} \cdot q_{e^-}} \tag{4.1}$$

where $\overline{\Delta V}$ is given by the slope of the linear fit to the mean value of each peak plotted against the number of fired pixels (Figure 4.8), F_{amp} is the amplification factor of the amplifier and q_{e^-} is the electron charge. Using $\overline{\Delta V}$ obtained and equation 4.1, the gain of the SiPM used in this example is extracted as $G = (7.355 \pm 0.005) \times 10^5$, quite in agreement with the values suggested by Hamamatsu in Table 4.1.

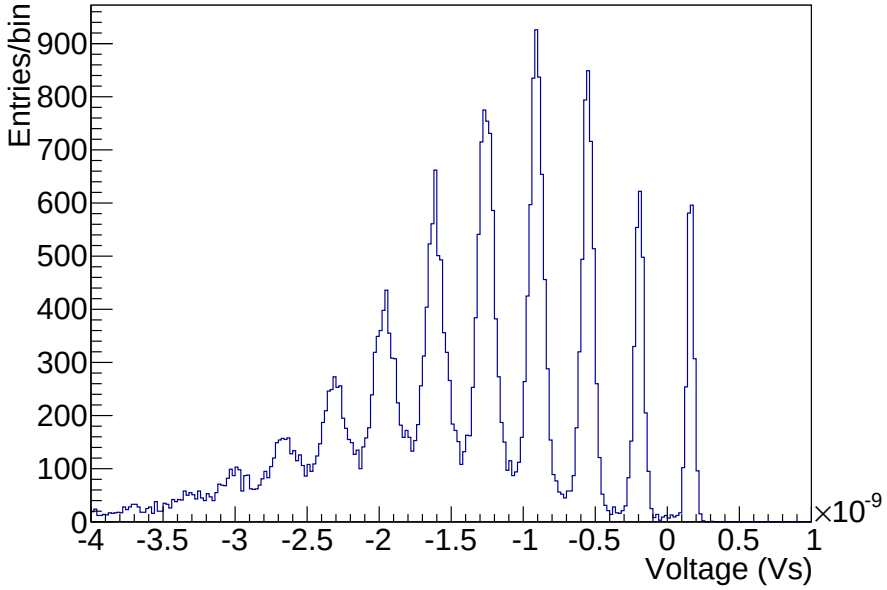

Figure 4.7: Typical single photon spectrum (SPS) of a SiPM obtained with a pulsed LED. Individual photoelectron peaks are identified. The peak on the extreme right corresponds to the charge of the electronics baseline. Subsequent peaks correspond to 1, 2, 3 ... pixels being fired in the SiPM.

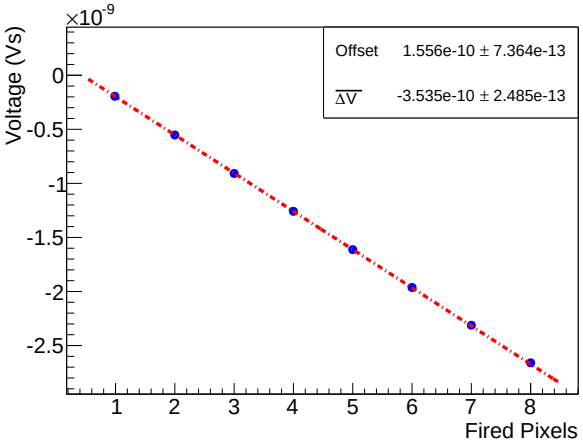

Figure 4.8: Mean charge produced by different number of fired pixels and linear fit to obtain the SiPM gain.

The fluctuation of the electronic noise is represented by the width of the rightmost peak (σ_0 from the gaussian fit) in Figure 4.7. It is independent of the SiPM and reflects the quality of the readout electronics chain. The width of the second and subsequent peaks (σ_N) increases due to two reasons: the statistical nature of the amount of charge produced by a fired pixel and the non-uniformity of the gain over the pixels. Using the propagation of uncertainty, σ_N^2 it follows that

$$\sigma_N^2 = N \cdot \sigma_G^2 + \sigma_0^2 \tag{4.2}$$

where $\sigma_G^2 = \sigma_1^2 - \sigma_0^2$, and $N = 1, 2, 3, \ldots$. Therefore, higher order peaks start to deviate due to their increased peak widths. Figure 4.9 shows σ^2 of each peak in the spectrum in Figure 4.7 plotted versus their corresponding number of pixels. A linear fit to the data points shows that for large number of pixels, the width increases faster than predicted. One possible explanation is the effect of signal afterpulses (see § 4.2.4).

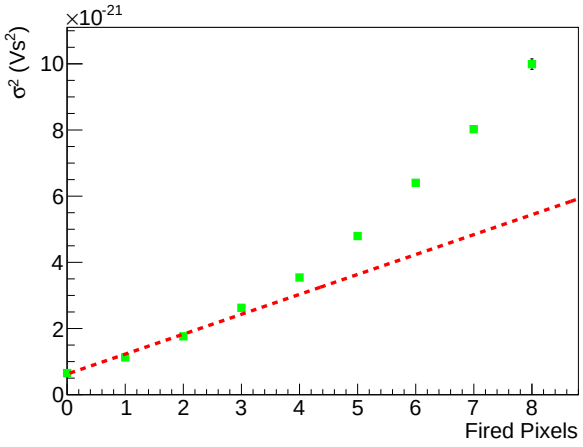

Figure 4.9: Sigma square of the charge distribution corresponding to the peaks in Figure 4.7 versus the number of fired pixels. The deviation from the linear trend is illustrated by the dashed line, corresponding to a linear fit to the first 3 data points.

Since an afterpulse can take place directly after a discharge, they can be integrated into the pulse. This further smears the separation between the peaks and produces an asymmetric tail on the right side of the pixel peak. When the peaks are fitted to a gaussian function, the resulting σ is therefore larger than the predicted value from equation 4.2.

On the other hand, the gain of a SiPM is directly proportional to the charge produced in an avalanche:

$$G = \frac{Q_{pixel}}{e^-} = C_d \cdot \frac{V_{bias} - V_{bd}}{e^-} = a \cdot V_{bias} + b \tag{4.3}$$

In the parallel plate capacitor model of the pixel, this can be seen to be directly proportional to the pixel capacitance and the difference of the bias voltage V_{bias} and the breakdown voltage V_{bd}. This difference is known as overvoltage V_{over}.

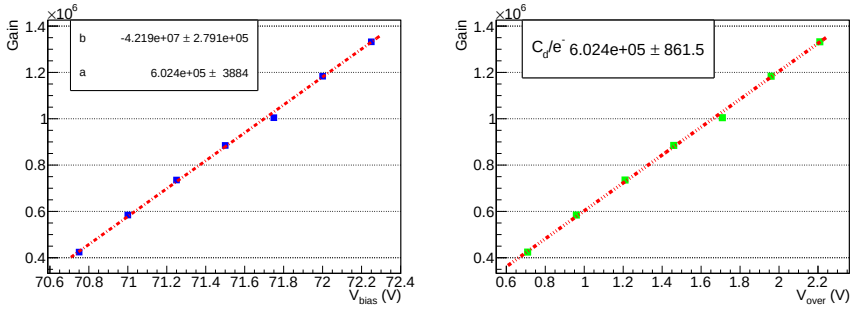

Figure 4.10: Gain versus operating voltage (left) and overvoltage (right) for a MPPC S10362-11-050P from Hamamatsu Photonics.

Figure 4.10 shows the gain of the SiPM as a function of the operative bias voltage at constant temperature. As will be commented in further sections, gain decreases proportionally with temperature; however, the temperature variation within the data taking was small enough ($\sim 0.5°C$) so that this effect is negligible. As can be seen, G increases as V_{bias} rises, due to the widening of the *depletion zone*. Fitting the data to the linear model shown in equation 4.3, the breakdown voltage and pixel capacitance of a SiPM can be determined. For the SiPM used in the plots these values are determined to be $V_{bd} = 70.04 \pm 0.01$ V and $C_d = 96.5 \pm 0.1$ fF respectively. The total capacitance (C_T) of the SiPM is defined as the sum of the capacitances of its pixels, as such, the example device has a capacitance of $C_T = 400 \times C_d = 38.60 \pm 0.05$ pF. This value is in agreement with the values suggested by Hamamatsu, shown in Table 4.1.

For the set of SiPMs used in this characterization, these parameters were distributed in a range of V_{bd} = [70.02 - 70.09] V and C_T = [36.7 - 38.92] pF.

4.2.3 Recovery Time

After the breakdown of the pixel is quenched, the bias voltage across the diode has to be recovered and the capacitance of the pixel recharged. This is done by taking charge from neighboring pixels and from the external electronics circuit. The behavior of the recovery is like that of an RC circuit following the function:

$$V_{bias}(t) = V_{bias}(t_0)(1 - e^{-t/\tau}) \tag{4.4}$$

where τ is the recovery time constant of the system. τ is proportional to the magnitude of the quenching resistance R_q and the pixel capacitance C_d:

$$\tau = R_q \cdot C_d \tag{4.5}$$

The quenching resistance of the individual pixel can be extracted from the data depicted in Figure 4.11, which shows the current across the SiPM versus voltage in the forward bias configuration. The current was measured with a Keithley 6517B electrometer [93]. As can been seen, current rises beyond $V = 0.7$ V, a value which corresponds to the potential difference between the n-region and p-region V_0 commented in § 4.1. Beyond this point, the intensity is linear versus the voltage supply as:

$$I = \frac{1}{R_{eq}} \cdot V \tag{4.6}$$

where R_{eq} means the equivalent resistor to all pixels connected in parallel:

$$\begin{aligned} \frac{1}{R_{eq}} &= \frac{1}{R_{q1}} + \frac{1}{R_{q2}} + ... + \frac{1}{R_{qN}} \\ R_{q1} &= R_{q2} = ... = R_{qN} \\ \frac{1}{R_{eq}} &= N \cdot \frac{1}{R_q} \end{aligned} \tag{4.7}$$

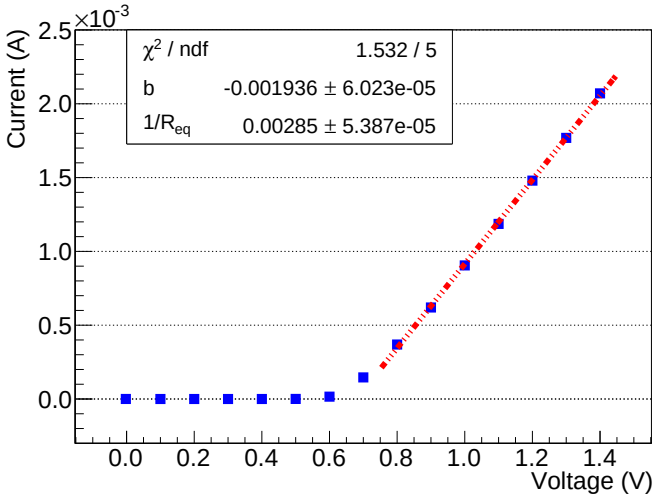

Figure 4.11: Forward Current for a SiPM S10362-11-050C and linear fit to equation 4.6 to obtain the quenching resistance of the pixel.

From equation 4.7 and the slope of the linear fit of Figure 4.11, the quenching resistor value obtained is $R_q = 140 \pm 2$ kΩ. The measured values for the set of sensors under test fell in the range 138 – 148 kΩ. Using this parameter and C_d, calculated in § 4.2.2, the recovery time constant is $\tau = 13.54$ ns.

The pixel capacitance is small if compared with the total capacitance of the SiPM. For that reason, at low intensities the drop in voltage induced by one pixel on the neighbors is small. However, at higher intensities, more pixels are fired and the potential of the remaining pixels is not always sufficient to recharge them. When this is the case, the charge is supplied by the external circuit which introduces a higher recovery time constant.

4.2.4 Afterpulsing

Impurities introduced in the lattice at the time of doping can produce regions with different band structures, traps, where avalanche electrons can be held and released after a characteristic time. If this characteristic time is longer than the recovery time τ mentioned in § 4.2.3, the released electron will produce a new avalanche within the pixel. This process is called *afterpulsing* and its probability can be expressed as

$$P_{af} = \frac{P_t}{\tau_t} \cdot e^{-t/\tau_t} \tag{4.8}$$

where P_t is the probability of electron capture by a trap, which depends on the density of impurities in the silicon, and τ_t is the trap lifetime, which varies with the temperature of the silicon lattice [90].

In the case that the electron is released before the bias voltage is completely restored, which occurs typically after 3 times τ, the new avalanche will contain less charge than the pixel capacitance C_d, and will also reduce the photon counting capability of the SiPM since this charge introduces an additional background to the response spectrum. This corresponds to the continuous contribution of the SPS in Figure 4.7.

4.2.5 Dark Count Rate

In some cases, the signal generated by a SiPM does not correspond with an incident photon or afterpulsing effects. In these cases, the signal is produced by free charge carriers, mainly due to thermal generation or tunneling effect, which triggers the Geiger discharge spontaneously, generating an identical avalanche. Such events occur even when the SiPM is operated in the dark; for that reason this effect is known as dark current or dark counts. The dark count rate (DCR) is a limiting factor for low intensity photon detection, as they can be confused with the arrival of real photons.

At higher temperatures ($T > 25°C$), the major contribution to dark count rate is the thermal generation of free charge carriers in the *depletion zone*. Direct transition of an electron from the valence to conduction band is very rare due to the width of the band gap in silicon. The presence of trap levels in the band gap introduced by crystal impurities facilitates the thermal generation. This process is described by the Shockley-Read-Hall model [94], and its contribution to DCR is given by

$$DCR \propto N_t \cdot W_D \cdot \sigma_n \cdot T^2 \cdot \exp(-\frac{E_a}{k_B \cdot T}) \tag{4.9}$$

where N_t is the intrinsic carrier density, W_D is the width of the *depletion region*, σ_n is the cross section for the process, T is the temperature, k_B is the *Boltzmant constant* and E_a is the activation energy which is the energy difference between the conduction band and the trap level. As can be seen in equation 4.9, the DCR has an exponential dependence with temperature, thus being the dominant factor in the generation of dark count events.

On the other hand, at lower temperatures it is the tunneling effect which becomes dominant in the DCR because thermal generation of charge carriers is highly suppressed. The probability for an electron to penetrate the band gap is proportional to the bias voltage. The tunneling effect becomes significant for induced electric fields above 10^6 V/cm increasing nonlinearly with field. At some point, overvoltage is such that afterpulsing becomes significant, and the output signal measured is a combination of both effects.

The Dark Count Rate of the SiPM used in NEXT-DEMO was measured using a similar setup to that employed in § 4.2.2, but this time without source of light. Therefore, the registered events correspond only to dark count events. Different voltage thresholds have been set over the registered values, obtaining the distribution depicted in Figure 4.12. As can been observed, DCR decreases for precise thresholds,

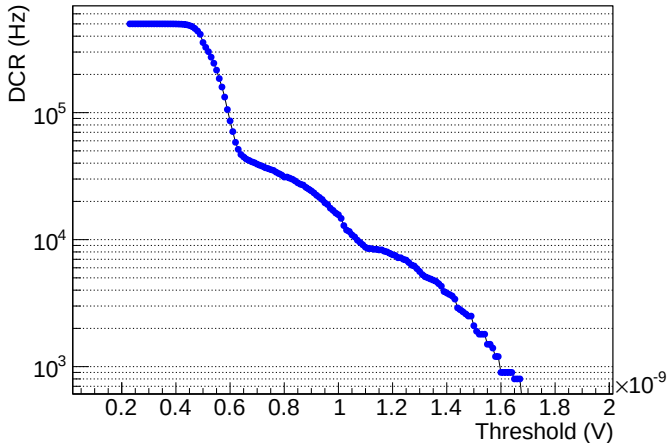

Figure 4.12: Dark Count Rate of the S10362-11-050C versus the voltage threshold established.

corresponding to the voltage produced by one pixel fired, two and so on.

Figure 4.13 shows the DCR at different overvoltage and temperature conditions, which are found to be compatible to the ones provided by Hamamatsu (see Table 4.1), following equation 4.9. Since the DCR is a limiting factor at low light intensities and has a dependency both on Temperature and Overvoltage, these parameters must be closely monitored and controlled during data taking.

4.2.6 Optical Crosstalk

During the breakdown of one pixel, every electron of the avalanche emits approximately 3×10^{-5} optical photons at wavelengths less than 1000 nm [95]. Considering the gains calculated in § 4.2.2 ($G \sim 10^6$), around 20 photons are generated per fired pixel. These photons can

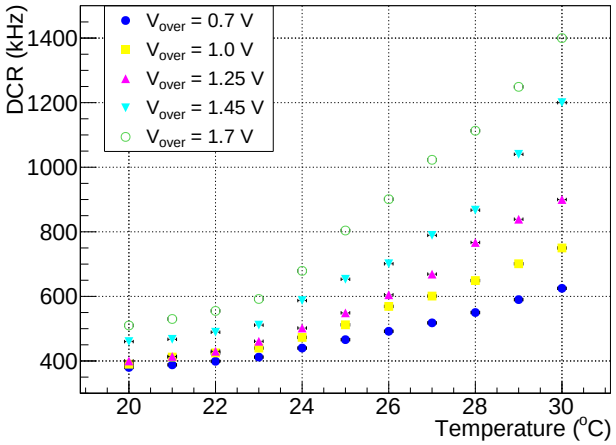

Figure 4.13: Dark Count Rate of the S10362-11-050C versus temperature at different overvoltages.

easily reach neighboring pixels, triggering new avalanches which are unrelated to the original one. If this occurs, both signals are integrated as a whole, limiting the photon counting capability of the SiPM, and making it impossible to determine the exact number of photons. This effect is know as *optical crosstalk*, and for the selected SiPM has a probability of occurrence of about 30-40% [96], increasing exponentially with overvoltage due to the number of electrons during breakdown increasing. This effect can be easily reduced by the introduction of opaque tranches between the pixels of the SiPM, which block the arrival of these photons to the neighboring pixels, reducing significantly the optical crosstalk to values around 5% for the overvoltage values where these sensors will be operated [97].

4.2.7 Photon Detection Efficiency

The Photon Detection Efficiency (PDE) is defined as the probability that an arriving photon which hits the SiPM surface triggers an avalanche and produces a measurable electrical charge. The PDE is defined as the product of three terms

$$PDE = FF \cdot QE \cdot P_{av} \tag{4.10}$$

where FF is the fill factor of the pixel, QE is the quantum efficiency for photoelectron conversion and P_{av} is the probability that electrons and holes initiate an avalanche in the depleted region.

The first term in equation 4.10 represents the ratio between the photon sensitive area over the total area of one pixel. As seen in Figure 4.14, some of the surface area is taken up by components not sensitive to light like quenching resistors and bias lines. In the case of the SiPM chosen for NEXT, due to the microcell structure of the sensor, the fill factor is ∼60% (see Table 4.1), while typical fill factor values oscillate between 20% up to 70%.

The quantum efficiency is defined as the probability that a photon incident on the sensitive area will produce an electron-hole pair. This effect has a spectral dependence, depending on the absorption coefficient of light in silicon (Figure 4.15). The photon absorption length in silicon varies from 10 nm to a few microns for wavelengths between 300 nm and 700 nm and is less than 10 nm for shorter wavelengths [98]. When the photon attenuation length is below the micron, a silicon-based photodetector can achieve high sensitivity only if the photo-detection region is close to the surface.

At the same time, the protective material which covers the silicon active area of the photosensors can additionally reduce their sensitivity to short wavelengths. The protective window of the standard SiPMs from Hamamatsu are made out of Epoxy-resin. This is a polymer that provides thin layer coatings of high mechanical strength and good

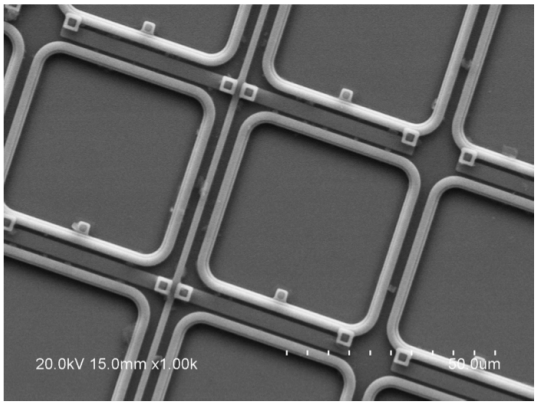

Figure 4.14: Micro-cells of a SiPM observed with a scanning electron microscope. Photon sensitive areas are delimited by a non sensitive structure.

adhesion to the silicon substrate of the SiPMs. It is however poorly transparent to photons below 300 nm, reducing drastically the PDE of the SiPMs below these wavelengths.

Finally, only photons which fall in the sensitive area of the pixel and have produced an electron-hole pair have a probability to trigger an avalanche. This probability is represented by P_{av} which reduces the PDE of the SiPM. Only in the case that electrons drift through the multiplication region will produce the avalanche breakdown. Those generated outside the depletion region will quickly recombine.

There are other factors, such as the dead time of the microcells, which can limit the PDE, however, they have little effect at the low light levels considered in this thesis.

The experimental determination of the PDE of the S10362-11-050P is discussed in [100]. The method is based on the comparison between the number of incident photons (N_{inc}) with the number of photons recorded (N_{rec}), equivalent to the number of SiPM cells fired. The

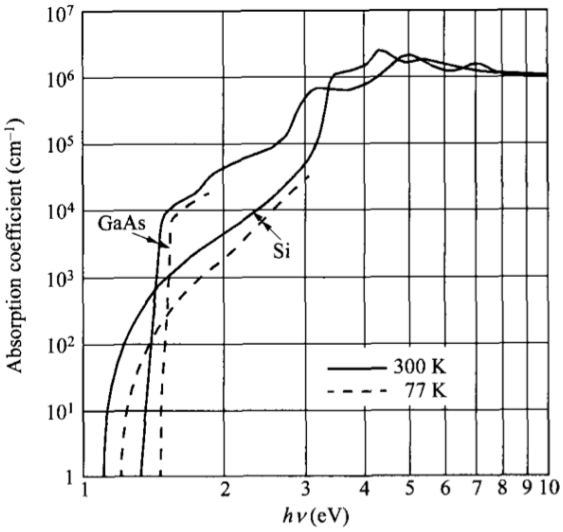

Figure 4.15: Measured absorption coefficients for Silicon and Gallium Arsenide, extracted from [99].

relation between both magnitudes follows the relation

$$N_{rec} = N_{pixels} \cdot (1 - exp(-\frac{N_{inc} \cdot PDE}{N_{pixels}})) \tag{4.11}$$

where N_{pixels} is the total number of pixels in the SiPM. At low illumination levels, where the number of incident photons is small compared to the number of the SiPM pixels ($N_{inc} << N_{pixels}$), the response of the photosensor is linear and equation 4.11 can be approximated to

$$N_{rec} = PDE \cdot N_{inc} \tag{4.12}$$

The number of incident photons in the SiPM is determined using a Hamamatsu PMT R8520-0SEL [81] calibrated by the manufacturer, operated without gain and normalizing its response by the ratio between

their photosensitive areas, while the number of recorded photons in the SiPM is determined from its output current (I_{SiPM}, after dark current subtraction) and the gain G provided by the manufacturer for a specific voltage at room temperature

$$N_{rec} = \frac{I_{SiPM}}{G \cdot q_{e^-}} \tag{4.13}$$

where q_{e^-} is the electron charge.

The results are shown in Figure 4.16-*left* as a function of wavelength in the spectral range 250-315 nm. As can be seen, this sensor has a poor PDE (of ∼2%) at these wavelengths, mainly due to the presence of the Epoxy-resin window which protects the silicon active area. This effect exposes the necessity of the introduction of a wavelength shifter which convert the xenon scintillation light generated in the detector into the wavelengths where the SiPM is more sensitive. This process is fully described in § 4.3.

For completeness, the PDE of a slightly different SiPM (S10362-33-050P), measured with the method described previously in the spectral range 250-550 nm, and their comparison with the values provided by Hamamatsu are depicted in Figure 4.16-*right*. The agreement between the independents measurements ensure the reliability of the method. At the time these results were produced, it was not possible to use the SiPM model S10362-11-050P to determine its PDE in the same spectral range. However, due to the similar properties of both sensors, values should be compatible with the ones measured.

4.2.8 **Dynamic Range**

If an avalanche has already been triggered in a pixel it is not possible for another photon to trigger another before the pixel has recharged. For that reason, the response of SiPM to a light flux is only linear at low intensities. At higher intensities, the number of incident photons

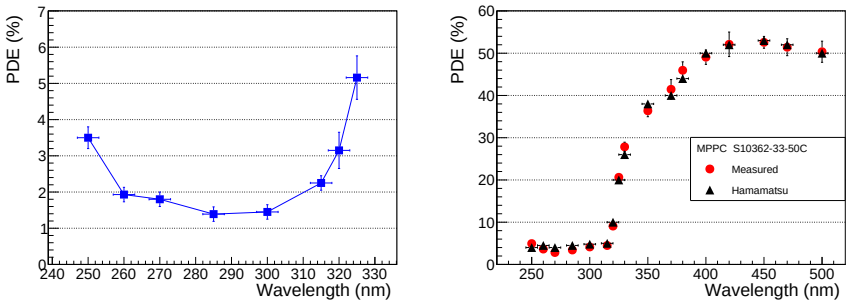

Figure 4.16: Left: Measured PDE of S10362-11-050P as a function of wavelength in the spectral range 250-315 nm extracted from [100]. Right: Measured PDE (red circles) and PDE values provided by Hamamatsu (black triangles) of S10362-33-050P as a function of wavelength in the spectral range 250-550 nm.

per single pixel as unit of area increases, not contributing to the total output signal generated. This behavior is described in equation 4.11, where the exponential term represents the number of detected photons per pixel. The dynamic range of the SiPM is then dominated by the number of available pixels in the detector, their recovery time and its PDE at the wavelength of the incident photons.

The response curve at different low illumination levels of the S10362-11-050P SiPM is shown in Figure 4.17. A 285 nm LED operated in continuous mode was used to illuminate the sensor. The intensity was tuned by controlling the current across the LED with a precise source-meter. The number of incident photons was measured by the calibrated PMT used in § 4.2.7 located closely above the SiPM. The effective PDE at this wavelength was $(1.46 \pm 0.01)\%$, as extracted from Figure 4.16-*left*. As can be observed, the response starts to deviate from linearity when about 10% of the total number of pixels are simultaneously excited and produce a photoelectron ($N_{rec} > 40$). This effect, which at first may seem

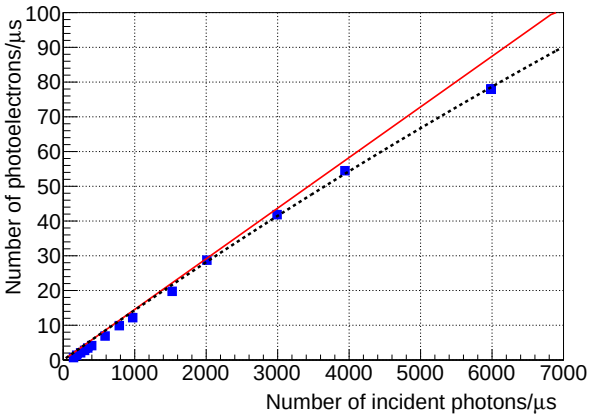

Figure 4.17: Response curve at 285 nm of S10362-11-050P extracted from [100]. The solid red line represents the linear fit to the data at low illumination levels. The dashed black line represents the theoretical response curve following equation 4.11.

to constrain the capability of the chosen sensors, will be also improved by the introduction of the wavelength shifter described in § 4.3, which will adapt even more the expected signal in NEXT to the dynamic range of the S10362-11-050P SiPM.

4.2.9 Suitability for NEXT

The tracking function in the NEXT experiment is based in the detection of the EL light generated by the ionization electrons produced by the beta particles in the high pressure gas. The number of photons produced per ionization electron was described in § 3.1. Using equation 3.9 and the operational parameters of NEXT-DEMO, with E/p = 2.0 kV cm^{-1} bar^{-1}, p = 10 bar and Δx = 0.5 cm, the optical gain yields in η = 820 photons per ionization electron.

The number of ionization electrons produced by a $\beta\beta$ event has an expected ratio of about 300 electrons/μs entering in the EL region and producing around $2.5{\times}10^5$ photons/μs. Assuming this light is emitted isotropically, with an optical transparency of the EL meshes of 88% (see § 3.5.2), an estimation of the number of photons expected to illuminate the 1 mm^2 active are of a SiPM is $N_{inc} \sim 120$ photons/μs. The time-stamp of the *tracking-plane* electronics, which will be discussed in § 4.5, will be 1 μs, so the dynamic range of its sensors should be adequate for the expected signal intensity.

The SiPM S10362-11-050P meets the above requirement, and with its 400 pixels and a recovery time of a few tens of ns, a linear response is expected during operation. Its robustness, high gain and photon counting capability, make it the appropriate candidate to discriminate between the different intensities in the generated signal. At the same time, as will be described in § 4.6, its dark count rate can be exploited during the calibration of the sensors. On the other hand, its main drawback arises from the low PDE at the scintillation light of xenon, which can be easily improved with the addition of the wavelength shifter already commented, and fully described in § 4.3.

4.3 SiPM Coating with a WLS

As commented in previous sections, the model of SiPM S10362-11-050P has been chosen for NEXT-DEMO thanks to its many outstanding features such as photon counting capability, dynamic range, robustness and low cost. However, its main drawback is the poor sensitivity in the emission range of the xenon scintillation light (peak at 172 nm). This makes necessary the use of a wavelength shifter (WLS) to convert the UV light into visible light, where these sensors have their optimal photon detection efficiency. This is done by covering the protective layer of the SiPM with an organic molecule, 1,1,4,4-Tetraphenyl-1,3-butadiene of > 99% purity grade [101]. This is achieved using direct application via vacuum evaporation onto the surface.

Tetraphenyl butadiene (TPB) is an organic compound which fluoresces when excited by UV radiation. Its fluorescence spectrum peaks at about 430 nm [102, 103], matching the PDE spectrum of the chosen SiPM (see Table 4.1), and does not vary with the wavelength of the incident light in the UV range [103].

4.3.1 Coating Protocol

The addition of TPB over the SiPMs to improve their PDE must be done in such a way that ensures the response uniformity of the sensor, hence, high quality coatings are needed. This section describes the coating technique which has been developed to ensure the conditions that guarantee uniformity, reproducibility and long-term stability of the TPB coatings on SiPMs [7].

The coating process was carried out in the facilities of the Instituto de Ciencia Molecular (ICMOL) of Valencia. This facility is located in a class 10000 clean-room due to the stringent cleanliness conditions that are required for high quality depositions of molecules on different substrates.

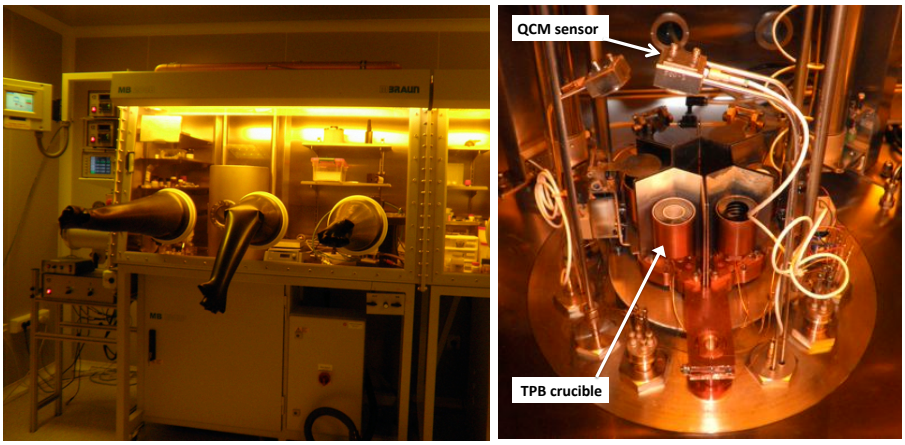

Figure 4.18: Left: Picture of the glove-chamber filled with N_2 . Right: Picture of the evaporation system containing the crucible used for TPB and the QCM sensor positioned on top of it.

The coating setup consists of a vacuum chamber or evaporator enclosing four ceramic crucibles which may melt simultaneously up to four different compounds (Figure 4.18-*right*). The vacuum system is composed of a diaphragm pump and a turbo-molecular pump that provide vacuum levels close to 10^{-7} mbar in the evaporator. The latter is enclosed in a glove-chamber filled with N_2, where the manipulation of different compounds takes place in an oxygen and water-free environment to prevent oxidation and hydration (Figure 4.18-*left*).

Only one crucible was filled with TPB powder, and then heated by a cartridge with an adjustable current that allows monitoring of the temperature and control of the evaporation rate, essential to prevent bubbling and sputtering of the TPB on the substrate. SiPMs were positioned on a sample-holder fixed on a spinning disk located 15 cm above the crucible. A shutter located under the holder allowed masking of the exposed surface when required. After positioning the SiPMs,

the vacuum-chamber was closed and evacuation was started. When the optimal vacuum level is reached, typically $4{\times}10^{-7}$ mbar, heating of the crucible was started with the shutter closed. The TPB melting temperature is 203°C at atmospheric pressure. At the high vacuum level reached in the evaporator, TPB evaporates at about 75°C.

The TPB deposition rate and thickness were measured with high precision with a Quartz Crystal Microbalance (QCM) from Sigma Instruments [104], located half way between the crucible and the SiPMs. This is a very sensitive mass deposition sensor based on the piezoelectric properties of the quartz crystal. The QCM is able to measure in real time mass changes ranging from micrograms to fractions of nanogram (that is a fraction of a monolayer of atoms) on the surface of the quartz crystal. The calibration of this sensor is thus necessary to determine accurately the deposition rate and thickness on the substrate. During the TPB coating campaign this calibration was performed using a high resolution surface profilometer (XP-1 from Ambios Technology [105]). The profile of a TPB deposition on a glass substrate, scratched with a cutter, was recorded by the profilometer. This allowed the measurement of the thickness of the TPB deposition in the Å range. This thickness measurement, compared to that recorded by the QCM sensor in the evaporator, provided the calibration factor for the rate and superficial mass deposition of TPB on the substrates.

The relevant coating parameters, the deposition rate and thickness, the temperature in the crucible and the vacuum level are displayed in the deposition control units. This allowed a constant monitoring of the evaporation process. When the deposition rate stabilized around a constant value, typically between 1.8 and 2.4 Å/s, a steady evaporation process of the TPB was established. The shutter was then opened and the spinning of the sample-holder was initiated to ensure a uniform TPB deposition on the SiPMs. When the desired thickness was reached, the shutter was closed, evacuation was stopped and the evaporator

Sample	Thickness (kÅ)	Density (mg/cm^2)
1	0.571	0.05
2	1.340	0.1
3	2.273	0.2
4	6.802	0.6

Table 4.2: Thicknesses and densities of TPB depositions samples.

was opened. The coated samples were stored in N_2 atmosphere or in vacuum to avoid their exposure to degrading agents.

Under these conditions, different substrates were used for calibration and characterization of the method, obtaining a range of coating thicknesses (0.6, 0.2, 0.1 and 0.05 mg/cm^2) (see Table 4.2). These samples were glass plates of 30x30 mm^2 coated with TiO_2 and a set of SiPM boards consisting of 5 SiPMs soldered onto Printed Circuit Boards.

4.3.2 Characterization of Coatings

Measurement of the emission spectrum of the TPB was carried out using a glass plate of 30×30 mm^2, coated with 0.1 mg/cm^2 of TPB (sample 2 in Table 4.2), placed in a small black box. A xenon lamp (Hamamatsu Photonics E7536, 150 W) coupled to a monochromator was used for the selection of the input wavelength. The spectrum after reflections was measured using a spectrometer (Hamamatsu Photonics Multichannel Analyzer C10027) allowed to record the spectrogram of the output light from the TPB layer. The light from the monochromator to the black box was conducted through a quartz optical fiber, coupled to the box through an optical feedthrough. The spot of the input light covered an area of a few mm^2 of the glass surface. The output light from the coated glass was collected by a lens, in the direction perpendicular to

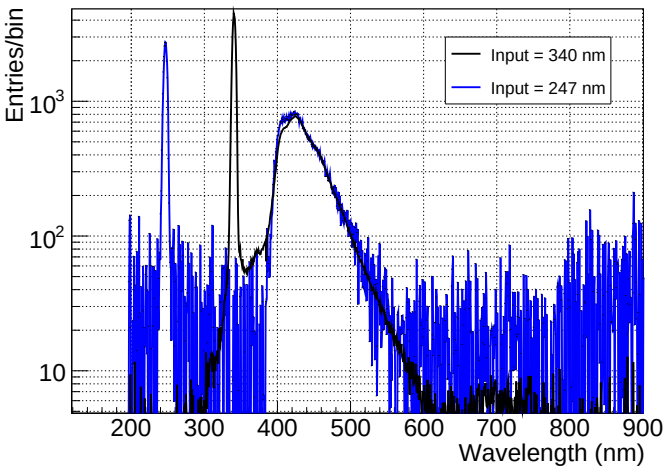

Figure 4.19: TPB emission spectra obtained from glass plate coated with 0.1 mg/cm^2 of TPB illuminated with 246 nm and 340 nm photons.

the input beam and conducted to the spectrometer by a quartz optical fiber.

Figure 4.19 shows the measured emission spectra of the TPB at the input wavelengths of 245 ± 2.5 nm and 340 ± 2.5 nm. The peaks corresponding to non converted input light are seen, well separated from the fluorescence peak lying at 427 ± 20 nm. This fluorescence peak shows no dependence on the input wavelength in the UV range below 340 nm. It presents, moreover, a long tail at longer wavelengths which originates from the radiative decays of the S1 excited state to the multiple vibrational levels of the ground state [7]. The maximum peak sensitivity of the chosen SiPMs is 430 nm (see Table 4.1), therefore, a TPB coated SiPM ensures maximum detection for the xenon scintillation light produced.

One of the problems when working with thin TPB depositions is

its fluorescence yield depends on the thickness of the deposition [102]. For that reason, the deposition homogeneity must be characterized to ensure the homogenous response of the sensors. The method, fully described in [106], is based on the response of a non-coated SiPM placed on one side of a coated glass plate. On the other side, a 260 nm LED was used to illuminate different coated sectors of the plate, as the glass plate was rotated. The mean current in the SiPM for each light exposition was measured using a picoammeter (Keithley 6487) and the current relative standard deviation $\sigma(I)/I_{mean}$ was drawn for each TPB coating of Table 4.2. This standard deviation is represented in Figure 4.20 as a function of thickness. The trend shown is compatible with that observed for the fluorescence yield as a function of thickness in [102]. The relative standard deviation of the measured current was close to 10% at the lowest thickness (0.05 mg/cm^2) and is slightly above 4% for the thickest coating (0.6 mg/cm^2).

The UV light converted by the TPB is emitted isotropically, so photons which reach the sensitive area of the SiPMs must pass through the layer of TPB. The transmittance of the TPB as a function of its thickness has been measured to evaluate the part of light which will be reabsorbed. Four glass plates of 30×30 mm^2 of Table 4.2 were placed between a 430 nm LED and a 1 inch PMT Hamamatsu R8520-406, and its current measured with a picoammeter. A non-coated glass plate with the same dimensions of the coated plates was used as a reference. The current in the PMT, induced by the light transmitted through the TPB layer, was compared to the current measured in the absence of TPB, using the reference glass and the same illumination conditions. The transmittance of the reference glass at 430 nm was also measured using the same LED and PMT was estimated to be 95.0 ± 0.1 %.

The transmittance of the TPB at its fluorescence wavelength (430 nm) is shown in Figure 4.21 as a function of the thickness. The trend observed indicates an increase of the absorption with the TPB thickness. However, this amount of light absorbed, remains below 4% which is

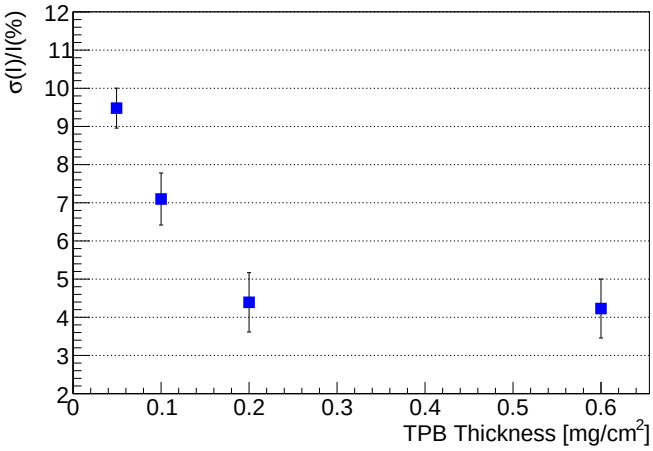

Figure 4.20: Relative standard deviation of current in a SiPM detecting light from different sectors of a coated glass plate as a function of TPB coating thickness. Reproduced from [106].

negligible for the position measurements. TPB can thus be considered transparent to its fluorescence light in the range of thickness here considered (≤ 0.6 mg/cm^2).

4.3.3 Response of Coated SiPMs

One of the most important variables when using TPB coated SiPMs is the thickness of deposition, since the fluorescence yield is proportional to the thickness of the wavelength shifter [102]. The simplest way to optimize the fluorescence is by comparing the current generated by a set of SiPMs without TPB and for a set of deposition thicknesses. Tests were performed using LEDs with light output at wavelengths in the range 240-400 nm with constant illumination of the devices under test [106]. It was found that the peak output corresponded to a deposition thickness of 0.05 mg/cm^2, a result in good agreement with

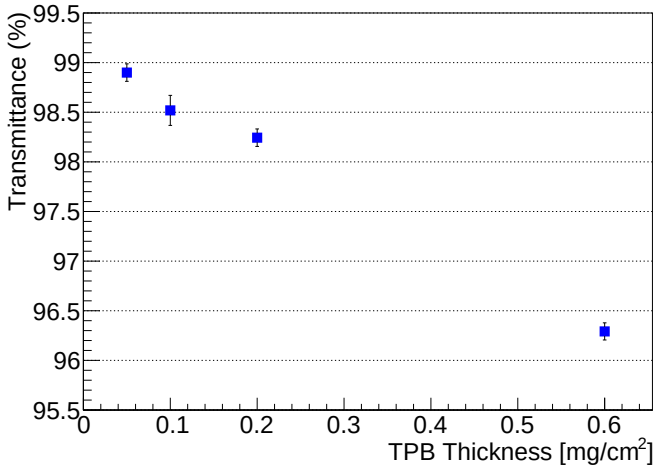

Figure 4.21: Transmittance of the TPB at its emission wavelength as a function of TPB thickness. Reproduced from [106].

the literature [102]. However, coating to this thickness results in a high level of inhomogeneity across the surface which would result in a large variance in fluorescence between different channels. The simultaneous optimization of thickness variance and high yield lead to a choice of 0.1 mg/cm^2 thickness.

Using the procedure described in § 4.2.7, the experimental determination of the photon detection efficiency of a set of S10362-11-050P coated with 0.1 mg/cm^2 of TPB was done in the spectral range 250-315 nm. The results are shown in Figure 4.22, where TPB coating appears to increase their PDE by a factor eight in this UV range, from about 2% to about 16%. Thus, in this way the sensors are better adapted to the conditions of the detector.

Coating the sensors with TPB can also be seen to improve linearity. Figure 4.23 shows the response curve at different illumination levels of a 0.1 mg/cm^2 TPB coated S10362-11-050P SiPM using the method

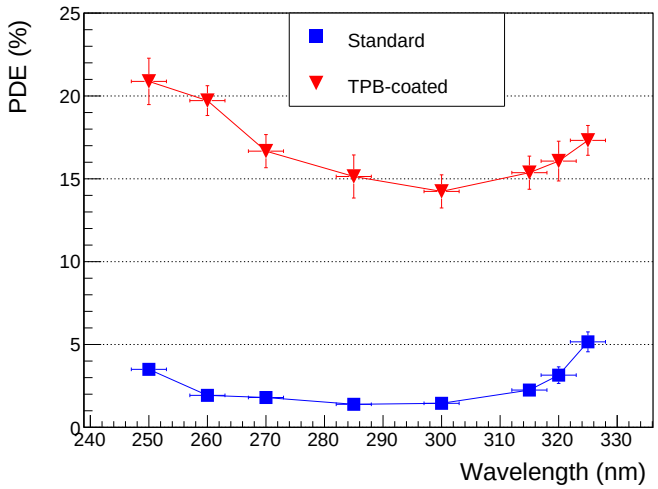

Figure 4.22: Measured PDE of a coated S10362-11-050P as a function of wavelength in the spectral range 250-315 nm, extracted from [100].

described in § 4.2.8. As can be seen, the response of the coated SiPM starts to deviate from linearity when about a quarter of the total number of pixels are simultaneously fired and produce a photoelectron ($N_{rec} >$ 100), practically increasing by a factor two the range where the SiPM has a linear response, if compared with Figure 4.17.

4.4 Dice Boards

Due to the large number of SiPMs needed to form the tracking plane in NEXT — 256 for the *tracking plane* of NEXT-DEMO and more than 7000 for NEXT-100 — it is impractical to apply an individual bias voltage line to each sensor, as it would require a huge amount of connections to extract the signal from the pressure vessel.

For that reason, the SiPMs are mounted in groups of 64 sensors on multilayer *CuFlon*® Printed Circuit Boards (PTFE substrate with

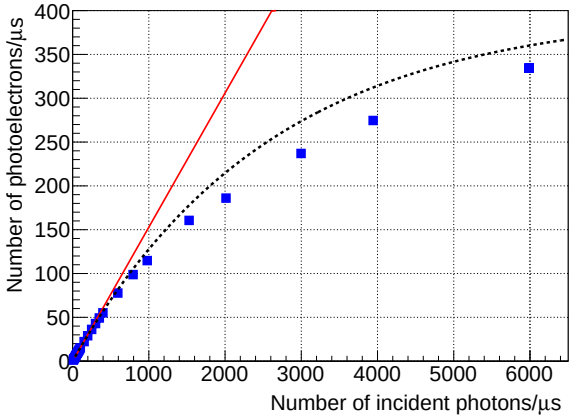

Figure 4.23: Response curve at 285 nm of a TPB coated S10362-11-050P, reproduced from [100]. The solid red line represents the linear fit to the data at low illumination levels. The dashed black line represents the theoretical response curve following equation 4.11.

copper layers, gold plated). *CuFlon* has the advantage of high light reflectivity and low degassing.

All sensors of this system, called *Dice Board* (DB) (see Figure 4.24), share their common bias voltage through a common cathode line via a FPC (Flat Printed Circuit) kapton cable which also extracts the sensor signals and the readings of a thermister positioned next to the board. In order to maintain the nominal supply voltage of the sensors and reduce detector dead time, four tantalum capacitors are connected to each DB and supply the sensors with the required voltage after the breakdown of the pixels (see Figure 4.24-*right*).

Due to the Geiger mode operation of the SiPMs, a relatively small variation of the bias voltage induces a large variation of the gain. For that reason, the grouping of the sensors must be carried out in such a way that the dispersion in response of a DB is as low as possible. This

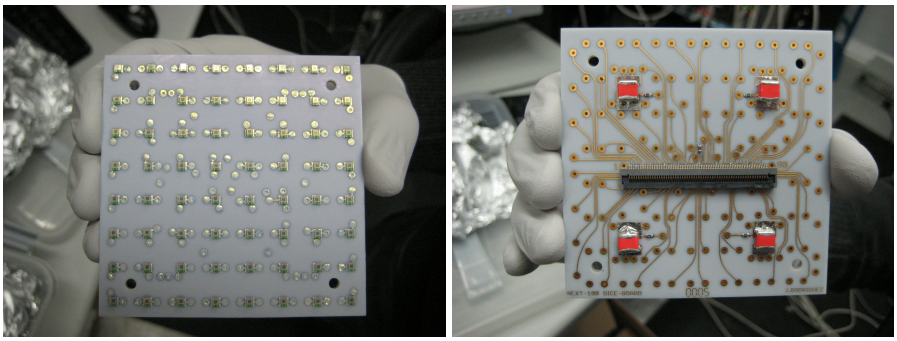

Figure 4.24: Left: Front view of one Dice Board of the NEXT-DEMO Tracking Plane with 64 SiPMs. Right: Back view of the DB containing the four tantalum capacitors and conector.

has been done considering the individual gain of each device at a given operating voltage and grouping the sensors which have the most similar gains under these conditions.

Once mounted, each DB was placed inside a dark box and supplied with the average of the voltages determined for each individual sensors as optimal at operating temperature. Using a 400 nm LED, the individual single photon spectrum of each SiPM was registered and their gain calculated following the method described in § 4.2.2.

The gain spread within the four DBs of the NEXT-DEMO *tracking plane* varies between 2% and 3.6%, this variation is within operational tolerance for NEXT-DEMO. The average gain of each DB is in the range $(2.27\text{-}2.50)\times10^5$.

After these measurements, the DBs were coated with vacuum-evaporated TPB, following the protocol described in § 4.3.1, and then stored in a N_2 atmosphere to prevent TPB degradation prior to their introduction in NEXT-DEMO (see Figure 4.25).

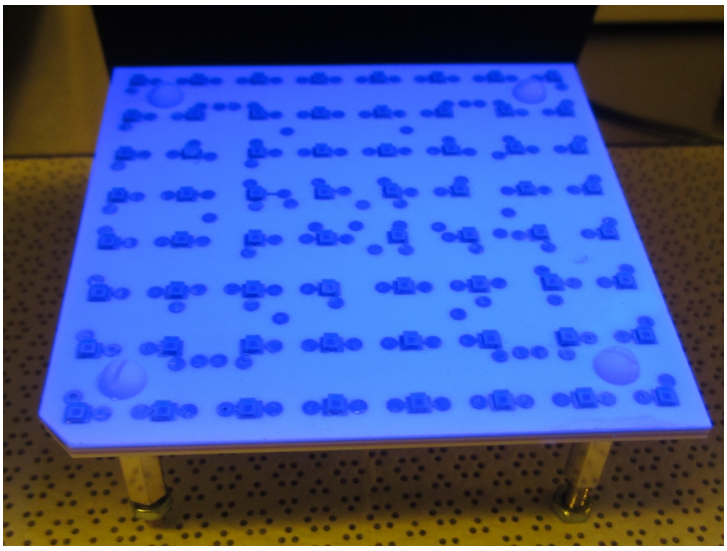

Figure 4.25: TPB-coated Dice Board illuminated with an UV lamp and reemitting in the 430 nm TPB emission peak (blue).

4.5 Tracking Plane Electronics

The processing of the SiPM signals is performed by a 16-channel front-end (FE) board (Figure 4.26) including 16 analog paths and a digital section [107]. Each analog path consists of three stages. The first stage is a transimpedance amplifier which converts the SiPM current into a voltage signal providing a gain of 1.5 V/mA and baseline adjustment. The second stage is a gated integrator with 22 ns RC constant and a nominal integration time of 1 μs. An offset control at the first stage enables the optimization of the integrator dynamic range. The third stage is an inverter with a gain of 1.2 required to produce a positive signal at the ADC input. An offset correction is included at this stage since the integrator introduces an output deviation. The three electronics stages are manufactured using the OPA659 operational amplifier from Texas Instruments [108].

The signals obtained in the outputs of the analog paths are digitized at a rate of 1 MHz using 12-bit ADCs (4096 channels). In the digital section, a configurable FPGA (Xilinx Spartan 3A) is used to read the ADCs, control the switches in the gated integrators, build a frame with the digitized data and communicate with the upstream readout stage through a standard RJ-45 connector and cable. Careful PCB layout techniques ensure that the digital section introduces very little noise in the analog section.

The gains in the three stages of the analog section have been set to obtain an output level which can resolve single photoelectrons. For the system to have this resolution, the output voltage obtained from a single photoelectron should be higher than the equivalent output noise of the circuit which has a typical standard deviation of 2 mV. The gain values at the different stages are set to obtain a voltage level of 17 mV/pe for signals from S10362-11-50P SiPMs. The gain values in the analog stages can be further modified in order to adjust the ADCs dynamic range to the level of real tracking signals from the TPC.

The front-end cards are read out by the Front-End Concentrator (FEC) card, designed within a joint collaboration between CERN-PH-AID and NEXT in the framework of the RD-51 Collaboration [109, 110]. Up to 16 front-end cards can be connected to the FEC module, resulting in 256 channels, which is the number of channels of the NEXT-DEMO prototype. This readout system can be scaled up for NEXT-100 by simple addition of FEC cards. The data are sent to the data acquisition PC via gigabit Ethernet links.

The front end electronics in NEXT-DEMO are placed outside the chamber for reasons of space inside the TPC and accessibility of the front end cards for development studies and maintenance. These cards are placed close to the detector in order to minimize signal losses through cables.

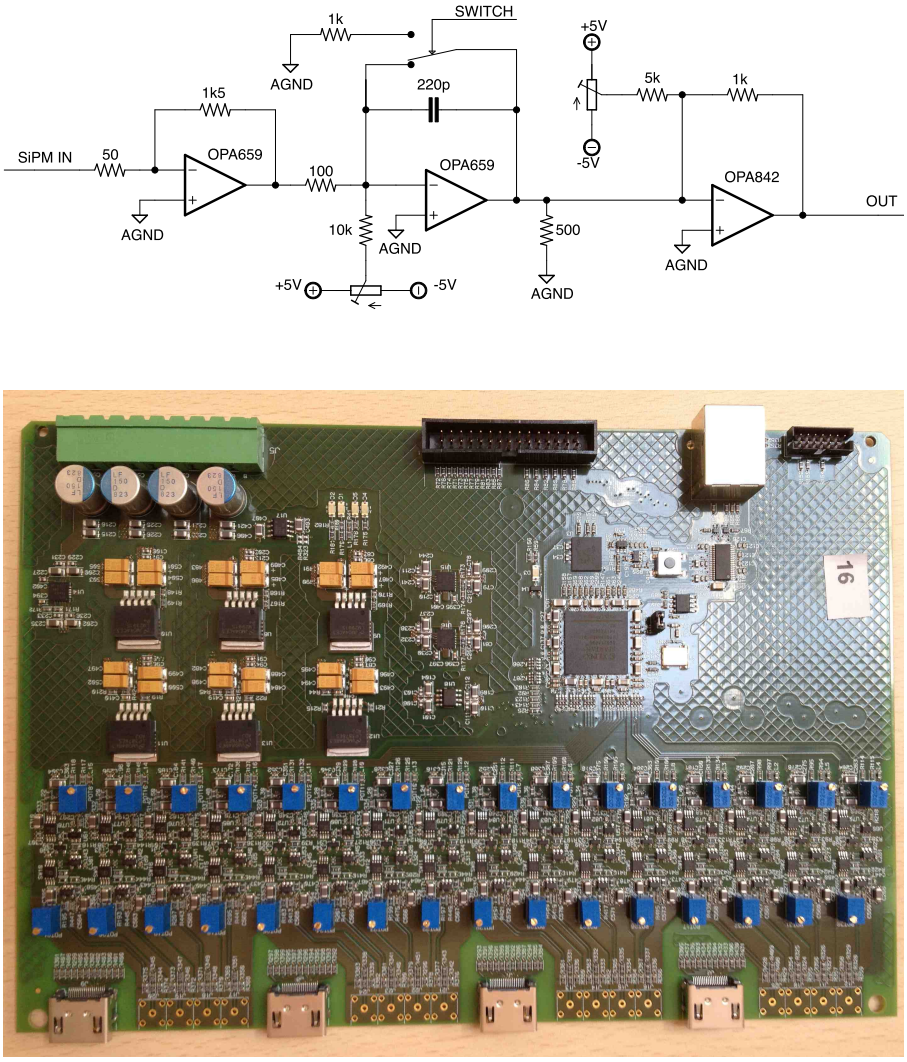

Figure 4.26: Top: Electronic scheme of one analog path including its three stages. Bottom: View of one front-end (FE) of NEXT-DEMO. 16 FEs are needed to the full read-out of the tracking plane.

4.6 Active Control of the Gain

SiPMs are known to be sensitive to temperature changes, their gain being highly anti-correlated with this variable [111]. This is because at high temperature, electrons lose more energy to crystal lattice scattering by emitting phonons, thus they need a higher field to acquire the energy needed for impact ionization [90]. Therefore a higher bias voltage is needed to create stronger electric field in the diode for the breakdown condition.

Temperature variations inside the NEXT-DEMO prototype were expected to be no more than a few °C during the detector operation, but they changed due to the continuous gas flow in the TPC which ensured the cleaning conditions of the gas. Therefore, the stabilization of the SiPMs gain had to be done in such a way that ensured the homogeneous response of the tracking plane.

A dedicated experimental setup was designed for the study of the temperature dependence of the SiPMs used in NEXT (see Figure 4.27). A small board, similar to the Dice Board described in § 4.4 but containing only four sensors, was coupled to a copper block which had a hole pattern similar to the pitch of the SiPMs, in such a way that sensors were inside the holes. A *Peltier cell* was glued on the other side of the copper block, so the temperature in the set could be changed by varying the current across the cell. The temperature of the system was measured using a digital thermometer DS18B20 from Maxim Integrated Products Inc. [112], with a programmable resolution of 9-bit to 12-bit and an accuracy of ±0.5°C over the range -10°C to +85°C, located in different positions over the copper. This system was placed inside a small black box and the SiPMs signals processed by the electronics described in § 4.5.

As explained in § 4.2.5, within the electronic sample time (1 μs), a different number of dark count events are produced spontaneously.

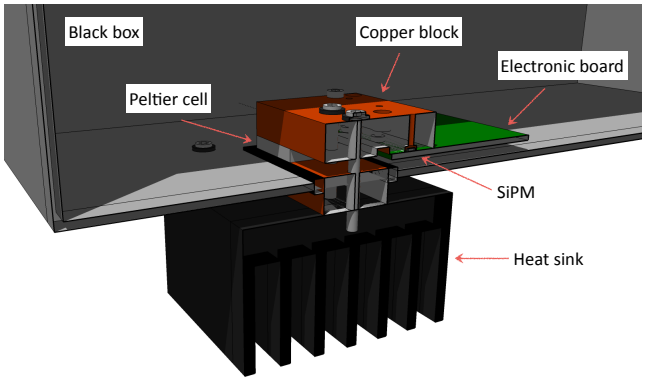

Figure 4.27: Transverse cross section drawing of the experimental setup indicating the main components.

These are registered by the setup described above producing the waveform shown in Figure 4.28, which presents entries at different intensities corresponding to the number of fired pixels. Using these events, the typical single photon spectrum of the SiPMs was recorded for a range of bias voltages between 73.07-73.82 V, the nominal voltage of the DB being 73.57 V. These measurements were carried out keeping constant the temperature in a wide range (20 to 30°C in steps of 1°C). As commented in § 4.2.2, the gain of the sensors can be extracted from their SPS (see Figure 4.29) by fitting the peaks distribution (see Figure 4.30), but this time in ADC counts due to the digital response of the system. This procedure can be done due to the extremely low electronic noise introduced by the system, as can be seen in the width of the leftmost peak in Figure 4.29, which allows to resolve single photoelectron peaks.

The calculated gain of the four SiPMs versus the applied bias voltage is represented in Figure 4.32 at four temperatures. The data were

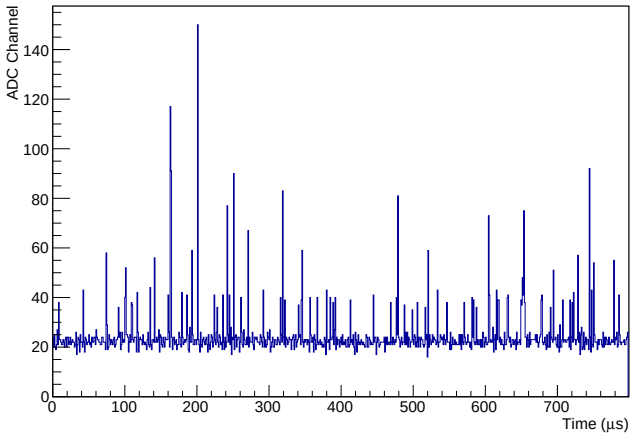

Figure 4.28: Typical dark count waveform of the S10362-11-050P with a sample time of 1 μs.

fitted to equation 4.3 and their slopes (Voltage coefficients) plotted in Figure 4.33-*left*. In the range where SiPMs were operated, a spread in gain lower than 4% was obtained at all bias voltages while the voltage coefficients were observed to be constants and therefore independent of temperature.

Similarly, the calculated gain of the four SiPMs as a function of temperature is represented in Figure 4.32 at four constant values of bias voltage, obtaining a spread in gain in every temperature configuration lower than 6%. As can be seen, the gain of a device decreases with increased temperature. This is predominantly due to electron energy loss to phonons.

According to the behavior shown in Figure 4.32, gain variations due to temperature changes can be modeled as

$$G = b^* + a^* \cdot T \tag{4.14}$$

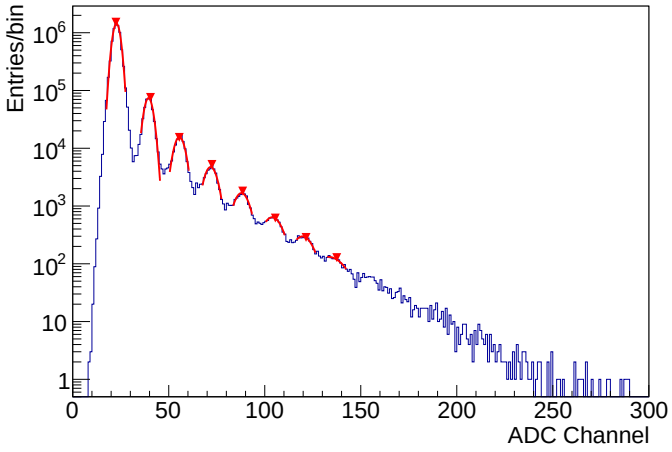

Figure 4.29: Typical dark count spectrum of the S10362-11-050P recorded in a sample time of 1 μs. The gaussian fits to the photoelectrons peak are shown.

where a* is the temperature coefficient of the gain. This equation has been applied to fit the calculated data of gain, obtaining the temperature coefficients shown Figure 4.33-*right*. The coefficients do not depend on the operating voltage and have a spread of less than 4%.

Based on these results, the assumption that gain variations due to temperature fluctuations can be compensated with the control of the bias voltage is established. Thus, an increase in temperature requires an increase in operating voltage to keep the gain constant and vice-versa. The relation factor between temperature and bias voltage variation required at a certain temperature can be easily obtained from equations 4.3 and 4.14:

$$a \cdot \Delta V = a^* \cdot \Delta T; \Longrightarrow \Delta V = \frac{a^*}{a} \cdot \Delta T \tag{4.15}$$

Taking as reference the nominal voltage of the Dice board at room temperature (25°C), the required bias voltage applied to compensate

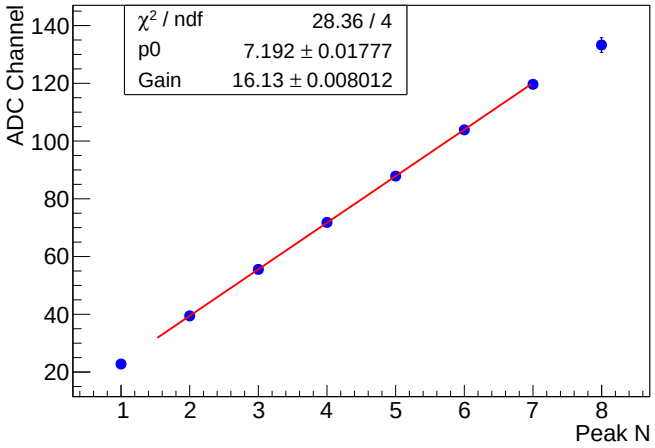

Figure 4.30: Average number of ADC counts produced by different number of fired pixels and linear fit extracting the channel gain.

temperature variations is given by

$$V_{bias} = V_{25°C} + \Delta V \tag{4.16}$$

A specially designed power supply has been developed to achieve this goal [113]. The system is based on a commercial power supply module, the APp0250512 from ISEG-HV [114], whose output voltage can be set from 0 to 200 V with a control voltage of 0 to 5 V. The voltage is controlled via a 16 bit SPI DAC with 4.096 V reference voltage, providing a resolution of 62.5 μV. This allows the control of the output voltage in steps of 2.5 mV. This voltage resolution is good enough, since Hamamatsu specifies the nominal voltage of each SiPM with a precision of tenths of mili-volts.

A 16 bit SPI ADC monitors the output voltage of the module and corrects (if necessary) the control voltage. This allows compensation for possible drifts in the power supply module output.

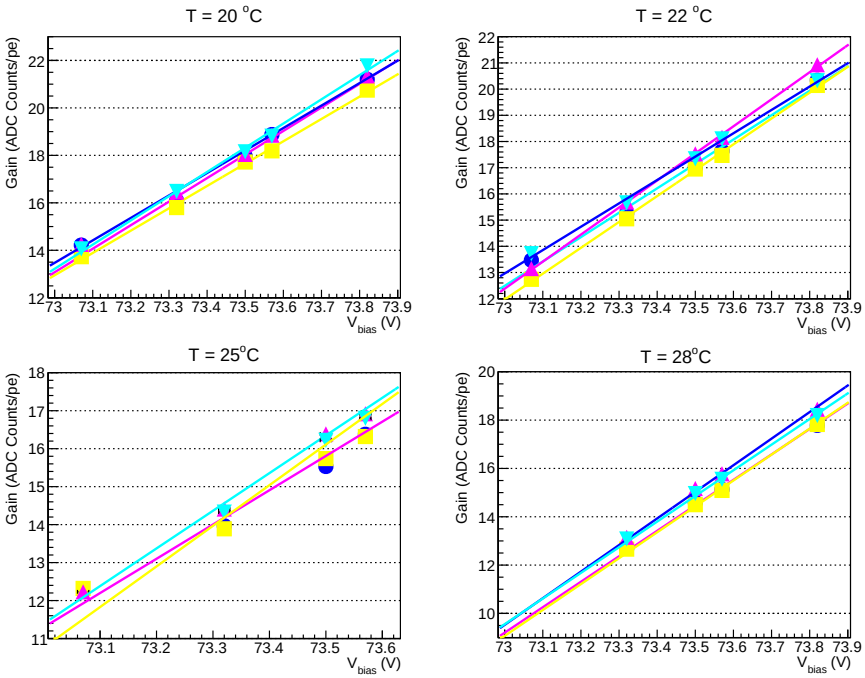

Figure 4.31: Gain versus bias voltage for four SiPMs at four different temperatures.

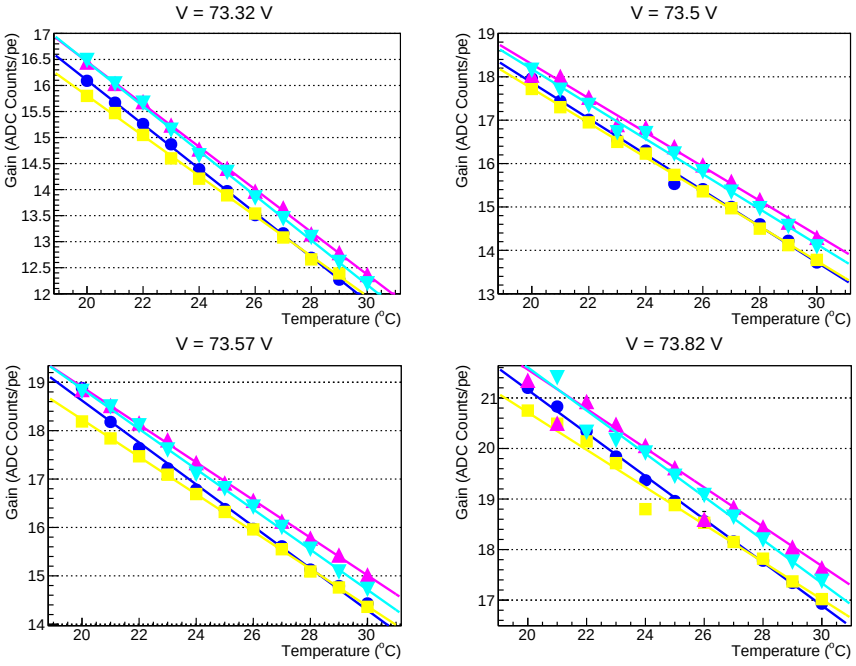

Figure 4.32: Gain versus temperature for four SiPMs at four constant bias voltages.

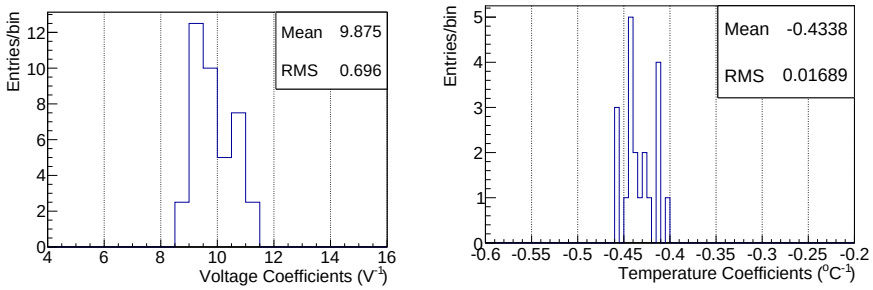

Figure 4.33: Left: Voltage coefficients extracted from the calculated data fitted to equation 4.3. Right: Temperature coefficients extracted from the calculated data fitted to equation 4.3.

A computer with LabVIEW reads the temperature sensor placed in the DB and communicates with the microcontroller via a USB interface for the setting of the nominal bias voltages and also for the control and monitoring of the power system. The system stores the values of temperature and corrections applied in ascii files for further data analysis.

To evaluate the performance of the system, the gain of a SiPM was measured for a temperature range from 20 to 30 °C. Figure 4.34 shows the calculated gain of the SiPM without (blue) and with (red) temperature compensation. As seen, gain variation is reduced from nearly 30% to only 0.5% for a range of 10 °C.

This solution ensures the correct and homogeneous response of the *tracking plane* during long runs of data taking where temperature conditions inside the TPC could drift in such a way that would modify the output signals of the SiPMs.

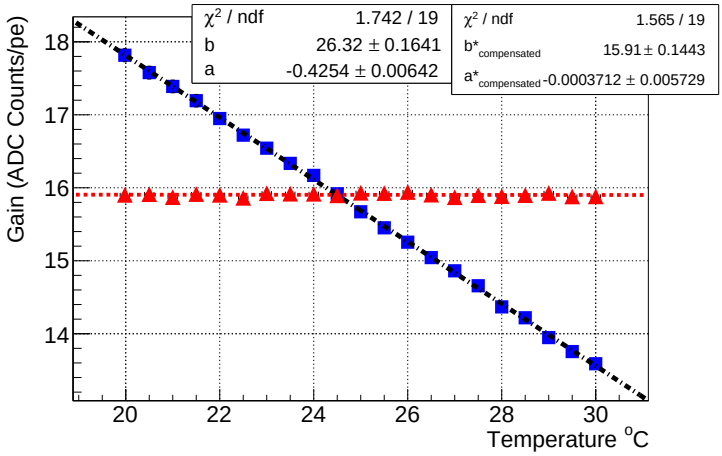

Figure 4.34: Gain of a SiPM without (blue) and with (red) temperature compensation in range from 20 to 30 °C.

4.7 Installation of the Tracking Plane

The installation of the *tracking plane* in the NEXT-DEMO detector has been made following a strict protocol to ensure clean conditions and prevent the contamination (with dust, humidity, etc.) of the detector while it is open.

The NEXT-DEMO *tracking plane* is formed by 256 SiPMs grouped in four TPB-coated Dice Boards. These DBs are assembled on a structure that ensures the robustness of the system. The structure is fixed to the vessel end-cap, around 5 mm behind the double mesh where EL light is produced (see Figure 4.35). Additionally, a 400 nm LED is mounted between the four DBs, centered in the TPC. It is used for the calibration of both sensor planes. Kapton cables which extract the SiPMs signals are guided through conduits present in the end-cap and connected to a feedthrough which ensures the system remains airtight. On the other

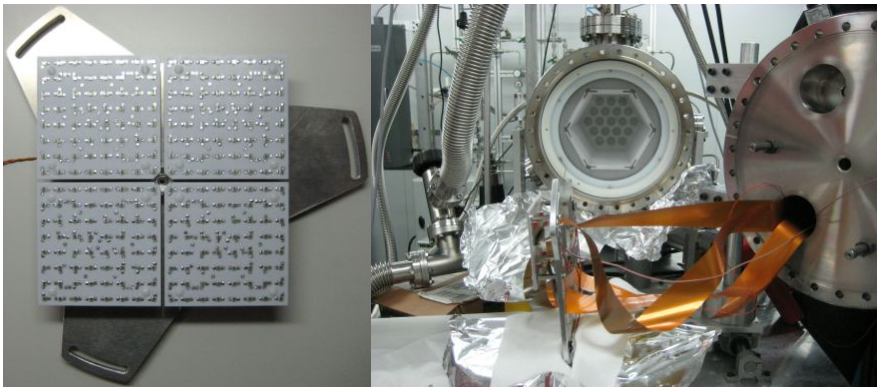

Figure 4.35: Left: Four Dice Boards which comprises the NEXT-DEMO tracking plane. Right: Mounting the tracking plane in the NEXT-DEMO detector.

side, a specially designed board groups each four output channels to a standard HDMI connector, reducing the number of required lines. Here, 64 HDMI cables (16 per DB) are needed to fully read the plane. Four HDMI cables are connected to one FE described in § 4.5, so 16 FEs are needed to digitize the SiPMs signals. These in turn are connected to two FEC (8 FE per FEC) which assemble the data packets. In addition, one trigger FEC synchronizes the *tracking plane* signal with the PMTs located on the other side of the detector. The whole system is read by the DAQ software DATE.

The xy position of each sensor is stored in a database in such a way that the signal of each electronic channel is associated with a two dimensional location inside the TPC.

Prior to the four DBs being supplied at their nominal voltages, an offset correction must be done to optimize the electronics dynamic

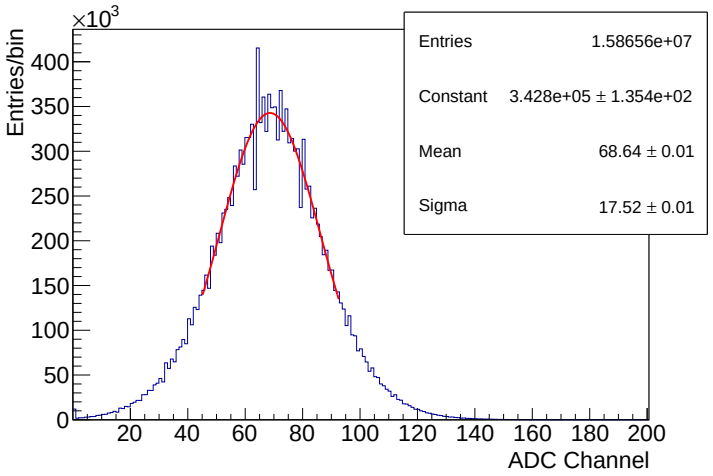

Figure 4.36: Histogram with the distribution of the baseline of one electronic channel. The offset is taken as the mean value of the gaussian fit and stored in the database for the posterior subtraction.

range, given by the 12-bit ADC, so a range from 0 to 4095 ADC counts is possible.

Due to baseline fluctuations, the offset of each channel must be positioned at a positive, close-to-zero value, but sufficiently high that signals produced when baseline presents a minimum do not produce a value below zero, which would result in the loss of information. This is solved by adjusting the potentiometer located at the second stage of the FE (see § 4.5), which controls the voltage on the negative branch of the ADC, in such a way that the output is within 50 and 80 ADC counts.

After the manual adjustment of the 256 channels is made, the offset of each channel is taken as the mean value of the the Gaussian fit obtained from the histogram of the baseline entries (see Figure 4.36). This value is also included in the database mentioned above in order to be subtracted during the posterior analysis.

As can be observed in Figure 4.36, the distribution is wider than the one obtained in the SPS of Figure 4.29, which represents the electronic noise introduced by the system. This effect, that will be analyzed later, does not allow the single photoelectron peak's resolution, making impossible the calibration of the SiPMs as it was done previously using dark count events.

Research is what I'm doing when
I don't know what I'm doing.

Werner von Braun

CHAPTER

5

Commissioning and Results

This chapter comprises two parts, both concerned with the NEXT-DEMO prototype. First, we summarize the commissioning of the *tracking plane* described in Chapter 4, the problems that emerged during this operation and the techniques developed to resolve such problems.

Second, we describe the use of X-ray emission by the atoms of xenon as a multi-tool in xenon gas detectors. X-ray energy depositions are used to study xenon gas properties at 10 bar pressure, like electron diffusion in gas and drift velocities. At the same time, they are employed to calibrate the response of the sensors inside the detector and to obtain the spatial response dependence by an EL-based amplification. Finally, energy released by gamma particles coming from external sources has been reconstructed using a novel method, achieving excellent energy resolution in the NEXT-DEMO prototype [4].

5.1 Internal Calibration

The absolute gain of the SiPMs was calculated prior to their introduction in the TPC using their single photon response to illumination with a 400 nm LED, as commented in § 4.4, achieving a gain spread between 2% and 3.6% at their nominal voltages. However, due to the posterior addition of a wavelength shifter coating (TPB) over the SiPMs, to make them sensitive to the xenon scintillation light, together with the addition of the electronic read-out chain, an independent calibration is required to give a true representation of the relation between photoelectrons (pes) and ADC counts.

This requirement can be observed in Figure 5.1, where the correlation in the response between both planes of sensors to a ^{22}Na source, located at one of the external ports for calibration present in the vessel is shown. Figure 5.1 shows how for a constant energy registered by the energy plane (cathode sum in figure), a wide range of responses in the tracking plane (anode sum in figure) are registered. This effect indicates that the calibration constants used at this level of the analysis are not correct, as they do not include the mentioned effects.

A measurement of the dark current of the SiPM channels would provide directly the conversion factor. However, once the tracking plane was introduced inside the detector, an increase in the noise levels was observed, as represented by the fluctuations in the baseline of one electronic channel, shown in Figure 5.2-*left*. The origin of this noise was identified as the electrical facility of IFIC where all electronics were connected. Using a LeCroy 500 MHz passive probe [115], bursts of about 3 kHz with a few MHz noise were identified on the ground line of the electrical facility. These frequencies overlap by capacitive coupling to the readout distorting the baseline. Different filters were employed in order to cancel such frequencies, however, they were not very efficient, allowing the sensors to pick up this noise.

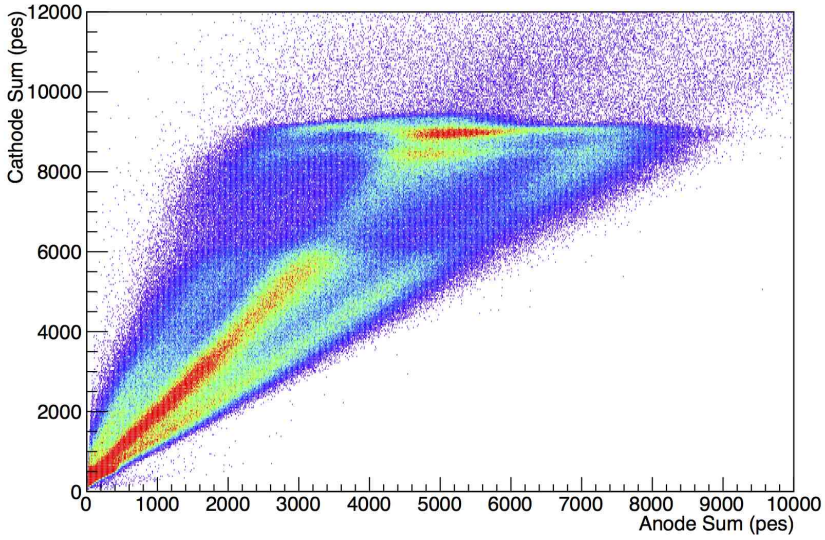

Figure 5.1: Anode-cathode correlation response to a ^{22}Na source using external calibration constants.

As can be observed in Figure 5.2-*right*, this noise produced that the peaks of the dark current distribution were not distinguishable, so the detected signal is actually a convolution of the signal produced by dark count events with the pickup noise. For this reason, three independent techniques are introduced here to perform the calibration or equalization of the SiPMs. The response of the SiPMs to X-ray depositions present in data, the photon transfer curve technique using a blue (400 nm) LED and the common noise filtering.

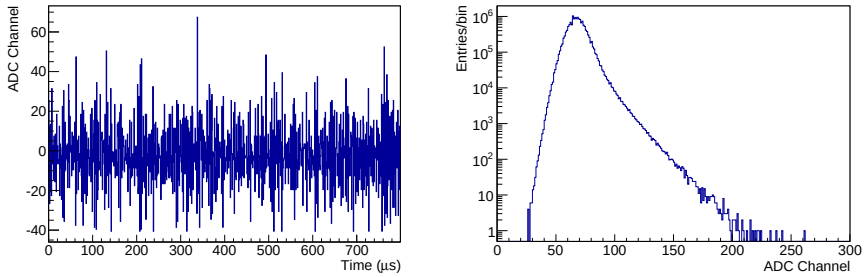

Figure 5.2: Left: Noisy baseline waveform from one electronic channel. Right: Digital SPS of one SiPM where the pickup noise make impossible to resolve photoelectrons.

5.1.1 X-ray Calibration

X-ray energy depositions have been identified as a useful resource for the homogenization of the SiPMs response. As will be discussed in § 5.2, such events are produced by the 30 keV electrons extracted by gamma rays coming from external sources. These events are very abundant during data taking, providing thousands of depositions distributed all around the active volume of the detector.

The range of those e^- at 10 bar is ~0.6 mm [116], which by multiple scattering deposits all its energy at the production point. The blob of charge produced drifts toward the anode due to the electric field present in the chamber, where it produces EL light. Since the SiPMs that form the tracking plane are located just a few millimeters away from the EL generation region, the forward photons tend to be concentrated in few channels. Considering as estimator of the energy released in each recorded event only the channel with maximum charge, a low energy spectrum is reconstructed for each channel (example in Figure 5.3), which exhibits a peak corresponding to the X-ray energy. The 30 keV peak is fitted, and its mean value used to characterize the response to X-rays.

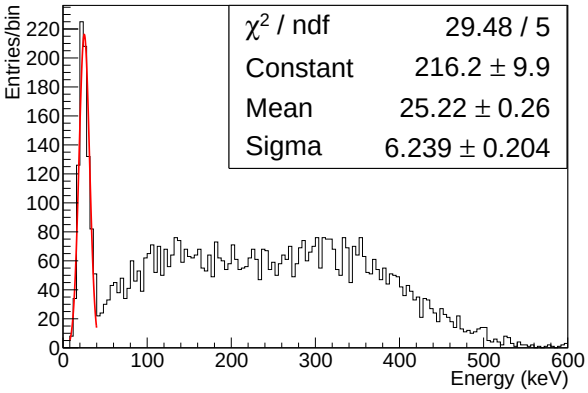

Figure 5.3: "Low energy" spectrum of ^{22}Na obtained with one SiPM of the tracking plane, and gaussian fit to the X-ray peak.

The position of the X-ray peak is different for each channel. These differences are used to homogenize the response of the SiPMs, slightly modifying the original gain of the sensors. Once gains are modified, the correlation between both planes changes as shown in Figure 5.4, achieving a linear response between the two planes.

5.1.2 Photon Transfer Curve

While the X-ray method can be used over the course of a run with a radioactive source to monitor the equalization of the gains, it is not possible to measure the actual gain values using this method. As an additional method of absolute determination of the gain in the absence of the dark current method, the Photon Transfer Curve (PTC) method using a blue LED is proposed here.

From a very basic point of view, a read-out channel, composed by a SiPM plus its associated electronics, is a system block with light as input, and digital data as output. The only noise introduced at the

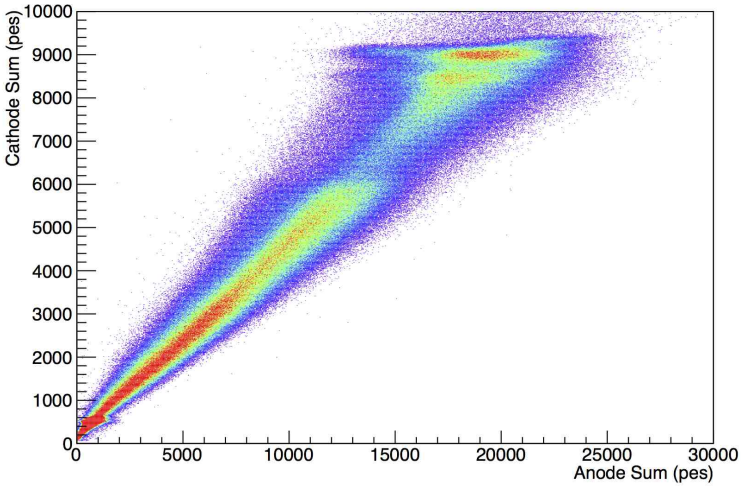

Figure 5.4: Anode-cathode correlation response to a ^{22}Na source after apply the X-ray calibration method.

input corresponds to the fluctuations associated to the light source and it is know as *shot noise* [117]. A random noise can be associated to the read-out channel and its processing electronics, and represents the baseline noise in total darkness. Illuminating the SiPM, as the input light level increases in amplitude, the noise at the system output rises out of the baseline noise and becomes dominated by shot noise. Shot noise is directly related to the input illumination I, satisfies Poisson statistics and is therefore proportional to the square root of that signal:

$$\sigma_I = \sqrt{I} \, . \tag{5.1}$$

The Photon Transfer Curve is shown in Figure 5.5-*top* for an individual read-out channel, and illustrates the various noise regions.

During the PTC measurements, the SiPM was exposed to a blue LED located at the TPC cathode producing an uniform illumination, and pulsated at different reverse bias voltages. The digital SiPM response (S_{ADC}) at different intensities is represented in Figure 5.5-*bottom*.

The Gain of the full system G, typically expressed in ADC/e^{-}, is the number of ADC counts per single electron. For an increase in illumination I, the digital SiPM response will change by $S_{ADC} = G \cdot I$, while $\sigma_{ADC} = G \cdot \sigma_I$. According to equation 5.1:

$$\sigma^2_{ADC} = (G \cdot \sigma_I)^2 = G^2 \cdot I = G \cdot S_{ADC} \tag{5.2}$$

The absolute gain value of the system can be extracted from equation 5.2 as the slope of the linear fit between the digital SiPM response (S_{ADC}), and the square shot noise of the signal. Figure 5.5-*top* shows this linear fit for one of the channel of the *tracking plane* with the fitted gain.

The linearity range of the SiPMs was discussed in § 4.2.8. At the light intensity levels used in this study, a maximum of around 130 pixels are fired per event, which corresponds to $\sim 30\%$ of the active region. Under these conditions the sensor's response can be considered linear.

The gain values obtained with the PTC method match perfectly with the values calculated during the external calibration using dark count events, making of this method useful for further monitoring of the gain during the data taking.

5.1.3 **Common Noise Filtering**

The Common Noise Filtering (CNF) method is based on the idea that the noise induced in the electronics has a common pattern since the source of the noise is common to all channels even if their response is not the same. This electronics noise contains a high frequency component of a

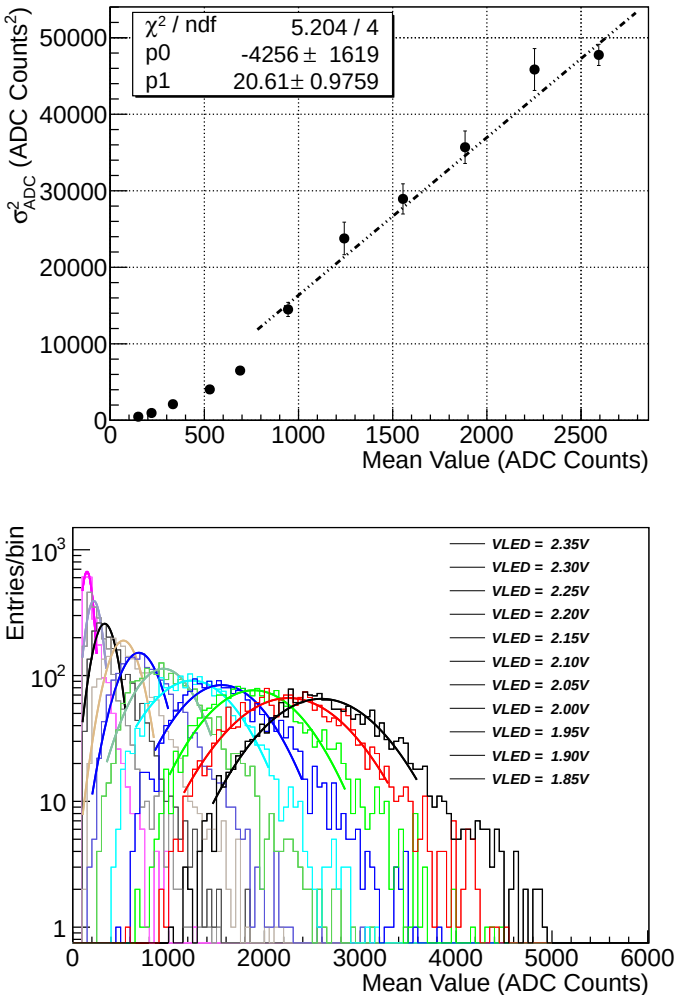

Figure 5.5: Top: Photon Transfer Curve of a SiPM and linear fit in the shot noise region obtaining the absolute gain of the system. Bottom: Average response of the SiPM at different illumination levels of the LED and gaussian fit to the mean value.

few MHz which increases the width of the baseline fluctuations making impossible the resolution of single photoelectron peaks.

The passive components mounted on all channels of the Front Ends (capacitors, resistors, etc.) have the same nominal values. However, due to the tolerance range given by the manufacturer, their actual values are within a 5% of the nominal ones. This small difference is the main contribution that makes the response not exactly the same in all channels. Figure 5.6-*left* shows the baseline distribution for four channels within one FE once their offset have been subtracted. These distributions can be modeled as a Gaussian, and therefore their response R is described by

$$R(x) \sim \exp\left(-\frac{1}{2}\left(\frac{x-\mu}{\sigma}\right)^2\right) \tag{5.3}$$

where μ is the mean value (must be zero after offset subtraction) and σ is determined by the electronics gain, dominated by the combination of the first and third stages of the FE.

After setting all electronics channels to equation 5.3, they are normalized according to their sigmas, eliminating the unevenness from the components and leaving only the effect of the pickup noise (see Figure 5.6-*right*). Then, a noise model may be established to describe the average noise in a sample time:

$$\bar{R}_{CNF}(t) = \frac{1}{n}\sum_{i}^{n}\frac{R_i(t)}{\sigma_i} \tag{5.4}$$

where $R_i(t)$ is the ADC value of the channel i at a sample time, σ_i its normalization and n the number of channels within the Front End. These parameters have been determined for every FE individually.

The signal recorded by electronics, is actually the convolution of the signal generated by SiPMs with the pickup noise in the system. The fact that dark count events are produced randomly following Poisson

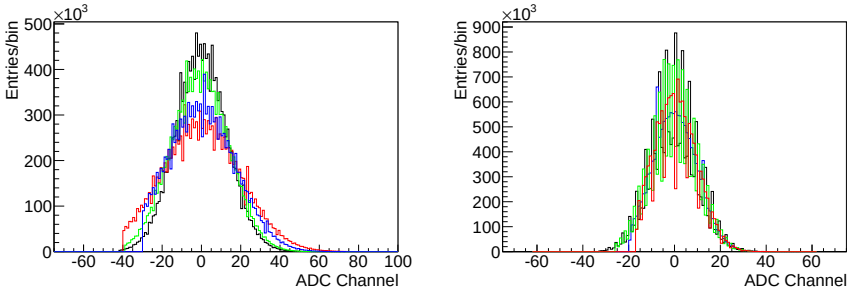

Figure 5.6: Left: Baseline distribution of four channels within one Front End without (left) and with (right) normalization by their electronics gains. Gain taken as σ in equation 5.3.

statistics, makes these events uncorrelated with the pickup noise, and this the latter can be subtracted leaving only the relevant information of the SiPMs. This is shown in Figure 5.7, where a waveform of a biased SiPM is represented before and after the CNF model is applied. Once subtracted, dark count events are clearly visible, allowing the construction of the SPS with peak identification and therefore, the sensor calibration.

The correlation within the absolute constants obtained by applying the CNF method is similar to the one obtained with the other methods, ensuring the reliability of the three methods described in these sections.

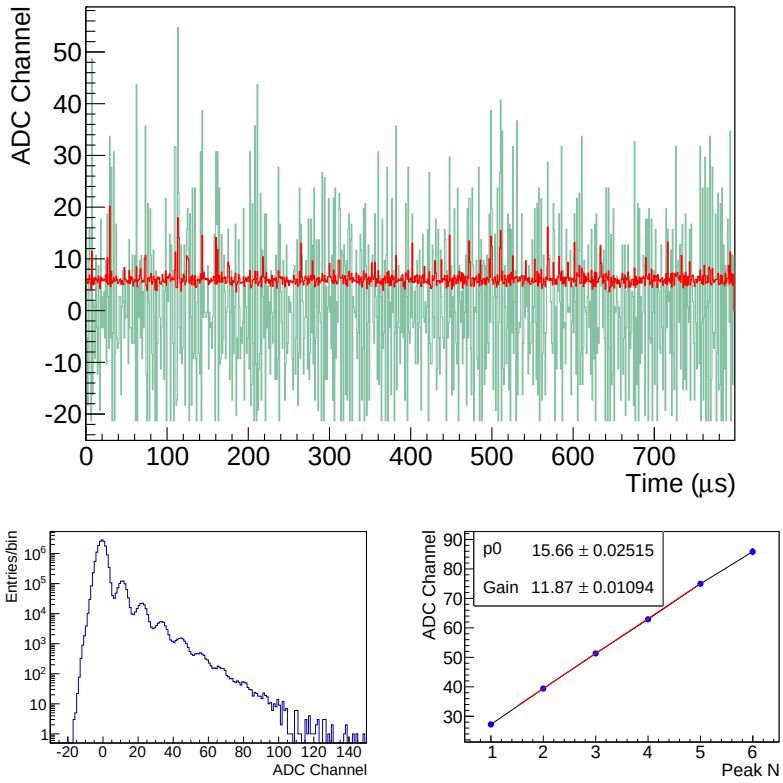

Figure 5.7: Top: Waveform of a biased SiPM with dark count events before (green) and after (red) CNF is applied. Bottom: Single Photon Spectrum obtained with DK events after CNF (left) and linear fit to extract its gain (right).

5.2 X-rays Production in Xenon

In xenon, as in most noble gases, there exists a non-zero probability that an interacting photon will excite the K or L shells of an atom causing the emission of an X-ray. This can take place in two ways (illustrated in Figure 5.8):

1. The gamma directly excites an electron which upon de-excitation emits a K/L-shell X-ray.

2. An electron from the K/L shells is knocked out of the xenon atom. The hole is then filled by an electron from a higher shell, which emits an X-ray.

In both cases, the X-ray will travel on average around 1.39 cm at 10 bar [118] before interacting with the gas, producing a photoelectric electron. In xenon in the range of sensitivity of NEXT the most important lines are the K_α and K_β emissions with 29.7 keV and 33.8 keV respectively. Electrons produced at these energies will travel a maximum CSDA distance ~0.6 mm at 10 bar [116] but will tend to displace from their production point by less due to the important of multiple scattering. The abundance of such events and their effectively point-like nature make K-shell X-ray interactions useful tools for the calibration of the detector. They can be used to study fundamental properties of the gas and drift region as well as to equalise the energetic response which varies due to detector geometry.

5.3 Data Sets, Preprocessing and Selection

The analysis presented in the following have been produced by using two different sources, ^{22}Na and ^{137}Cs, located in two different positions in the NEXT-DEMO detector (see Figure 5.9). In *Configuration 1* the sources were located between one of the transparent lateral ports of

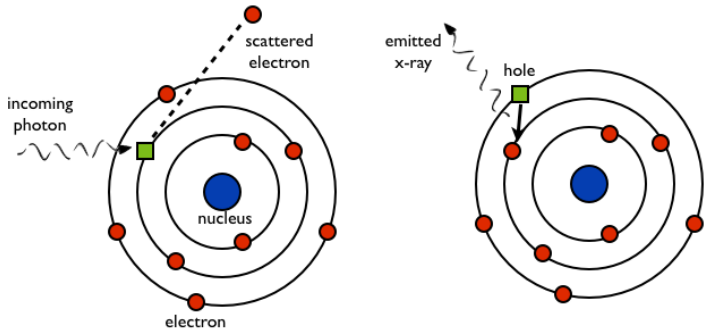

Figure 5.8: X-ray emission process. An incoming photon with enough energy extracts an electron from the K, L shells (left). The hole is filled by a more energetic electron with the consequent emission of an X-ray (right).

the vessel and a NaI scintillator placed outside. When the ^{22}Na source was placed in this configuration, read-out was triggered by coincidence between a signal produced by primary scintillation (S1) and a pulse in the external NaI scintillator. This trigger is possible because of the back-to-back photons produced in positron annihilation, as ^{22}Na is a β^+ isotope. When using ^{137}Cs, the trigger consisted of a combination of S1-like signal of at least three of four central PMTs. In *Configuration 2*, sources were located centered in one of the end caps of the vessel, axis $Z = 0$. The trigger required the coincidence of an S1-like signal in at least 3 central PMTs.

Raw data first passes through a data preprocessing algorithm common to all analyses. This applies pedestal correction to all channels before identifying S1-like and secondary scintillation signals (S2) and rejecting any events with multiple S1-like peaks or where the S2 signal is less than 20 photoelectrons. Figure 5.10-*top*, shows the signal induced by ^{22}Na averaged over all 19 PMTs. This is the typical ^{22}Na energy spectrum, where the photoelectric and escape peaks as well as the Compton edge are clearly visible along with the Xe X-ray peaks. Events

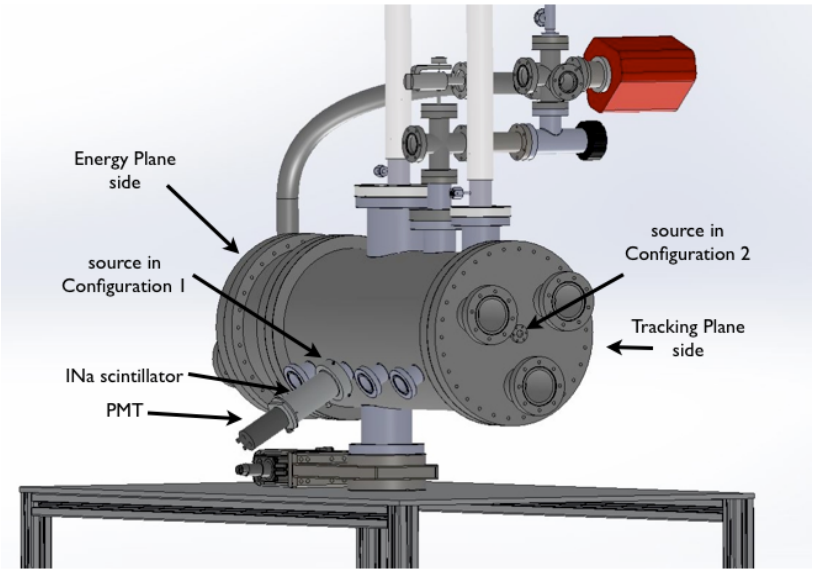

Figure 5.9: Schematic of NEXT-DEMO showing the different source positions for the data taking.

with energy within 1 sigma of the most prominent X-ray peak (K_α) are considered to be due to the interaction of these X-rays and constitute the basic dataset for the subsequent analyses (Figure 5.10-*bottom*). The purity of X-ray events in this initial selection is high in such a way that less than 5% within this range are not X-ray events, corresponding to the extrapolation of the low energy distribution of the Compton effect (flat region in Figure 5.10-*bottom*).

5.4 Monte Carlo Data Generation

A set of Monte Carlo end-to-end simulated events of the same type of data has been used throughout this analysis, both as a tool for reconstruction and as a check of the correctness of the methods. A detailed simulation of the NEXT-DEMO prototype has been developed

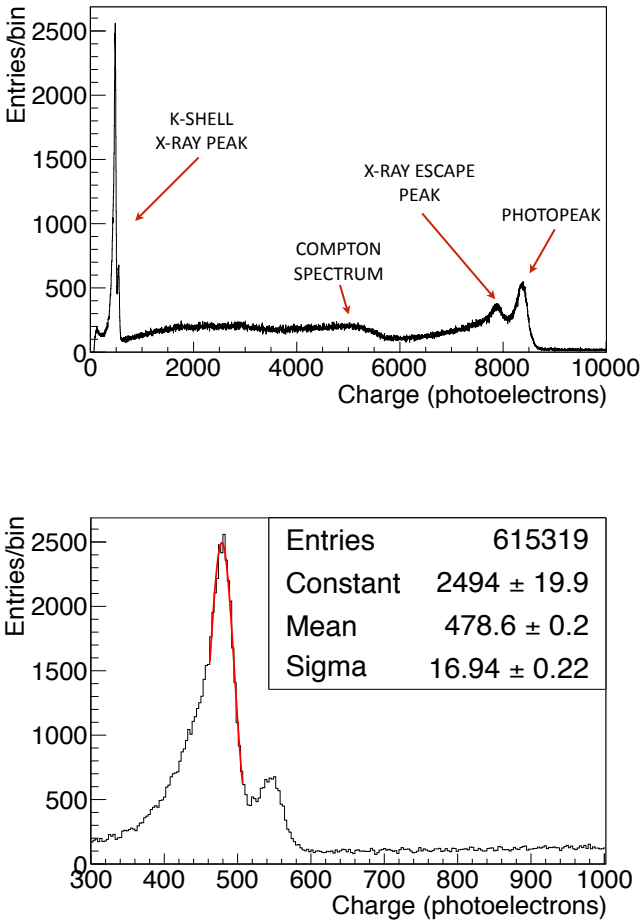

Figure 5.10: Top: Energy spectrum of the ^{22}Na source before any correction. Bottom: Gaussian fit to X-ray peak for X-ray event selection.

in NEXUS [45], the Geant4-based [119, 120] simulation software of the NEXT collaboration. This Monte Carlo dataset was generated simulating the two 511 keV back-to-back gammas coming from the annihilation of the positron emitted in the decay of a ^{22}Na nucleus. Such particles are generated in the place where the radioactive source is located in NEXT-DEMO and are propagated through the materials of the detector, where all the relevant processes are taken into account. The ionization electrons resulting from the interaction with the gas are drifted through the active region and, when they enter the electroluminescent region, a secondary scintillation signal is simulated, according to previously produced lookup tables, which give the response of the sensors (both PMTs and SiPMs) to the electroluminescent light generated in a particular point of the EL region. The response of the sensors, in photoelectrons, is digitized, adding fluctuations in the gain, electronic noise, and shaping according to measurements taken in NEXT-DEMO.

5.5 Position Reconstruction

Spatial reconstruction of the deposited energy in the detector is performed using the S2 signal recorded by the tracking plane. The position is determined using the barycentre of the deposited charge. A preselection of the useful channels is made considering the relative charge compared to that of the maximum channel. As can be seen in Figure 5.11, the charge observed in each channel tends to decrease asymptotically to a level of 10%. Taking this as the noise baseline, the barycentre $(\overline{x}, \overline{y})$ is calculated using only those channels with charge greater than 10% of that of the channel with greatest charge according to

$$\overline{x} = \frac{1}{Q_{tot}} \sum_{i=0}^{n} x_i \cdot Q_i \quad ; \quad \overline{y} = \frac{1}{Q_{tot}} \sum_{i=0}^{n} y_i \cdot Q_i \tag{5.5}$$

where $x_i(y_i), Q_i$ are position and charge respectively of each SiPM and $Q_{tot} = \sum_{i=0}^{n} Q_i$.

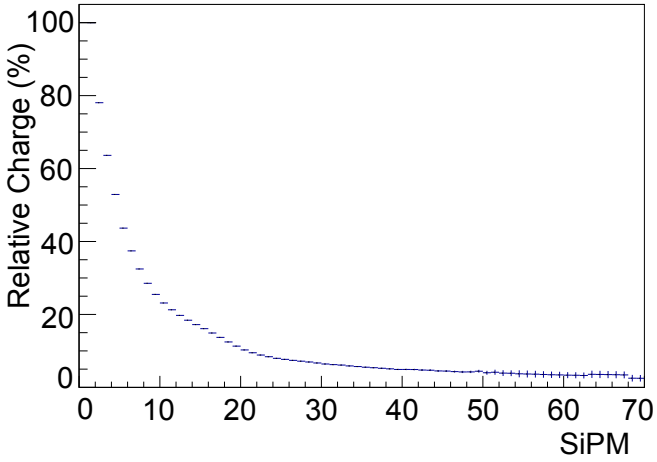

Figure 5.11: Relative charge to maximum signal in the tracking plane. The plot shows how relative charge decreases until an asymptotic value of 10% of the maximum charge.

This assumption has been checked using NEXUS under the same conditions. The barycentre is calculated as described above using the SiPM channels with charge greater than 10% that of the SiPM with maximum charge, and then compared to the averaged position of the energy deposits recorded by Geant4. Figure 5.12 shows the distribution on the reconstructed position where R_{true} is the true position of events given by MC and R_{reco} is the calculated position. In the data the statistics reduce significantly at $R_{reco} > 60$ mm because the trigger conditions favor the events in the center of the detector volume. For this reason the fiducial region is defined by this value. As can be seen in Figure 5.12, the position is reconstructed accurately within this region.

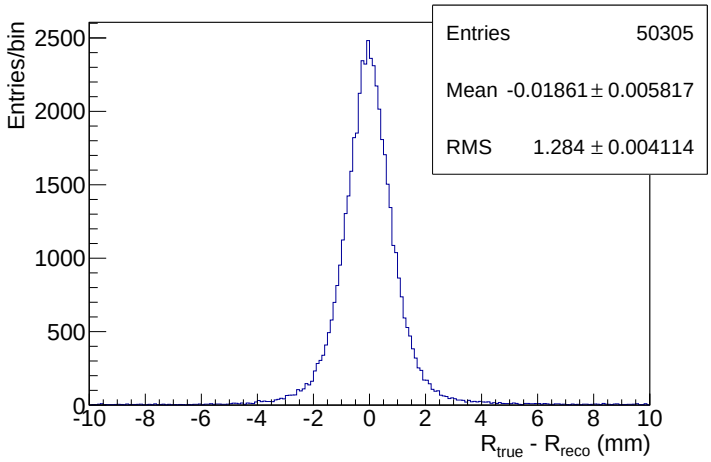

Figure 5.12: Distribution of the reconstructed position. R_{true} is the true position of events given by MC and R_{reco} is the calculated position.

5.6 Properties of Xenon EL-based TPC

As explained in Chapter 3, an EL TPC has huge potential in the field of $\beta\beta0\nu$ physics. Good energy resolution can be achieved and track reconstruction can be used to reduce backgrounds. However, achieving the optimum performance requires a deep understanding of the detector response so that inhomogeneities in energy reconstruction and blurring of the event topology do not reduce sensitivity. The point-like nature of X-ray induced events means that they can be used to monitor fundamental properties of the gas and detector.

Of particular interest are the properties of the EL gap. Since electrons continuously produce light as they pass between gate and anode, a point-like deposition will be smeared out in three dimensions at the read-out plane. These effects are convoluted with the diffusion of the charge cloud during drift, which can also be studied, along with the drift velocity, using the K_α X-ray deposits.

5.6.1 Drift Velocity

Electron drift velocity (v_d) can be determined analyzing the longitudinal event time distribution in the TPC. The drift time (t_d) is well defined by the difference in detection time between the S1 and S2 signals in the events selected as X-ray. There exists a maximum drift time (t_{dmax}) corresponding to the events just inside the drift region next to the cathode. This maximum can be determined as the half-maximum of a Heaviside function fitted to the event time distribution (shown in Figure 5.13-*top*). The maximum drift distance can be calculated from the detector design parameters as the total drift distance plus half of the width of the EL region, since the peak of light production is well estimated by that point. In NEXT-DEMO, these values are 300 mm and 2.5 mm respectively (see § 3.7).

Drift velocity is lower in the drift region than in EL region, however, due to the smallness of the last, we assume this difference negligible compared to the total drift distance. The drift velocity can be then calculated from the ratio between the maximum drift distance D_{dmax} and the maximum drift time t_{dmax}:

$$v_d = \frac{D_{dmax}}{t_{dmax}} = \frac{300 + (5/2)\ \text{mm}}{t_{dmax}} \tag{5.6}$$

Configuration 1 data were used to determine the drift velocity in order to maximise the number of events near the cathode. The drift velocity was determined for 4 drift field settings (0.5, 0.4, 0.3, 0.2 kV cm^{-1}). The results are shown in Figure 5.13-*bottom*, where they are compared to the expectation using electron scattering cross-sections for xenon at 10 bar obtained with the Magboltz 9.0.2 simulation code [121]. The difference between data and simulation may be due to the presence in the gas of xenon clusters, although not being stable, reduce the gas mix density increasing the electron drift velocity as well as the uncertainties in the cross sections used by the simulated

model. These results are in agreement with previous data obtained by the *NEXT Collaboration* as published in [122, 123].

5.6.2 Longitudinal Spread

A point-like charge deposit will tend to be read with a finite width in the longitudinal direction due to two main effects: the EL gap induced spread and the longitudinal diffusion. The former, due to EL light, is not produced in a single z point, but over the whole distance between gate and anode. Both effects contribute to the observed signal z sigma in the following way:

$$\sigma_t = \sqrt{{\sigma_L}^2 + {S_L}^2} \tag{5.7}$$

where σ_t is the sigma in z of the signal, σ_L is the sigma of the spread induced by longitudinal diffusion, and S_L is the EL gap induced longitudinal spread (all units in seconds). The longitudinal diffusion term σ_L is defined as:

$$\sigma_L^2 = (\frac{2D_L}{v_d^3}) \cdot z \tag{5.8}$$

where D_L is the longitudinal diffusion coefficient (in units of $[cm^2\ s^{-1}]$), v_d is the electron drift velocity, and z is the drift length.

5.6.2.1 EL Gap Induced Longitudinal Spread

Using *Configuration 2* data to maximize the number of events at small drift lengths and selecting X-ray deposits using the additional requirement of Gaussian form of the S2 in the z direction, S_L can be studied. Events with drift times (t_d) of less than 50 μs had their time charge distributions fitted, (Figure 5.14-*top*), and those events not successfully fitted by this model were rejected. The number of rejected events is compatible with the number of non X-ray events present in the initial selection made on § 5.3.

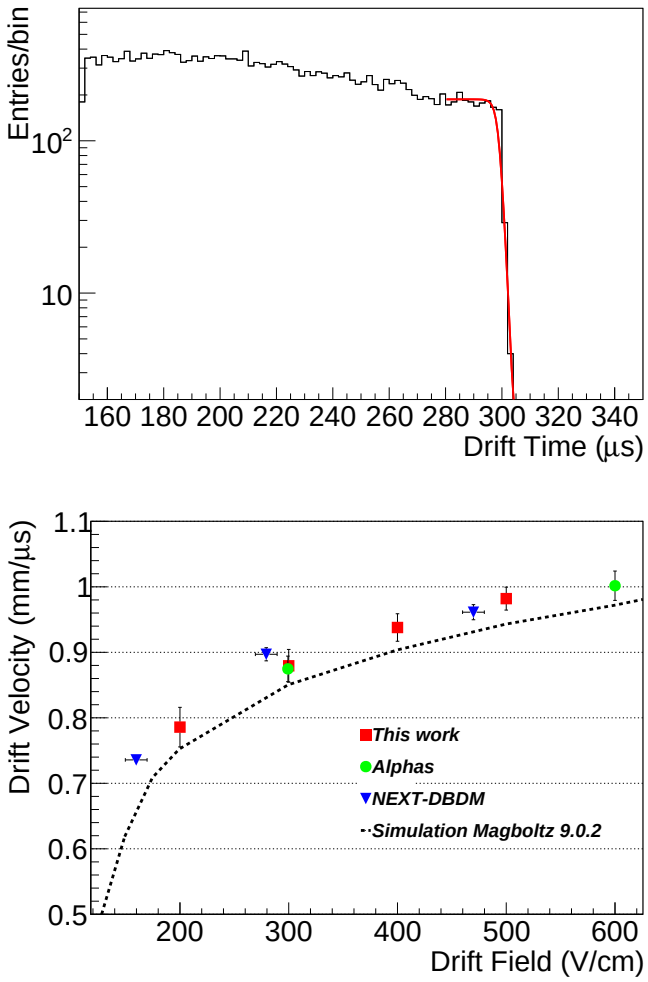

Figure 5.13: Top: Event time distribution for 0.5 kV cm^{-1} drift field, and its fit to the Heaviside function. Bottom: Drift velocity as a function of drift field, for xenon gas at 10 bar. The red square points are the measured values, green circles correspond to the results of [123], blue triangles are from [122] while the dashed curve is the prediction for pure xenon at 10 bar from the Magboltz 9.0.2 simulation [121].

Using equations 5.7 and 5.8 it can be seen that there exists a linear relationship between the variance of the signal in z and the drift time with the intercept equal to the square of S_L:

$$\sigma_t^2 = \frac{2D_L}{v_d^2} t_d + {S_L}^2 \tag{5.9}$$

where for a given drift field and gas conditions the longitudinal drift coefficient and drift velocity, and hence their ratio, are constant. Therefore, fitting this model to the distribution obtained using the selection mentioned above allows for a determination of S_L. For the standard drift field settings (2 kV cm^{-1} bar) this method yields a value of $S_L = 0.50 \pm 0.05$ μs. This result is slightly different to the value obtained in [123], $S_L = 0.8$ μs, presumably because of the different drift field in the EL region (1 kV cm^{-1} bar). At higher fields, a higher drift velocity reduces the drift time across the EL gap of the electrons. Another implication of this value is the minimum expected duration in z of an event. A sigma of 0.5 μs implies that ~99.7% of the charge would be contained within 6σ and, as such, we would expect a minimum z width of ~3 μs, a value which includes the shaping of the electronics.

5.6.2.2 **Longitudinal Diffusion**

Using the same method of the previous section and extending the allowed drift time, the longitudinal diffusion coefficient can be determined by a fit to the z sigma versus the drift length using the model of equation 5.7 and the calculated drift velocity from § 5.6.1 and S_L from § 5.6.2.1.

The model is shown in Figure 5.15-*top* for a drift field of 0.5 kV cm^{-1}. This coefficient was determined for the same drift field settings used for drift velocity studies of § 5.6.1 and once again compared to a pure xenon simulation based on version 9.0.2 of Magboltz (Figure 5.15-*bottom*). These results are in slight disagreement with previous data

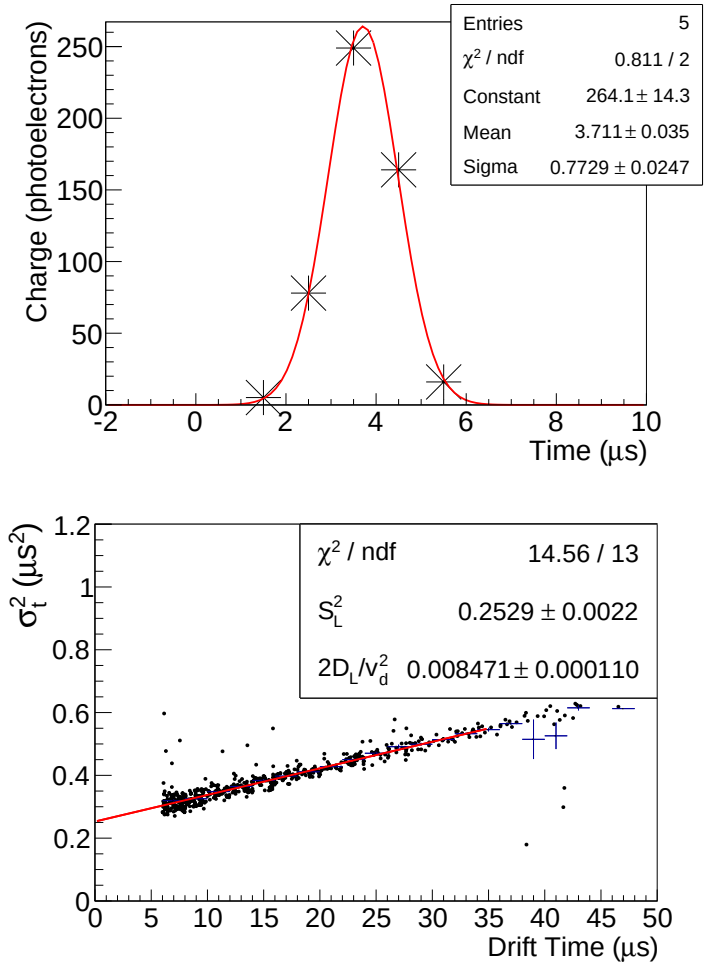

Figure 5.14: Top: Temporal charge distribution of a typical X-ray event and Gaussian fit. Bottom: Variance of the Gaussian fits versus drift time t_d, and linear fit to the model obtaining S_L^2 as the intercept.

obtained by the *NEXT Collaboration* [122, 123], where somewhat lower values were extracted. The differences with simulation and previous results are not fully understood at present. They could be attributed to differences, perhaps, in gas conditions during data taking.

5.6.3 **Transverse Spread**

The transverse response of the tracking plane to a point-like charge deposition is expected to have a width distribution due to the convolution of the transversal diffusion and the EL gap induced Transverse Spread S_T. The ionization electrons will diffuse transversely as they drift up to the EL region. Once there, due to the isotropic emission of light, each electron will be seen as the projection of a cone, and therefore, a K_α deposit will be seen as multiple overlapping cones.

Using the events selected as X-ray using the criterion mentioned above, a study of the extent of this projection was carried out. Figure 5.16-*top* shows the average projection of an event onto the x-y plane with the channel with maximum charge taken as the centre and the charge of the neighboring channels plotted according to their distance from it. A two dimensional Gaussian can be fitted to the distribution to give an estimate of the transverse spread of the charge.

Figure 5.16-*bottom* shows the standard deviation of the two dimensional fit as well as their quadratic sum which is the parameter used to define the EL gap induced transverse spread ($S_T = \sqrt{{\sigma_x}^2 + {\sigma_y}^2}$), plotted versus drift time. There is no significant dependence of the measured values with drift time suggesting that the EL gap distortion dominates the transverse spread of the charge cloud in the detector. The pitch of the SiPM channels in NEXT-DEMO is 10 mm, S_T of the order of 8 mm suggests that little would be gained by increasing sensor density, as commented in § 3.5.5.

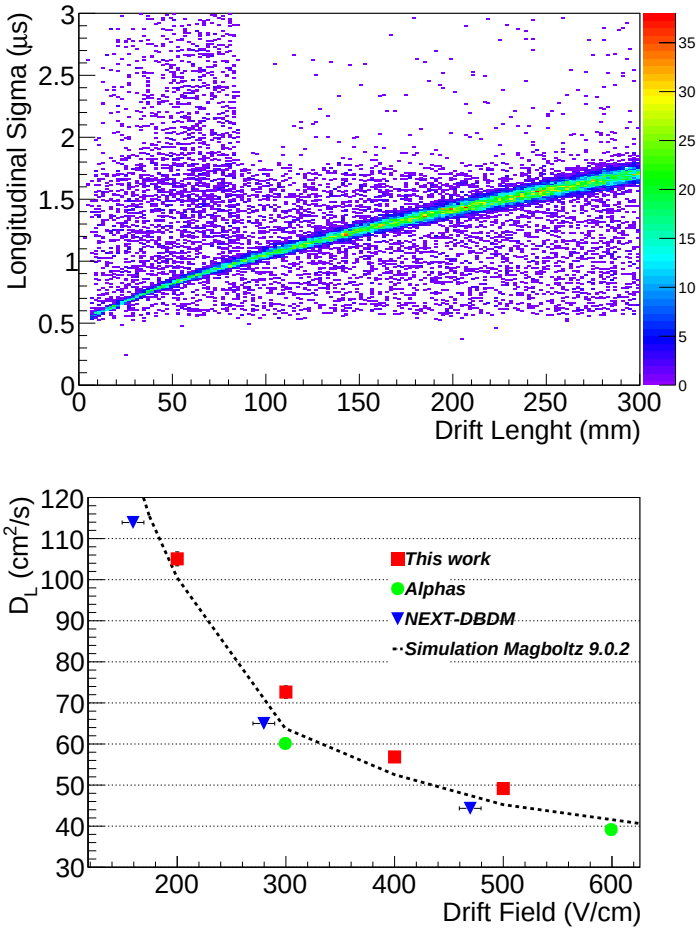

Figure 5.15: Top: Longitudinal sigma of the temporal charge distribution fits versus drift length for the 0.5 kV drift field configuration dataset. Bottom: Longitudinal diffusion coefficient D_L as a function of drift field for xenon gas at 10 bar. The red square points are the measured values, green circles correspond to the results of [123], blue triangles are from [122] while the dashed curve is the prediction for pure xenon at 10 bar from the Magboltz 9.0.2 simulation [121].

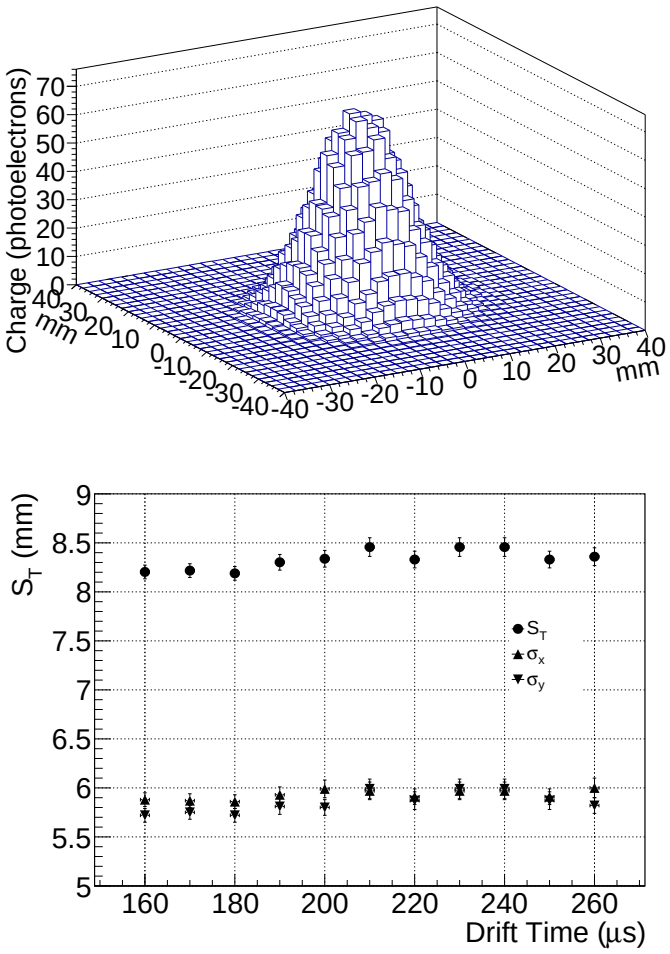

Figure 5.16: Top: Average 3D charge distribution of a X-ray event from its barycenter. Bottom: S_T, σ_x and σ_y of charge distribution gaussian fit versus Drift Time.

5.7 Energy Resolution

One of the most important goals of NEXT-DEMO is to prove that the energy of electron tracks can be reconstructed accurately, and that the resolution calculated for these tracks can be extrapolated to less than 1% FWHM at $Q_{\beta\beta}$ (the target value in NEXT-100 [60]). While the energy resolution of the raw data, only considering the online trigger, is already good, there are a number of correctable detector effects which can be understood and equalised, optimizing the energy resolution of the detector. Among these effects are attachment during drift, which causes a drift distance dependant energy measurement and inhomogeneities in light production and reflection due to the grids and light tube. Similarly as was done in § 5.6, these effects can be understood using the K_α X-ray events which can be used to equalise the detectors response.

5.7.1 Electron Attachment

As commented in § 3.1, during the charge cloud's drift towards the anode, a fraction of the charge is lost due to attachment. Attachment is reduced by constant circulation and cleaning of the gas through hot getters but there remains a small, observable effect. Using the K_α peak in the selected data and plotting its charge versus drift time this decay can be seen (Figure 5.17) and modeled as an exponential function

$$N(t_d) = N(0) \cdot \exp(-t_d/\tau) \tag{5.10}$$

where N represents the mean charge measured, which is a function of the drift time t_d, and τ the mean electron lifetime in the gas. Using this value the loss of charge due to attachment can be effectively corrected.

In all datasets considered in this work, the decay constant was measured to be -3.5×10^{-5} μs^{-1}, equivalent to a mean electron lifetime of ∼28 ms, far larger than the maximum drift time of the TPC. This value represents an improvement over the values achieved in other gaseous xenon detectors [124].

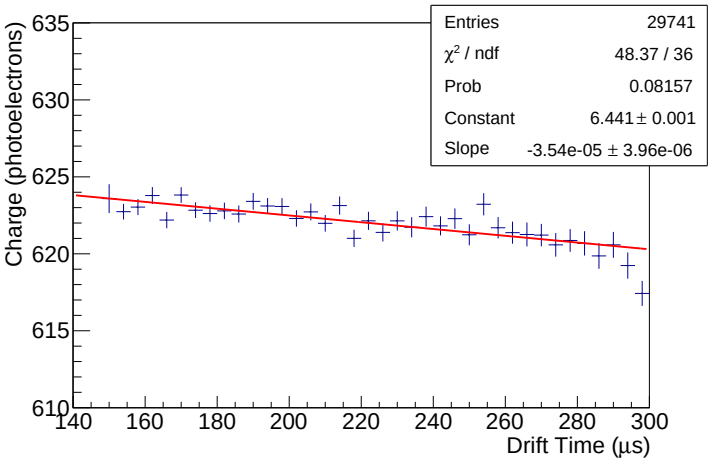

Figure 5.17: Mean charge of X-ray events versus drift time. Exponential fit is made and decay constant extracted.

5.7.2 Time-related Fluctuations

Temperature variations due to the gas recirculation as well as air conditioning activity in the laboratory, produce a variation in the sensors response. The effect over the *tracking plane* was corrected by the active control of the gain described in § 4.6, while the effect over the energy plane is insignificant due to small dependence of PMTs to temperature changes. However, temperature variations cause pressure variations in the gas xenon present inside NEXT-DEMO, and therefore, according to equation 3.9, a change in the absolute Electroluminescense gain, η. In addition, continuous exposure to VUV light can damage the photocathode of the PMTs as well as the TPB layer with which the inner face of the light tube is coated, reducing the effective response measured with the energy plane.

All these effects can be observed as a time-dependent decrease of

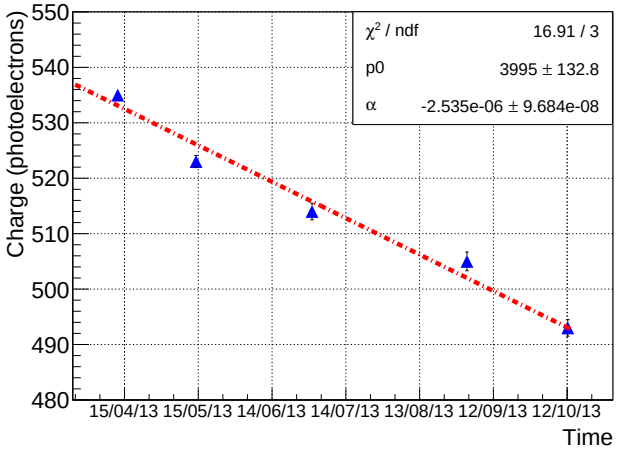

Figure 5.18: Mean charge of X-ray events versus time in a range of six months.

the detected K_α X-ray charge. Figure 5.18 shows the mean position in charge of the K_α peak over a period of 6 months. As can be seen, there is a degradation of the charge with time, which can be modeled as

$$N(t) = N(0) + \alpha \cdot t \tag{5.11}$$

where N represents the mean charge measured, produced by the K_α deposition and α is the slope of this degradation, parameterized as linearly dependent on time. The slope was determined to be a fraction lost of charge of ~0.06% per day. Using this value, the temporal reduction of the measured charge can be effectively corrected.

5.7.3 XY Response

The measurement of the energy of the events is affected by a number of processes in the detector. Those corresponding to temporal reduction

and electron attachment have been described and corrected in the previous sections, and can be considered uncorrelated with the rest. However, due to the imperfect rotational symmetry of the light tube and variation in the amount of deposited TPB across the detector, the stronger effect when measuring the energy of the events is the XY position where the event occurs.

To understand the spatial behavior of the light tube, the response of the detector to the K_α X-rays was analyzed in bins of 1 cm^2. In each bin, the individual response of each PMT to these singular events was stored, and their distributions fitted to a Gaussian extracting the mean and sigma values (examples in Figure 5.19). Using the mean position of the K_α deposits, a correction factor per PMT i and bin x, y ($f_i(x, y)$) is determined by normalizing the mean value to the central bin.

The correction factors for an individual PMT are represented by white points in Figure 5.20. However, the resolution of the grid can be improved using a Delaunay triangulation [125] between the bins, increasing the number of factors by 2 orders of magnitude (color map in Figure 5.20).

In addition, the variance of each distribution (σ^2) can be used as estimator of the good behavior of the PMT i in the bin x, y. This variance will be used in the next section when calculating the contribution of the PMT i to the sum of the energy plane.

5.7.4 Calculation of Energy Weighted Sum

The correction factor determined above together with those obtained in § 5.7.1 and § 5.7.2 can, in principle, be used as a model for the correction of the energy of any type of interaction in the TPC. While an extended event will require consideration in time slices, the photoelectric events of ^{22}Na and ^{137}Cs are still small enough that the X-ray model is a good one.

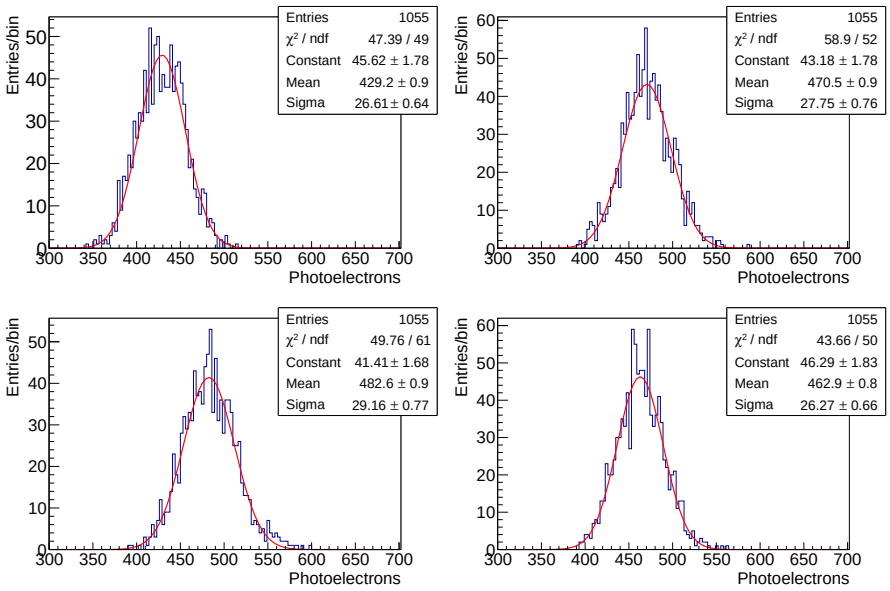

Figure 5.19: Distribution of response to K_α events of a PMT in four bin x, y and gaussian fits to calculate correction factors.

The corrected event energy is calculated as the weighted sum of the contributions from each individual PMT:

$$Q_{tot} = S_0(x,y) \cdot \sum_i q_i \cdot w_i(x,y) \cdot f_i(x,y) \tag{5.12}$$

where q_i is the charge recorded by PMT i, $w_i(x,y)$ its weight for the reconstructed (x,y) position — here, the inverse of the variance of its response to K_α X-rays as described in § 5.7.3 — and $f_i(x,y)$ is the geometrical correction factor for PMT i in for the reconstructed (x,y) position. The term $S_0(x,y)$ is an overall conversion factor from photoelectrons to energy. Using this weighted energy estimator, inhomogeneities in the response of the PMTs are taking into account.

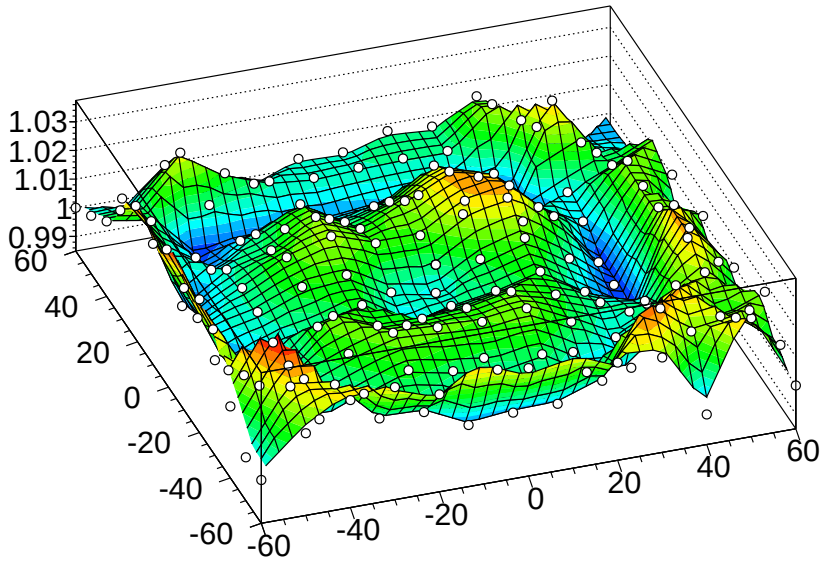

Figure 5.20: Calculated correction factors (white points) versus their x,y position. Delaunay interpolation is represented in color, increasing the number of points by 2 orders of magnitude.

The errors associated to the method employed produce a slight difference in the energy scale according to the (x, y) bin in which an event falls. This is accounted for by calculating a scaling factor per bin, $S_0(x, y)$. These factors are calculated by fitting a straight line, in each bin, to the known energy of well defined peaks (the K_α and K_β peaks at 29.7 keV and 33.8 keV respectively) and the photoelectric peak and its escape peak, at 511 keV and ~481 keV for ^{22}Na and 661.7 keV and ~641 keV for ^{137}Cs (example in Figure 5.21).

Applying all the corrections described, the resultant ^{22}Na spectrum is that shown in Figure 5.22-*top* with energy resolution for the K_α peak

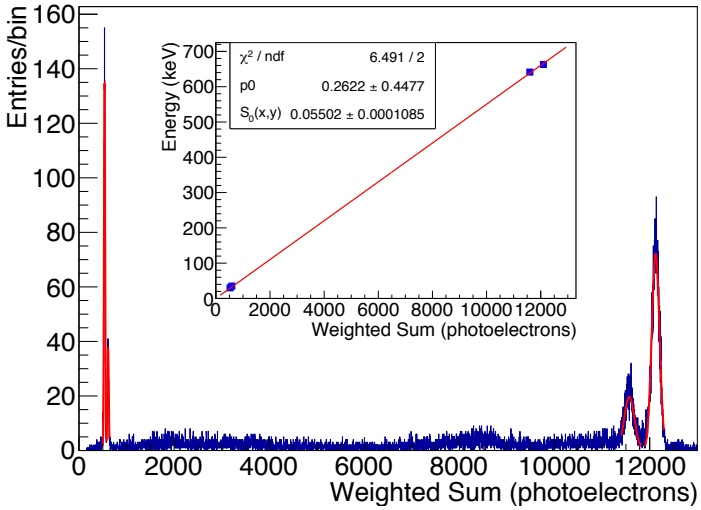

Figure 5.21: Spectrum of an individual bin x,y to extract $S_0(x,y)$ for equation 5.12.

of (5.691 ± 0.003)% FWHM (detail shown in Figure 5.22-*center*). The ^{22}Na photopeak has a resolution of (1.62 ± 0.01)% FWHM (detail shown in Figure 5.22-*bottom*).

Using same corrections, the resultant ^{137}Cs spectrum is shown in Figure 5.23-*top*, with energy resolution for the K_α peak of (5.416 ± 0.002)% FWHM (detail shown in Figure 5.23-*center*). The ^{137}Cs photo peak has a resolution of (1.51 ± 0.01)% FWHM (detail shown in Figure 5.23-*bottom*).

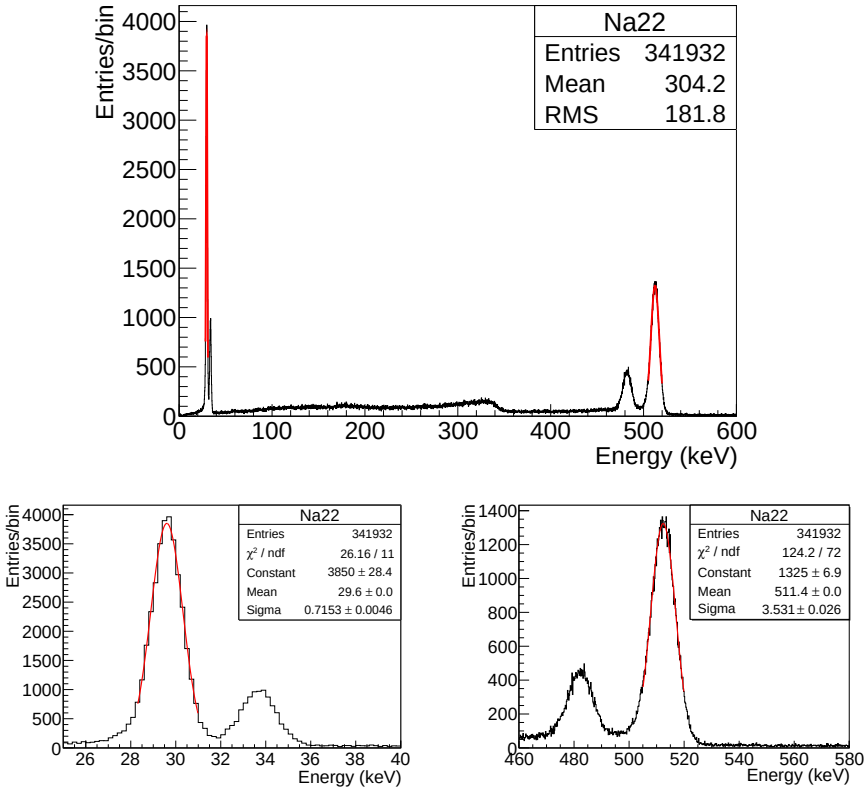

Figure 5.22: Top: ^{22}Na spectrum after all corrections. Bottom-left: Zoom of X-ray peak region and gaussian fit of the K_α peak. Bottom-right: Zoom of the escape and photoelectric peaks and gaussian fit to the Photoelectric.

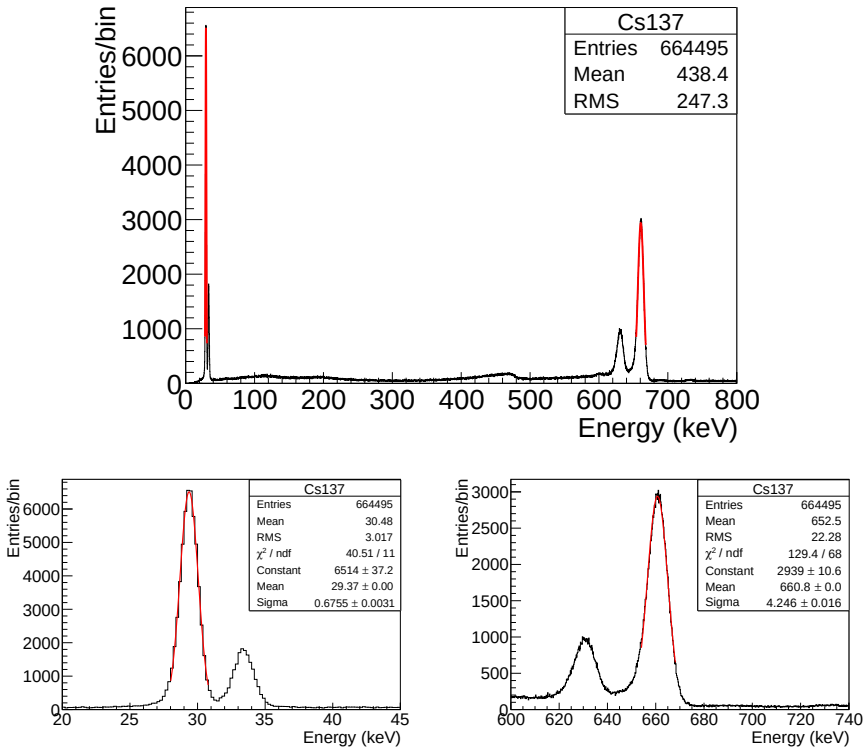

Figure 5.23: Top: ^{137}Cs spectrum after all corrections. Bottom-left: Zoom of X-ray peak region and gaussian fit of the K_α peak. Bottom-right: Zoom of the escape and photoelectric peaks and gaussian fit to the Photoelectric.

5.7.5 Extrapolation to Higher Energies

As already discussed in § 2.5.2, an excellent energy resolution at $Q_{\beta\beta}$ value is needed in all $\beta\beta0\nu$ experiments, in order to resolve the energy released by neutrinoless events from background events, either high energy gammas coming from natural sources or the two neutrino mode.

With the obtained values of energy resolution from the previous section (see Table 5.1), an extrapolation model for the energy resolution (ER) can be constructed as

$$ER \propto A + \frac{B}{\sqrt{E}} \tag{5.13}$$

where A represents the fluctuations associated to instrumental effects (noise, calibration errors, non-uniformity in sensors, ...) and B represents the photon shot noise Poisson statistics. For the extracted parameters (see Figure 5.24), the extrapolated value of energy resolution to the ^{136}Xe $Q_{\beta\beta}$ is (0.96 ± 0.03)% FWHM. This value, which already shows a slight improvement over the target energy resolution of the NEXT experiment, is limited by the model described by equation 5.13, since this model presents a gradual breakdown at high energies due to the increased size of the tracks. To solve this, a single correction per track's slice must be done, taking as slice the total size of an X-ray event. This assumption would improve the energy resolution of the NEXT-DEMO detector until the value predicted by simulations, achieving the limit set by the Fano factor, 0.37% FWHM at $Q_{\beta\beta}$ value.

Source	Energy (keV)	ER (% FWHM)	ER@$Q_{\beta\beta}$ (% FWHM)
^{22}Na	29.7	5.691 ± 0.003	0.626 ± 0.003
^{22}Na	511	1.62 ± 0.01	0.73 ± 0.05
^{137}Cs	29.7	5.416 ± 0.002	0.596 ± 0.002
^{137}Cs	661.7	1.51 ± 0.01	0.78 ± 0.06

Table 5.1: Energy Resolution obtained with the Energy Weighted Sum method for ^{22}Na and ^{137}Cs sources, and independent extrapolation to the $Q_{\beta\beta}$ value of ^{136}Xe assuming a $1/\sqrt{E}$ dependence.

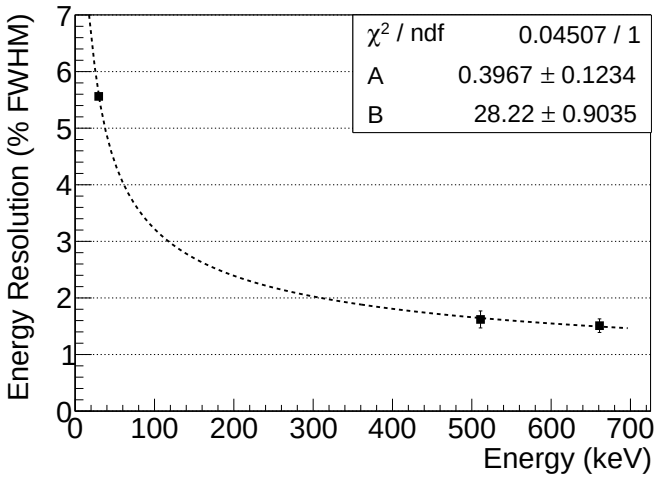

Figure 5.24: Energy resolution achieved in NEXT-DEMO as a function of energy and fit to equation 5.13.

Science never solves a problem without creating ten more.

George Bernard Shaw

CHAPTER

6

Summary and Conclusions

In recent decades, various experiments announced the observation of neutrino flavour oscillation. This phenomenon can only be explained assuming that neutrinos are massive particles, in contradiction with their description in the Standard Model of Particle Physics, providing the first evidence of physics beyond the current Standard Model (§ 2.1).

At present, there is the theoretical prejudice that neutrinos must be Majorana particles, that is, identical to their antiparticles, since a Majorana mass term explains naturally the smallness of neutrino masses (§ 2.3 and § 2.4). The only experimental method which can effectively confirm this idea is the observation of neutrinoless double beta decay, since for this process to be observable, the anti-neutrino generated in one vertex of the beta decay must interact as neutrino

in the opposite vertex, being only possible if both particles are the same (§ 2.5).

The Neutrino Experiment with a Xenon TPC (NEXT), is one of the experiments that plans to search for neutrinoless double beta decay of ^{136}Xe. In this work, a detailed description of the physical processes involved in the detection of $\beta\beta0\nu$ events in the NEXT-100 detector has been done (§ 3.1), emphasizing its advantages over other detection techniques, as the low fluctuations introduced by an EL amplification system (§ 3.1), which results in an extremely good energy resolution at the $Q_{\beta\beta}$ value of xenon, below 1% FWHM (§ 3.2). This property, together with the capability of reconstructing the tracks of particles (§ 3.3), only possible in high pressure gas, make of the NEXT-100 detector a promising candidate in the $\beta\beta0\nu$ field.

In this thesis we also have presented a scale-down prototype of the NEXT-100 detector, the NEXT-DEMO prototype (§ 3.7), built to demonstrate the feasibility of the proposed technology. A detailed description of the prototype's tracking plane has been done (§ 4.2), justifying the choices made in its design. At the same time, an intensive study over the dynamic properties of the SiPMs used in the tracking plane were carried out, characterizing the response of these sensors and ensuring their suitability for NEXT (§ 4.2.9). It is shown in particular that the response of the SiPMs is uniform over the tracking area with a gain dispersion of less than 3.6% (§ 4.4). The gain of the SiPMs is stabilized against temperature changes using an automated bias voltage compensation system, which ensures less than 0.5% gain variation in a temperature range of 10°C (§ 4.6).

In order to resolve the low photon detection efficiency of SiPMs to the xenon scintillation light, an strict coating protocol has been developed (§ 4.3), with particular precautions in obtaining clean and uniform coatings, with optimal fluorescence efficiency, choosing a deposition thickness of 0.1 mg/cm^2. The characterization of the coated

samples with different UV light sources shows high quality TPB coatings on the SiPMs of the NEXT-DEMO tracking plane. Furthermore, the coated SiPMs show a significant and uniform response to the Xe scintillation wavelength compared to the non-coated ones, observing an increase of a factor eight in the UV range from 250-315 nm (§ 4.3.3).

This thesis also describes the installation (§ 4.7), commissioning of the plane and calibration methods (§ 5.1) used for the analysis of the sensor's response, solving the initial problem created by the presence of electromagnetic noise inside the detector, which made it impossible to apply the conventional calibration method

In the final part of this work, NEXT-DEMO data have been used to present the flexibility of xenon X-ray events both as a means to understand the fundamental properties of the TPC and as a model for the equalization of detector energetic response (§ 5.2). The drift velocity and diffusion of the TPC have been determined using these events, which are abundant in any type of data taking (§ 5.6). These properties can be used to monitor the gas quality of the detector and to understand the effect of the EL gap on the observed signals. The same events have also been used to understand inhomogeneities in the detector response allowing for a normalization of effects due to uneven deposition of wavelength shifter and asymmetries in the form of the light tube (§ 5.7). This model has been used to calculate a corrected weighted sum of the observed energy resulting in ^{22}Na and ^{137}Cs photopeak energy resolution of 1.62% and 1.51% FWHM respectively, which translates into a resolution of 0.96% FWHM at the $Q_{\beta\beta}$ value of ^{136}Xe assuming a $1/\sqrt{E}$ dependence.

List of Figures

2.1 Particle content of the Standard Model. Notice the mass scale of neutrinos compared with that of other fundamental particles. Reproduced from [10]. 7

2.2 Representation of the two possible neutrino mass orderings. Left corresponds to the *"normal"* ordering, where m_1 is the lightest neutrino mass eigenstate, while right is the *"inverted"* ordering, if m_3 is the lightest eigenstate. . 11

2.3 Energy spectrum of beta decay showing the endpoint region. The black line corresponds to zero neutrino mass and the red line to finite neutrino mass. 13

2.4 Atomic masses of isotopes with $A = 136$ given as differences with respect to the most bound isotope, ^{136}Ba. The red levels indicate odd-odd nuclides, whereas the green indicate even-even ones. The arrows show the type of nuclear transition connecting the levels. Double beta (either plus or minus) transitions are possible because the intermediate state ($\Delta Z = \pm 1$) is less bound, forbidding the beta decay [45]. 18

2.5 Feynman diagram for the $\beta\beta 2\nu$ (left) and the $\beta\beta 0\nu$ (right). 19

2.6 Effective neutrino Majorana mass, $m_{\beta\beta}$, as a function of the lightest neutrino mass, m_{light}. The green band corresponds to the *inverse* hierarchy of neutrino masses, whereas the red corresponds to the *normal* ordering. The upper bound on the lightest neutrino mass comes from cosmological bounds whereas the bound on the *effective Majorana mass* from $\beta\beta0\nu$ constraints. 25

3.1 Principle of Electroluminescense generation process. . . 32
3.2 Reduced scintillation yield (open squares represent Monte Carlo results, while filled circles experimental results) and detector energy resolution (open circles) as a function of reduced electric field in the scintillation region for $5.9\,keV$ X-rays. The experimental values are normalized to the calculated Monte Carlo values at $\bar{E}/p = 6$ V cm^{-1} torr^{-1}, (4.5 kV cm^{-1} bar^{-1}) (from [64]). 33
3.3 Energy resolution (% FWHM) of ^{137}Cs 662 keV γ-ray, as a function of xenon density for the ionization signal only, reproduced from[72]. 35
3.4 Monte Carlo simulation of the topological signature of a $\beta\beta0\nu$ event in NEXT, a track that ends in two "blobs" of energy. The trajectory of electrons are dominated by multiple scattering in the dense gaseous xenon [45]. . . 38
3.5 Energy spectra of signal (red, solid curve) and background (^{208}Tl: grey, dashed distribution; ^{214}Bi: grey, dotted distribution; total: grey, solid distribution) in the region of interest (ROI) around $Q_{\beta\beta}$. The signal strength represented here corresponds to a neutrino Majorana mass of 200 meV, while the backgrounds are scaled to their expected values in NEXT-100 (6×10^{-4} counts/(keV$\cdot$ kg$\cdot$y)), assuming an exposure of 91 kg yr [45]. 40

3.6 The Separated, Optimized Functions TPC (SOFT) concept. EL light generated at the anode is recorded in the photosensor plane right behind it and used for tracking. It is also recorded in the photosensor plane behind the transparent cathode and used for a precise energy measurement. 41
3.7 Cross-section view of the NEXT-100 detector inside its lead castle shield. A stainless-steel pressure vessel (A) houses the electric-field cage (D) and the two sensor planes (energy plane, E, and tracking plane, C) located at opposite ends of the chamber. The active volume is shielded from external radiation by at least 12 cm of copper (B) in all directions [45]. 43
3.8 Scheme of DAQ and Online for NEXT-100. 51
3.9 Drawing of the NEXT-100 detector and the lead castle shield (in open position). Both the detector and shield rest on an anti-seismic platform. 52
3.10 Sensitivity (at 90% CL) of NEXT-100 to neutrinoless double beta decay. The solid curve represents the half-life sensitivity, while the dashed curves correspond to the $m_{\beta\beta}$ sensitivity for three different NME calculations (from bottom to top: EDF [86], IBM-2 [85], ISM [87]. . . 54
3.11 The NEXT-DEMO detector and ancillary systems (gas system, front-end electronics and DAQ) at IFIC [5]. . . . 56
3.12 Left: External view of the time projection chamber approximately indicating the different regions. Right: Hexagonal light tube of NEXT-DEMO illuminated with a UV lamp after being coated with TPB [5]. 57

4.1 Scheme of the energy-band structure of (a) an insulator, (b) a semiconductor, and (c) a conductor. 61

4.2 Covalent bonding of silicon. Left: Addition of pentavalent impurity (donor) forming n-type silicon. Right: Addition of tetravalent impurities (acceptor) forming p-type silicon. 63
4.3 Scheme of the pn-junction model. Depletion zone and charge are only qualitative. Bottom symbol commonly used for a diode. 64
4.4 Left: Detail of the pixel array structure of a SiPM. Right: SiPM from Hamamatsu photonics. 66
4.5 Schematics of the electrical model of the SiPM. The quenching resistance of the pixel is represented by R_q while the pixel capacitance by C_d. 68
4.6 Left: Bias circuit connection example. Right: Pulse waveforms registered in the oscilloscope. The distributions produced by different number of fired pixels in the SiPM are clearly observable. The X axis has a scale of 50 ns/div while the the Y axis 5 mV/div. 69
4.7 Typical single photon spectrum (SPS) of a SiPM obtained with a pulsed LED. Individual photoelectron peaks are identified. The peak on the extreme right corresponds to the charge of the electronics baseline. Subsequent peaks correspond to 1, 2, 3 ... pixels being fired in the SiPM. . 70
4.8 Mean charge produced by different number of fired pixels and linear fit to obtain the SiPM gain. 71
4.9 Sigma square of the charge distribution corresponding to the peaks in Figure 4.7 versus the number of fired pixels. The deviation from the linear trend is illustrated by the dashed line, corresponding to a linear fit to the first 3 data points. 72
4.10 Gain versus operating voltage (left) and overvoltage (right) for a MPPC S10362-11-050P from Hamamatsu Photonics. 73

4.11 Forward Current for a SiPM S10362-11-050C and linear fit to equation 4.6 to obtain the quenching resistance of the pixel. 75
4.12 Dark Count Rate of the S10362-11-050C versus the voltage threshold established. 78
4.13 Dark Count Rate of the S10362-11-050C versus temperature at different overvoltages. 79
4.14 Micro-cells of a SiPM observed with a scanning electron microscope. Photon sensitive areas are delimited by a non sensitive structure. 81
4.15 Measured absorption coefficients for Silicon and Gallium Arsenide, extracted from [99]. 82
4.16 Left: Measured PDE of S10362-11-050P as a function of wavelength in the spectral range 250-315 nm extracted from [100]. Right: Measured PDE (red circles) and PDE values provided by Hamamatsu (black triangles) of S10362-33-050P as a function of wavelength in the spectral range 250-550 nm. 84
4.17 Response curve at 285 nm of S10362-11-050P extracted from [100]. The solid red line represents the linear fit to the data at low illumination levels. The dashed black line represents the theoretical response curve following equation 4.11. 85
4.18 Left: Picture of the glove-chamber filled with N_2 . Right: Picture of the evaporation system containing the crucible used for TPB and the QCM sensor positioned on top of it. 88
4.19 TPB emission spectra obtained from glass plate coated with 0.1 mg/cm^2 of TPB illuminated with 246 nm and 340 nm photons. 91
4.20 Relative standard deviation of current in a SiPM detecting light from different sectors of a coated glass plate as a function of TPB coating thickness. Reproduced from [106]. 93

4.21 Transmittance of the TPB at its emission wavelength as a function of TPB thickness. Reproduced from [106]. . . . 94
4.22 Measured PDE of a coated S10362-11-050P as a function of wavelength in the spectral range 250-315 nm, extracted from [100]. 95
4.23 Response curve at 285 nm of a TPB coated S10362-11-050P, reproduced from [100]. The solid red line represents the linear fit to the data at low illumination levels. The dashed black line represents the theoretical response curve following equation 4.11. 96
4.24 Left: Front view of one Dice Board of the NEXT-DEMO Tracking Plane with 64 SiPMs. Right: Back view of the DB containing the four tantalum capacitors and conector. 97
4.25 TPB-coated Dice Board illuminated with an UV lamp and reemitting in the 430 nm TPB emission peak (blue). 98
4.26 Top: Electronic scheme of one analog path including its three stages. Bottom: View of one front-end (FE) of NEXT-DEMO. 16 FEs are needed to the full read-out of the tracking plane. 100
4.27 Transverse cross section drawing of the experimental setup indicating the main components. 102
4.28 Typical dark count waveform of the S10362-11-050P with a sample time of 1 μs. 103
4.29 Typical dark count spectrum of the S10362-11-050P recorded in a sample time of 1 μs. The gaussian fits to the photoelectrons peak are shown. 104
4.30 Average number of ADC counts produced by different number of fired pixels and linear fit extracting the channel gain. 105
4.31 Gain versus bias voltage for four SiPMs at four different temperatures. 106

4.32 Gain versus temperature for four SiPMs at four constant bias voltages. 107
4.33 Left: Voltage coefficients extracted from the calculated data fitted to equation 4.3. Right: Temperature coefficients extracted from the calculated data fitted to equation 4.3. 108
4.34 Gain of a SiPM without (blue) and with (red) temperature compensation in range from 20 to 30 °C. 109
4.35 Left: Four Dice Boards which comprises the NEXT-DEMO tracking plane. Right: Mounting the tracking plane in the NEXT-DEMO detector. 110
4.36 Histogram with the distribution of the baseline of one electronic channel. The offset is taken as the mean value of the gaussian fit and stored in the database for the posterior subtraction. 111

5.1 Anode-cathode correlation response to a ^{22}Na source using external calibration constants. 115
5.2 Left: Noisy baseline waveform from one electronic channel. Right: Digital SPS of one SiPM where the pickup noise make impossible to resolve photoelectrons. 116
5.3 "Low energy" spectrum of ^{22}Na obtained with one SiPM of the tracking plane, and gaussian fit to the X-ray peak. 117
5.4 Anode-cathode correlation response to a ^{22}Na source after apply the X-ray calibration method. 118
5.5 Top: Photon Transfer Curve of a SiPM and linear fit in the shot noise region obtaining the absolute gain of the system. Bottom: Average response of the SiPM at different illumination levels of the LED and gaussian fit to the mean value. 120

5.6 Left: Baseline distribution of four channels within one Front End without (left) and with (right) normalization by their electronics gains. Gain taken as σ in equation 5.3.122
5.7 Top: Waveform of a biased SiPM with dark count events before (green) and after (red) CNF is applied. Bottom: Single Photon Spectrum obtained with DK events after CNF (left) and linear fit to extract its gain (right). 123
5.8 X-ray emission process. An incoming photon with enough energy extracts an electron from the K, L shells (left). The hole is filled by a more energetic electron with the consequent emission of an X-ray (right). 125
5.9 Schematic of NEXT-DEMO showing the different source positions for the data taking. 126
5.10 Top: Energy spectrum of the ^{22}Na source before any correction. Bottom: Gaussian fit to X-ray peak for X-ray event selection. 127
5.11 Relative charge to maximum signal in the tracking plane. The plot shows how relative charge decreases until an asymptotic value of 10% of the maximum charge. 129
5.12 Distribution of the reconstructed position. R_{true} is the true position of events given by MC and R_{reco} is the calculated position. 130
5.13 Top: Event time distribution for 0.5 kV cm^{-1} drift field, and its fit to the Heaviside function. Bottom: Drift velocity as a function of drift field, for xenon gas at 10 bar. The red square points are the measured values, green circles correspond to the results of [123], blue triangles are from [122] while the dashed curve is the prediction for pure xenon at 10 bar from the Magboltz 9.0.2 simulation [121]. 133

5.14 Top: Temporal charge distribution of a typical X-ray event and Gaussian fit. Bottom: Variance of the Gaussian fits versus drift time t_d, and linear fit to the model obtaining S_L^2 as the intercept. 135
5.15 Top: Longitudinal sigma of the temporal charge distribution fits versus drift length for the 0.5 kV drift field configuration dataset. Bottom: Longitudinal diffusion coefficient D_L as a function of drift field for xenon gas at 10 bar. The red square points are the measured values, green circles correspond to the results of [123], blue triangles are from [122] while the dashed curve is the prediction for pure xenon at 10 bar from the Magboltz 9.0.2 simulation [121]. 137
5.16 Top: Average 3D charge distribution of a X-ray event from its barycenter. Bottom: S_T, σ_x and σ_y of charge distribution gaussian fit versus Drift Time. 138
5.17 Mean charge of X-ray events versus drift time. Exponential fit is made and decay constant extracted. 140
5.18 Mean charge of X-ray events versus time in a range of six months. 141
5.19 Distribution of response to K_α events of a PMT in four bin x, y and gaussian fits to calculate correction factors. 143
5.20 Calculated correction factors (white points) versus their x,y position. Delaunay interpolation is represented in color, increasing the number of points by 2 orders of magnitude. 144
5.21 Spectrum of an individual bin x, y to extract $S_0(x, y)$ for equation 5.12. 145
5.22 Top: ^{22}Na spectrum after all corrections. Bottom-left: Zoom of X-ray peak region and gaussian fit of the K_α peak. Bottom-right: Zoom of the escape and photoelectric peaks and gaussian fit to the Photoelectric. 146

5.23 Top: ^{137}Cs spectrum after all corrections. Bottom-left: Zoom of X-ray peak region and gaussian fit of the K_α peak. Bottom-right: Zoom of the escape and photoelectric peaks and gaussian fit to the Photoelectric. 147
5.24 Energy resolution achieved in NEXT-DEMO as a function of energy and fit to equation 5.13. 149

List of Tables

2.1 Neutrino mixing angles and experimental measurement of Δm^2_{ij} according to global oscillation analysis [28]. . . 10
2.2 Observed double beta decay isotopes and best measured half-life of the two neutrino mode [8]. 20

3.1 NEXT-100 pressure vessel basic parameters and dimensions (some of these quantities could change slightly during the construction phase due to refinements in the design) [60]. 44
3.2 Basic parameters of the electric field regions (drift and EL) of NEXT-100 [60]. 46
3.3 Hamamatsu R11410-10 photomultiplier basic parameters [60]. 48
3.4 Acceptance of the selection criteria for $\beta\beta0\nu$-decay events described in the text. The values for ^{208}Tl and ^{214}Bi correspond to one of the dominant sources of background in the detector. 53

4.1 Hamamatsu S10362-11-050P SiPM basic parameters [89]. 66
4.2 Thicknesses and densities of TPB depositions samples. . 90

5.1 Energy Resolution obtained with the Energy Weighted Sum method for ^{22}Na and ^{137}Cs sources, and independent extrapolation to the $Q_{\beta\beta}$ value of ^{136}Xe assuming a $1/\sqrt{E}$ dependence. 149

Bibliography

[1] F. Reines and C. L. Cowan, *Detection of the free neutrino*, Phys. Rev. **92** (Nov, 1953) 830–831. 1

[2] M. Fukugita and T. Yanagida, *Baryogenesis Without Grand Unification*, Phys. Lett. **B174** (1986) 45. 2, 20

[3] S. Davidson, E. Nardi, and Y. Nir, *Leptogenesis*, Phys. Rept. **466** (2008) 105–177, [arXiv:0802.2962]. 2, 20

[4] NEXT Collaboration, D. Lorca et al., *Characterisation of NEXT-DEMO using xenon K_α X-rays*, JINST **9** (2014) P10007, [arXiv:1407.3966]. 2, 4, 55, 113

[5] NEXT Collaboration, V. Álvarez et al., *Operation and first results of the NEXT-DEMO prototype using a silicon photomultiplier tracking array*, JINST **8** (2013) P09011, [arXiv:1306.0471]. 2, 55, 56, 57, 157

[6] NEXT Collaboration, V. Alvarez et al., *Design and characterization of the SiPM tracking system of NEXT-DEMO, a demonstrator prototype of the NEXT-100 experiment*, JINST **8** (2013) T05002, [arXiv:1206.6199]. 3

[7] NEXT Collaboration, V. Alvarez, J. Agramunt, M. Ball, M. Batalle, J. Bayarri, et al., *SiPMs coated with TPB : coating protocol and characterization for NEXT*, JINST **7** (2012) P02010, [arXiv:1201.2018]. 4, 87, 91

[8] Particle Data Group, K. Olive et al., *Review of Particle Physics*, Phys. Rev. **C38** (2014) 090001. 6, 12, 20, 165

[9] E. Majorana, *Theory of the Symmetry of Electrons and Positrons*, Nuovo Cim. **14** (1937) 171–184. 6, 16

[10] Wikipedia, *Standard model — wikipedia, the free encyclopedia*, 2014. http://en.wikipedia.org/w/index.php?title=Standard_Model&oldid=592640485. 7, 155

[11] B. T. Cleveland, T. Daily, J. Davis, Raymond, J. R. Distel, K. Lande, et al., *Measurement of the solar electron neutrino flux with the Homestake chlorine detector*, Astrophys. J. **496** (1998) 505–526. 8

[12] J. N. Bahcall, M. Pinsonneault, and S. Basu, *Solar models: Current epoch and time dependences, neutrinos, and helioseismological properties*, Astrophys. J. **555** (2001) 990–1012, [astro-ph/0010346]. 8

[13] SAGE Collaboration, J. Abdurashitov et al., *Measurement of the solar neutrino capture rate with gallium metal. III: Results for the 2002–2007 data-taking period*, Phys. Rev. **C80** (2009) 015807, [arXiv:0901.2200]. 8

[14] F. Kaether, W. Hampel, G. Heusser, J. Kiko, and T. Kirsten, *Reanalysis of the GALLEX solar neutrino flux and source experiments*, Phys. Lett. **B685** (2010) 47–54, [arXiv:1001.2731]. 8

[15] GNO COLLABORATION, M. Altmann et al., *Complete results for five years of GNO solar neutrino observations*, Phys. Lett. **B616** (2005) 174–190, [hep-ex/0504037]. 8

[16] *SNO experiment website*. http://www.sno.phy.queensu.ca. 8

[17] SNO Collaboration, Q. Ahmad et al., *Measurement of the rate of $\nu_e + d \rightarrow p + p + e^-$ interactions produced by ^8B solar neutrinos at the Sudbury Neutrino Observatory*, Phys. Rev. Lett. **87** (2001) 071301, [nucl-ex/0106015]. 8

[18] Super-Kamiokande Collaboration, Y. Fukuda et al., *Study of the atmospheric neutrino flux in the multi-GeV energy range*, Phys. Lett. **B436** (1998) 33–41, [hep-ex/9805006]. 8

[19] M. H. Ahn et al., *Measurement of neutrino oscillation by the k2k experiment*, Phys. Rev. D **74** (Oct, 2006) 072003. 8

[20] KamLAND Collaboration, K. Eguchi et al., *First results from KamLAND: Evidence for reactor anti-neutrino disappearance*, Phys. Rev. Lett. **90** (2003) 021802, [hep-ex/0212021]. 8

[21] Z. Maki, M. Nakagawa, and S. Sakata, *Remarks on the unified model of elementary particles*, Prog. Theor. Phys. **28** (1962) 870–880. 8

[22] B. Pontecorvo, *Neutrino Experiments and the Problem of Conservation of Leptonic Charge*, Sov. Phys. JETP **26** (1968) 984–988. 8

[23] Super-Kamiokande Collaboration, Y. Ashie et al., *Evidence for an oscillatory signature in atmospheric neutrino oscillation*, Phys. Rev. Lett. **93** (2004) 101801, [hep-ex/0404034]. 9

[24] KamLAND Collaboration, T. Araki et al., *Measurement of neutrino oscillation with KamLAND: Evidence of spectral distortion*, Phys. Rev. Lett. **94** (2005) 081801, [hep-ex/0406035]. 9

[25] T2K Collaboration, K. Abe et al., *Observation of Electron Neutrino Appearance in a Muon Neutrino Beam*, 2013, arXiv:1311.4750. 9

[26] Daya Bay Collaboration, F. An et al., *Independent measurement of the neutrino mixing angle θ_{13} via neutron capture on hydrogen at Daya Bay*, Phys.Rev. **D90** (2014), no. 7, 071101, [arXiv:1406.6468]. 9

[27] S.-B. Kim, *Observation of reactor electron antineutrino disappearance at RENO*, Nucl. Phys. Proc. Suppl. **235-236** (2013) 24–29. 9

[28] M. C. Gonzalez-Garcia, M. Maltoni, J. Salvado, and T. Schwetz, *Global fit to three neutrino mixing: critical look at present precision*, JHEP **1212** (2012) 123, [arXiv:1209.3023]. 10, 165

[29] R. Cahn, D. Dwyer, S. Freedman, W. Haxton, R. Kadel, et al., *White Paper: Measuring the Neutrino Mass Hierarchy*, 2013, arXiv:1307.5487. 10

[30] C. Weinheimer and K. Zuber, *Neutrino Masses*, Annalen Phys. **525** (2013), no. 8-9, 565–575, [arXiv:1307.3518]. 12

[31] V. Lobashev, V. Aseev, A. Belesev, A. Berlev, E. Geraskin, et al., *Direct search for mass of neutrino and anomaly in the tritium beta-spectrum*, Nucl. Phys. Proc. Suppl. **87** (2000) 275–277. 12

[32] C. Kraus, B. Bornschein, L. Bornschein, J. Bonn, B. Flatt, et al., *Final results from phase II of the Mainz neutrino mass search in tritium beta decay*, Eur. Phys. J. **C40** (2005) 447–468, [hep-ex/0412056]. 12

[33] KATRIN Collaboration, A. Osipowicz et al., *KATRIN: A Next generation tritium beta decay experiment with sub-eV sensitivity for the electron neutrino mass. Letter of intent*, 2001, hep-ex/0109033. 12

[34] J. Lesgourgues and S. Pastor, *Massive neutrinos and cosmology*, Phys. Rept. **429** (2006) 307–379, [astro-ph/0603494]. 13

[35] WMAP Collaboration, C. Bennett et al., *The Microwave Anisotropy Probe (MAP) mission*, Astrophys. J. **583** (2003) 1–23, [astro-ph/0301158]. 13

[36] 2DFGRS Collaboration, M. Colless et al., *The 2dF Galaxy Redshift Survey: Spectra and redshifts*, Mon. Not. Roy. Astron. Soc. **328** (2001) 1039, [astro-ph/0106498]. 13

[37] Planck Collaboration, P. Ade et al., *Planck 2013 results. I. Overview of products and scientific results*, 2013, arXiv:1303.5062. 13, 22

[38] M. Goldhaber, L. Grodzins, and A. W. Sunyar, *Helicity of Neutrinos*, Physical Review. **109** (1958), no. 3, 1015–1017, [arXiv:1307.3518]. 14

[39] C. Giunti and C. W. Kim, *Fundamentals of Neutrino Physics and Astrophysics*. OXFORD University Press, 2007. 14, 16, 17, 21

[40] P. Hernandez, *Neutrino physics*, 2010, arXiv:1010.4131. 14, 16

[41] P. Minkowski, $\mu \to e\gamma$ *at a rate of one out of 109 muon decays?*, Physics Letters B **67** (1977), no. 4, 421 – 428. 17

[42] T. Yanagida, *Horizontal Symmetry and Masses of Neutrinos*, Prog.Theor.Phys. **64** (1980) 1103. 17

[43] M. Gell-Mann, P. Ramond, and R. Slansky, *Complex Spinors and Unified Theories*, Conf.Proc. **C790927** (1979) 315–321, [arXiv:1306.4669]. 17

[44] R. Mohapatra and G. Senjanović, *Neutrino mass and spontaneous parity nonconservation*, Phys. Rev. Lett. **44** (Apr, 1980) 912–915. 17

[45] J. Martín-Albo, *The NEXT experiment for neutrinoless double beta decay searches*. PhD thesis, University of Valencia, 2015. http://inspirehep.net/record/1345217. 18, 38, 40, 43, 52, 128, 155, 156, 157

[46] M. Goeppert-Mayer, *Double beta-disintegration*, Phys. Rev. **48** (Sep, 1935) 512–516. 19

[47] W. H. Furry, *On transition probabilities in double beta-disintegration*, Phys. Rev. **56** (Dec, 1939) 1184–1193. 19

[48] J. Schechter and J. W. F. Valle, *Neutrinoless double-β decay in $su(2) \times u(1)$ theories*, Phys. Rev. D **25** (Jun, 1982) 2951–2954. 19, 24

[49] EXO-200 Collaboration, J. Albert et al., *Search for Majorana neutrinos with the first two years of EXO-200 data*, Nature **510** (2014) 229–234, [arXiv:1402.6956]. 22

[50] The KamLAND-Zen Collaboration, T. K.-Z. Collaboration, *Results from KamLAND-Zen*, 2014, arXiv:1409.0077. 22

[51] GERDA, B. Lehnert, *GERDA: Recent results and future plans*, Nucl. Instrum. Meth. **A742** (2014) 254–257. 23

[52] M. Agostini, M. Allardt, A. Bakalyarov, M. Balata, I. Barabanov, et al., *Results on $\beta\beta$ decay with emission of two neutrinos or*

Majorons in ^{76}Ge from GERDA Phase I, 2015, arXiv:1501.0234. 23

[53] GERDA Collaboration, M. Agostini et al., *Results on Neutrinoless Double-β Decay of ^{76}Ge from Phase I of the GERDA Experiment*, Phys. Rev. Lett. **111** (2013), no. 12, 122503, [arXiv:1307.4720]. 23

[54] KamLAND-Zen Collaboration, A. Gando et al., *Limit on Neutrinoless $\beta\beta$ Decay of Xe-136 from the First Phase of KamLAND-Zen and Comparison with the Positive Claim in Ge-76*, Phys. Rev. Lett. **110** (2013), no. 6, 062502, [arXiv:1211.3863]. 23, 24, 28

[55] EXO Collaboration, M. Auger et al., *Search for Neutrinoless Double-Beta Decay in ^{136}Xe with EXO-200*, Phys. Rev. Lett. **109** (2012) 032505, [arXiv:1205.5608]. 23

[56] J. Bergstrom, *Combining and comparing neutrinoless double beta decay experiments using different nuclei*, JHEP **1302** (2013) 093, [arXiv:1212.4484]. 24

[57] C. Iacobaeus, T. Francke, B. Lund-Jensen, J. Ostling, P. Pavlopoulos, et al., *A High position resolution X-ray detector: An 'Edge on' illuminated capillary plate combined with a gas amplification structure*, IEEE Trans. Nucl. Sci. **53** (2006) 554–561, [physics/0411082]. 28

[58] LUX Collaboration, D. Akerib et al., *The Large Underground Xenon (LUX) Experiment*, Nucl. Instrum. Meth. **A704** (2013) 111–126, [arXiv:1211.3788]. 28

[59] T. Ohashi, K. Ebisawa, Y. Fukazawa, K. Hiyoshi, M. Horii, et al., *The Gas Imaging Spectrometer on Board ASCA*, Publ. Astron. Soc. Jap. **48** (1996) 157–170. 28

[60] NEXT Collaboration, V. Alvarez et al., *NEXT-100 Technical Design Report (TDR): Executive Summary*, JINST **7** (2012) T06001, [arXiv:1202.0721]. 28, 42, 44, 46, 48, 49, 50, 52, 139, 165

[61] EXO-200 Collaboration, J. Albert et al., *Improved measurement of the $2\nu\beta\beta$ half-life of ^{136}Xe with the EXO-200 detector*, Phys. Rev. **C89** (2014), no. 1, 015502, [arXiv:1306.6106]. 28

[62] E. Aprile et al., *Noble Gas Detectors*. Wiley-VCH, 2006. 29, 30, 31

[63] T. H. V. T. Dias, J. M. F. dos Santos, P. J. B. M. Rachinhas, F. P. Santos, C. A. N. Conde, and A. D. Stauffer, *Full-energy absorption of x-ray energies near the xe l- and k-photoionization thresholds in xenon gas detectors: Simulation and experimental results*, Journal of Applied Physics **82** (1997), no. 6, 2742–2753. 29

[64] F. Borges, J. dos Santos, T. Dias, F. Santos, P. Rachinhas, and C. Conde, *Operation of gas proportional scintillation counters in a low charge multiplication regime*, Nucl. Instrum. Meth. **A422** (1999), no. 1–3, 321 – 325. 32, 33, 156

[65] C. Monteiro et al., *Secondary scintillation yield in pure xenon*, JINST **2** (2007) P05001. 32

[66] U. Fano, *Ionization yield of radiations. the fluctuations of the number of ions*, Phys. Rev. **72** (Jul, 1947) 26–29. 34

[67] G. Knoll, *Radiation Detection and Measurement*. John Wiley, 2010. 34

[68] D. Anderson, T. Hamilton, W.-M. Ku, and R. Novick, *A large area, gas scintillation proportional counter*, Nuclear Instruments and Methods **163** (1979), no. 1, 125 – 134. 34

[69] A. Policarpo, M. Alves, M. Salete, S. Leite, and M. dos Santos, *Detection of soft x-rays with a xenon proportional scintillation counter*, Nuclear Instruments and Methods **118** (1974), no. 1, 221 – 226. 34

[70] H. Sipilä, *Energy resolution of the proportional counter*, Nuclear Instruments and Methods **133** (1976), no. 2, 251 – 252. 34

[71] EXO Collaboration, E. Conti et al., *Correlated fluctuations between luminescence and ionization in liquid xenon*, Phys.Rev. **B68** (2003) 054201, [hep-ex/0303008]. 34

[72] A. Bolotnikov and B. Ramsey, *The spectroscopic properties of high-pressure xenon*, Nucl. Instrum. Meth. **A396** (1997) 360. 34, 35, 156

[73] A. Bolozdynya, V. Egorov, A. Koutchenkov, G. Safronov, G. Smirnov, S. Medved, and V. Morgunov, *A high pressure xenon self-triggered scintillation drift chamber with 3d sensitivity in the range of 20–140 kev deposited energy*, Nuclear Instruments and Methods in Physics Research Section A: Accelerators, Spectrometers, Detectors and Associated Equipment **385** (1997), no. 2, 225 – 238. 37

[74] J. Miyamoto and G. Knoll, *The statistics of avalanche electrons in micro-strip and micro-gap gas chambers*, Nuclear Instruments and Methods in Physics Research Section A: Accelerators, Spectrometers, Detectors and Associated Equipment **399** (1997), no. 1, 85 – 93. 37

[75] P. Rachinhas, T. Dias, A. Stauffer, F. Santos, and C. Conde, *Energy resolution of xenon proportional counters: Monte carlo simulation and experimental results*, Nuclear Science, IEEE Transactions on **43** (Aug, 1996) 2399–2405. 37

[76] NEXT Collaboration, F. Granena et al., *NEXT, a HPGXe TPC for neutrinoless double beta decay searches*, 2009, arXiv:0907.4054. 37

[77] D. Nygren, *High-pressure xenon gas electroluminescent TPC for 0-ν ββ-decay search*, Nucl. Instrum. Meth. **A603** (2009) 337–348. 39

[78] NEXT Collaboration, V. Alvarez, I. Bandac, A. Bettini, F. Borges, S. Carcel, et al., *Radiopurity control in the NEXT-100 double beta decay experiment: procedures and initial measurements*, JINST **8** (2013) T01002, [arXiv:1211.3961]. 42

[79] NEXT Collaboration, V. Alvarez et al., *Radiopurity assessment of the tracking readout for the NEXT double beta decay experiment*, 2014, arXiv:1411.1433. 44

[80] K. Lung, K. Arisaka, A. Bargetzi, P. Beltrame, A. Cahill, et al., *Characterization of the Hamamatsu R11410-10 3-Inch Photomultiplier Tube for Liquid Xenon Dark Matter Direct Detection Experiments*, Nucl. Instrum. Meth. **A696** (2012) 32–39, [arXiv:1202.2628]. 48

[81] *Hamamatsu webpage*. http://www.hamamatsu.com/eu/en/index.html. 49, 59, 65, 82

[82] *SensL MicroFC- 10035-SMT-GP*. http://bit.ly/1tn1yjh. 49

[83] KATRIN Collaboration, *Development of micro-pattern gas detector technologies*. http://rd51-public.web.cern.ch/rd51-public/l. 50

[84] *Laboratorio Subterraneo de Canfranc*. http://www.lsc-canfranc.es/. 50

[85] J. Barea, J. Kotila, and F. Iachello, *Nuclear matrix elements for double-β decay*, Phys. Rev. **C87** (2013) 014315, [arXiv:1301.4203]. 54, 157

[86] N. L. Vaquero, T. R. Rodriguez, and J. L. Egido, *Shape and pairing fluctuations effects on neutrinoless double beta decay nuclear matrix elements*, Phys. Rev. Lett. **111** (2013) 142501, [arXiv:1401.0650]. 54, 157

[87] J. Menendez, A. Poves, E. Caurier, and F. Nowacki, *Disassembling the nuclear matrix elements of the neutrinoless beta beta decay*, Nucl. Phys. **A818** (2009) 139–151, [arXiv:0801.3760]. 54, 157

[88] NEXT Collaboration, V. Alvarez et al., *Initial results of NEXT-DEMO, a large-scale prototype of the NEXT-100 experiment*, JINST **8** (2013) P04002, [arXiv:1211.4838]. 55

[89] *Hamamatsu MPPC datasheet*. http://bit.ly/1zplQ1D. 59, 65, 66, 165

[90] W. Leo, *Techniques for Nuclear and particle Physics Experiments*. Springer-Verlag, second edition ed., 1994. 60, 62, 64, 76, 101

[91] *AD8055 Voltage Feedback Amplifier*. http://bit.ly/1ytVZTl. 68

[92] *LeCroy HRO 64Zi*. http://bit.ly/1lTQBRY. 68

[93] *Keithley 6517B electrometer*. http://bit.ly/1jWLdn1. 74

[94] R. P. et al., *Dark Current in Silicon Photomultiplier Pixels: Data and Model*, IEEE Transactions on Electron Devices **59** (2012), no. 9, 2410 – 2416. 77

[95] A. Spinelli and A. L. Lacaita, *Physics and Numerical Simulation of Single Photon Avalanche Diodes*, IEEE Transactions on Electron Devices **44** (1997), no. 11, 1931 – 1933. 78

[96] E. Garutti, *Silicon Photomultiers for high energy physics detectors*, JINST **6** (2011) C10003, [arXiv:1108.3166]. 79

[97] P. Eckert, H.-C. Schultz-Coulon, W. Shen, R. Stamen, and A. Tadday, *Characterisation Studies of Silicon Photomultipliers*, Nucl. Instrum. Meth. **A620** (2010) 217–226, [arXiv:1003.6071]. 79

[98] L. Shi and S. Nihtianov, *Comparative study of silicon-based ultraviolet photodetectors*, Sensors Journal, IEEE **12** (July, 2012) 2453–2459. 80

[99] S. M. Sze and K. K. Ng, *Physics of Semiconductor Devices*. Wiley-Interscience, 3 ed., 2006. 82, 159

[100] N. Yahlali, L. Fernandes, and D. Lorca, *Characterization of UV-enhanced sipms for imaging in a high pressure xenon electroluminescent TPC*, 3rd International Conference on Advancements in Nuclear Instrumentation Measurement Methods and their Applications (June, 2013). 81, 84, 85, 95, 96, 159, 160

[101] *Aldrich Chemical Company Inc.*. http://www.sigmaaldrich.com/catalog/product/aldrich/185213?lang=es&region=ES. 87

[102] C. Lally, G. Davies, W. Jones, and N. Smith, *UV quantum efficiencies of organic fluors*, Nucl. Instrum. Methods (1995). 87, 92, 93, 94

[103] V. Gehman, S. Seibert, K. Rielage, A. Hime, Y. Sun, et al., *Fluorescence Efficiency and Visible Re-emission Spectrum of Tetraphenyl Butadiene Films at Extreme Ultraviolet Wavelengths*, Nucl. Instrum. Meth. **A654** (2011) 116–121, [arXiv:1104.3259]. 87

[104] *INFICON, Industrial Vacuum Coating.*. http://bit.ly/1odXC5u. 89

[105] *KLA Tencor, Surface Profilometry and Surface Metrology*. http://www.kla-tencor.com/surface-profilometry-and-metrology.html. 89

[106] D. Lorca, *Desarrollo y caracterización de fotomultiplicadores de silicio para next (in spanish)*, Master's thesis, University of Valencia, 2010. http://bit.ly/1o5NvB7. 92, 93, 94, 159, 160

[107] V. Herrero, J. Toledo, J. Català, R. Esteve, A. Gil, D. Lorca, J. Monzó, F. Sanchis, and A. Verdugo, *Readout electronics for the sipm tracking plane in the next-1 prototype*, NIM A **695** (2012) 229 – 232. 98

[108] T. Instruments, *OPA659, High Speed Amplifier*. http://bit.ly/1v2hoWX. 98

[109] J. Toledo, H. Muller, R. Esteve, J. Monzo, A. Tarazona, et al., *The Front-End Concentrator card for the RD51 Scalable Readout System*, JINST **6** (2011) C11028. 99

[110] RD51 Collaboration, M. Chefdeville, *RD51, a world-wide collaboration for the development of micro pattern gaseous detectors*, J. Phys. Conf. Ser. **309** (2011) 012017. 99

[111] P. Marrocchesi, M. Bagliesi, K. Batkov, G. Bigongiari, M. Kim, T. Lomtadze, P. Maestro, F. Morsani, and R. Zei, *Active control of the gain of a silicon photomultiplier*, Nucl. Instrum. Meth. **A602** (2009), no. 2, 391 – 395. 101

[112] M. Integrated, *Maxim Integrated Products Inc.*. http://www.maximintegrated.com/en.html. 101

[113] A. Gil, J. Rodriguez, V. Alvarez, J. Diaz, J. Gomez-Cadenas, and D. Lorca, *Programmable power supply system for SiPM bias*, IEEE Nucl.Sci.Symp.Conf.Rec. **2011** (2011) 787–790. 105

[114] iseg hv, *iseg High Voltage.*. http://www.iseg-hv.com. 105

[115] *LeCroy PP008 Passive Probe*. http://teledynelecroy.com/probes/probemodel.aspx?modelid=1256&categoryid=3&mseries=428. 114

[116] M. Berger, J. Coursey, M. Zucker, , and J. Chang, *(2005) ESTAR, PSTAR, and ASTAR: Computer Programs for Calculating Stopping-Power and Range Tables for Electrons, Protons, and Helium Ions (version 1.2.3)*. Originally published as: Berger, M.J., NISTIR 4999, National Institute of Standards and Technology, Gaithersburg, MD (1993)., February, 2013. http://physics.nist.gov/Star. 116, 124

[117] J. Janesick, *Scientific Charge Coupled Devices*. SPIE Press, 2001. 118

[118] J. Hubbeli and S. Seltzer, *Tables of X-Ray Mass Attenuation Coefficients and Mass Energy-Absorption Coefficients from 1 keV to 20 MeV for Elements Z = 1 to 92 and 48 Additional Substances of Dosimetric Interest*. . http://www.nist.gov/pml/data/xraycoef/. 124

[119] Geant4, S. Agostinelli et al., *Geant4: A Simulation toolkit*, Nucl. Instrum. Meth. A **506** (2003) 250–303. 128

[120] J. Allison, K. Amako, J. Apostolakis, H. Araujo, P. Dubois, et al., *Geant4 developments and applications*, IEEE Trans.Nucl.Sci. **53** (2006) 270. 128

[121] *Magboltz - transport of electrons in gas mixtures*. http://consult.cern.ch/writeup/magboltz/. 131, 133, 137, 162, 163

[122] NEXT Collaboration, V. Alvarez et al., *Near-Intrinsic Energy Resolution for 30 to 662 keV Gamma Rays in a High Pressure Xenon Electroluminescent TPC*, Nucl. Instrum. Meth. **A708** (2013) 101–114, [arXiv:1211.4474]. 132, 133, 136, 137, 162, 163

[123] NEXT Collaboration, V. Alvarez et al., *Ionization and scintillation response of high-pressure xenon gas to alpha particles*, JINST **8** (2013) P05025, [arXiv:1211.4508]. 132, 133, 134, 136, 137, 162, 163

[124] A. Dobi et al., *A xenon gas purity monitor for EXO*, Nucl. Instrum. Meth. **A659** (2011), no. 1, 215 – 228. 139

[125] Wikipedia, *Delaunay triangulation — wikipedia, the free encyclopedia*, 2015. http://en.wikipedia.org/wiki/Delaunay_triangulation. 142